FLORIDA INTERNATIONAL UNIVERSITY

Miami, Florida

EFFECT OF WIND INDUCED LOADS ON ROOF OVERHANGS AND SOFFITS FOR LOW RISE BUILDINGS

A dissertation submitted in partial fulfillment of

the requirements for the degree of

DOCTOR OF PHILOSOPHY

in

CIVIL ENGINEERING

by

Karim Aly Mostafa

2022

To: Dean John L. Volakis
College of Engineering and Computing

This dissertation, written by Karim Aly Mostafa, and entitled Effect of Wind Induced Loads on Roof Overhangs and Soffits for Low Rise Buildings, having been approved in respect to style and intellectual content, is referred to you for judgment.

We have read this dissertation and recommend that it be approved.

Arindam Chowdhury

Amal Elawady

Seung Jae Lee

Arif Mohaimin Sadri

Ted Stathopoulos, Co-Major Professor

Ioannis Zisis, Co-Major Professor

Date of Defense: October 28, 2022

The dissertation of Karim Aly Mostafa is approved.

Dean John L. Volakis
College of Engineering and Computing

Andrés G. Gil
Vice President for Research and Economic Development
and Dean of the University Graduate School

Florida International University, 2022

DEDICATION

I dedicate this dissertation manuscript to my entire family and most importantly, to my parents, and my wife. Without their support, patience, constant motivation, understanding and most of all, unconditional love, the completion of this work would not have been possible.

ACKNOWLEDGMENTS

I would like to express my deepest gratitude to my major professor Dr. Ioannis Zisis for his unwavering support, guidance, strong encouragement and most importantly, endless support. I wish to thank him for accepting me into a very welcoming and encouraging atmosphere at the Wall of Wind (WOW), in addition to participating in research works outside my dissertation scope in order to advance my knowledge and broaden my skills. Special thanks go to my co-major professor Dr. Ted Stathopoulos for his constant support, advice, and guidance throughout the entirety of the work on my dissertation topic. I truly appreciate his humbleness, and quick responses whenever situations arise. Working with such a highly reputable person in the wind and structural engineering community was extremely inspirational. This manuscript would not have been possible without his expertise. I would also like to thank Dr. Arindam Chowdhury for his invaluable support and encouragement when I used to work under his supervision on one of the projects. Last but not least, I would like to thank my committee members Dr. Amal Elawady, Dr. Seung Jae Lee, and Dr. Arif Mohaimin Sadri for their cooperation and support in this dissertation work.

I gratefully acknowledge the financial support from Florida Building Commission (Award No. B83FC1) to conduct the large-scale testing at the Wall of Wind (WOW). I acknowledge the scholarship support provided by the Dissertation Year Fellowship (FIU, University Graduate School).The help from the WOW team including Dr. Steven Diaz, Dr. Dejiang Chen, Walter Conklin, Manuel Matus, and James Erwin. Finally, I would like to thank my parents, my wife, my brothers for their continuous support and love during my PhD journey.

ABSTRACT OF THE DISSERTATION

EFFECT OF WIND INDUCED LOADS ON ROOF OVERHANGS AND SOFFITS FOR LOW RISE BUILDINGS

by

Karim Mostafa

Florida International University, 2022

Miami, Florida

Professor Ioannis Zisis, Co-Major Professor

Professor Ted Stathopoulos, Co-Major Professor

Roof overhangs are prone to wind damage as they are subjected to wind load at both the upper and bottom surfaces. Wind standards, like ASCE 7-22, assume that the pressure at the bottom covering of the roof overhang is the same as the external pressure coefficient on the adjacent wall surface. A large-scale experimental campaign was carried out at the Wall of Wind (WOW) Research Experimental Facility to investigate the validity and possible limitations of such assumptions. The experimental setup considered eight 1:10 scaled models of a low-rise hip roof building of various geometrical parameters such as roof slope, roof overhang width, along with plethora of wind directions.

The study investigated the pressure and correlation coefficients between soffits and underneath walls to quantify the effect of overhang width. The experimental results confirmed that, for all configurations, soffit positive pressure coefficients may be assumed to be equal to the adjacent wall external pressure, as stated by ASCE7-22, while this might not be applicable for negative pressure coefficients. In addition, peak pressures on both the

upper and lower surfaces were measured to calculate the simultaneous net pressure coefficients along the overhangs. Area-averaged pressure analysis was carried out to investigate the pressure gradients on single or groups of taps on the overhangs, soffits, and walls. These area averaged GC_p were compared to previous and current versions of wind standards to evaluate their adequacy. The findings revealed that the provisions' design guidelines are less conservative for some roofing zones and wall zones, which justified the need for a codification study that will provide recommended design guidelines for overhangs and adjacent walls. The study provided new codified design guidelines, which are formed based on statistical determination rather than the enveloped procedures as commonly used. In addition, an empirical equation has been developed that correlated the relation between wall pressure coefficient and soffit pressure coefficient for different overhangs widths and different wind direction. Finally, different machine learning models were developed using the experimental data to predict the pressure coefficients among the surfaces of low-rise buildings.

Keywords*:* Roof overhangs, Roof soffits, Wind loads, Pressure coefficient, Wind tunnel, Wind standards and codes of practice, Codification study, Machine learning.

TABLE OF CONTENTS

LIST OF TABLES

TABLE PAGE

LIST OF FIGURES

FIGURE PAGE

CHAPTER I. INTRODUCTION

1.1. Background and project Motivation

An overhang is an unenclosed continuation of the roof surface. Particularly on low-rise residential applications, overhangs may be open or covered by a soffit and may be cantilevered or supported (**Fig.1. 1**). Most of the foundational belief about overhangs seems to suggest that overhangs extend no more than 60 cm, whereas, in Florida, overhangs are often much longer and are necessary for energy efficiency and livability in this semi-tropical climate. Overhangs in Florida can be cantilevered 1.8 m or more, or supported, as on a terrace or porch, for 3 m to 3.6 m or more.

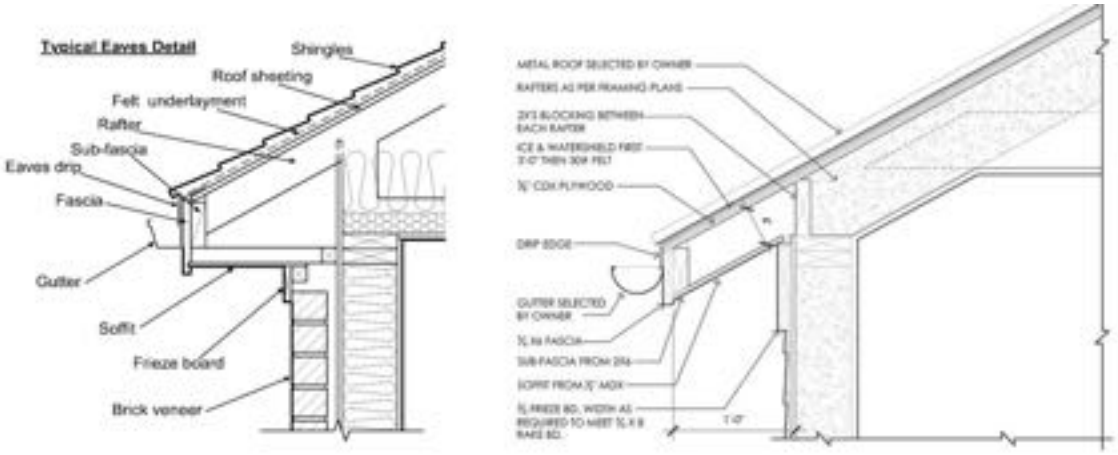

(a) (b)

Fig.1. 1: Typical details for (a) closed overhang (b) open overhang

Low-rise buildings are greatly affected by extreme wind events. The risk of wind-induced failure is particularly increased on roofs and roof overhangs. The latter are commonly used in residential and industrial buildings for weather protection against wind, snow, rain, and sun. Roof overhangs are prone to damage because they are subjected to wind from both the upper and bottom surfaces (soffit). They are vulnerable to uplift forces

that in some cases could trigger local or more severe failure on the roof (**Fig.1. 2**). Researchers at CSTB [Centre Scientifique et Technique du Bâtiment (Center for Building Science and Technology)] suggested to limit the length of overhangs to 50 cm especially for small slope roofs, (Taher 2007). Nevertheless, in warmer and sunny climates, it is common to use extended overhangs that go beyond the 60 cm and even reach 1.8 m. Extended overhangs resemble a roof extension like a canopy or a patio cover that is attached to the main structure. Recent studies showed that canopies may experience lower wind loads compared to those specified for roof overhangs on ASCE 7 (Candelario et al. 2014; Naeiji et al. 2022; Zisis et al. 2017; Zisis and Stathopoulos 2010)

Fig.1. 2: Aerial Footage of Great Guana Cay (Baker's Bay), Abaco after Dorian (retrieved on 2/26/2021 https://www.youtube.com/watch?v=92PutXku0xU&feature=youtu.be)

ASCE 7-16 (2017) provides methods for analysis of the loads on overhangs, both for main wind force resisting systems (MWFRS) and component and cladding (C&C) loads, but the commentary does not provide any information as to the maximum width of overhang for which this analysis is valid. In section 30.9, it states that the pressure on the bottom covering of the roof overhang is the external pressure coefficient on the adjacent wall surface as implemented by (Vickery 2008) as shown in (**Fig.1. 3**). This assumption was adopted more recently in the ASCE 7-16 (2017). In earlier versions of ASCE 7, for instance in ASCE 7 (2010), the overhang pressures considered the net pressure applied on these elements from simultaneous contributions from both the top and bottom surfaces of the overhang. In addition, this is only valid for positive pressure coefficient, with no information about the wall and soffit correlation for negative pressure coefficient. Moreover, the commentary in ASCE 7-16 and ASCE 7-22 does not provide any details about the maximum width for which this assumption could be valid, this may be an adequate assumption for a 60 cm overhang, but the pressure on the bottom surface of a 1.2 m or 1.8 m or 3.6 m overhang may not be a simple one-to-one wall-to-overhang pressure equivalent. The research that was done for canopies (ASCE 7-16 section 30.11), suggests that this may not be the case (Candelario et al. 2014, Zisis et al. 2017).

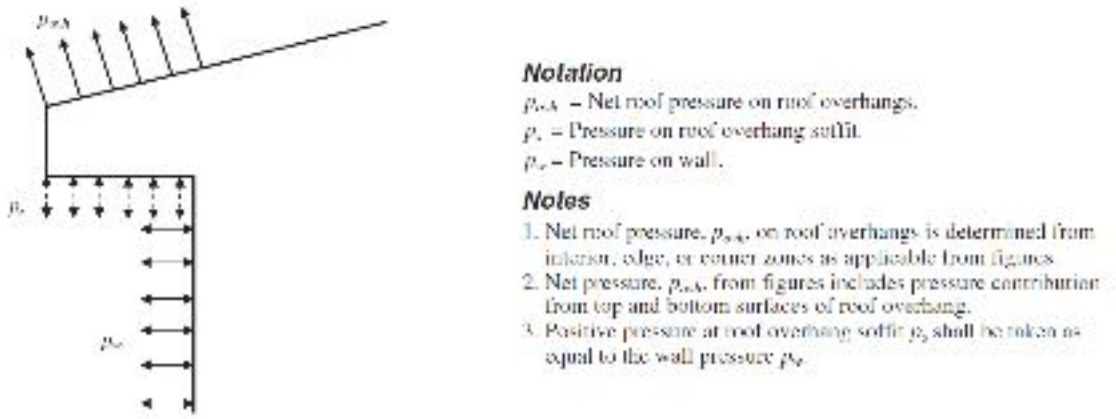

Fig.1. 3: ASCE 7-16 - Fig. 30.9-1 Components and Cladding (All Building Heights)

In this project, wind tunnel testing using large-scale models with different overhang width were carried out to investigate how the pressures on the wall relate to the overhang and for what distance. In addition, it was important to investigate at what point the wall pressure cease to affect the overhang. The following sections discuss the previous studies that investigated the wind induced loads on roof overhangs and their limitations.

1.2. Previous Studies and Literature Review

Different studies were selected and reviewed in this section that include both physical testing and numerical simulations. The findings provided information on the wind-induced loading on the upper and lower surface for the roof overhangs while considering different aspects and parameters (see **Table 1.1**). In an effort to better understand their contributions and limitations, the discussion is organized based on:

- The effect of roof geometry.
- The effect of overhang length.
- The interference effect of surrounding buildings on a single building with overhangs.

- Severe wind events and performance of roof overhangs.
- The effect of boundary wall locations on building with overhangs.
- Numerical simulation efforts to estimate wind loads on overhangs.

1.2.1. Wind induced forces on eaves of low buildings with higher slope roof

The effect of wind on eaves with higher slope roof (i.e. higher than 10°) was studied by (Stathopoulos and Luchian 1994). The experiments of this study were conducted in the boundary layer wind tunnel of the Building Aerodynamics Laboratory at Concordia University. Two models were tested with a geometric scale of 1:400. Open terrain exposure was considered for all tests with a velocity profile represented by a power law with exponent of 0.15. The maximum wind speed at the gradient height in the tunnel was 13m/s. Two gable roof models with roof slopes of 4:12 and 12:12 were used for the measurements of the wind induced pressures on eaves. Each building was 40 m wide and 60 m long (at full scale), one with eave height of 5m and the other of 10 m. The two models were equipped with pressure taps on lower and upper surfaces of the eave, as well as corresponding walls for comparison purposes.

This study found that the model with roof slope of 4:12 resulted into higher loads especially on the upper overhang surface and near the gable end. Positive pressures were found to be higher on the upper surface of the roof with slope of 12:12, as expected from the wind flow considerations. Furthermore, it was found that the lower surface of the 4:12 slope was subjected to higher pressures and suctions. The eave height also had an effect on the pressure coefficients while the pressure measured on the wall surface and the eave

lower surface compared well. However, some positive peaks under the eaves were significantly higher compared to the wall pressures.

1.2.2. The assessment of wind loads on roof overhang with different widths

This study concluded that larger overhangs would influence the pressure coefficient "Cp" values on both roofs and walls compared to roofs without overhangs or roofs with smaller overhangs. A study by (Wiik and Hansen 1997) investigated the effect of two overhangs of 0.3 m and 3.4 m on the wind load on the house walls. The study utilized both an experimental approach and numerical simulations. The experiments were conducted in the industrial aerodynamic wind tunnel of the University of Hertfordshire, UK while a commercial CFD code was used in the numerical simulations with a k-ε turbulence model. **Fig.1. 4** shows a sketch for the house models with and without roof overhang at the gable wall.

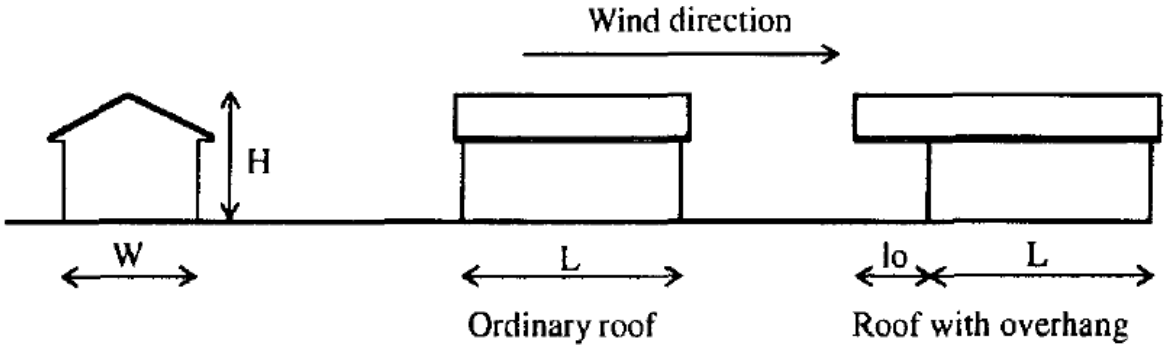

Fig.1. 4: Sketch shows the side view and elevation for the building model (Wiik and Hansen 1997)

For the gable wall, in the case of the ordinary roof, the stagnation point occurred at 2/3 of the model height and then the pressure reduced towards the roof. For the large roof overhang model, the stagnation point occurred at the top of the wall indicating that the upper part of the wall was subjected to higher wind forces compared to the ordinary roof.

Moreover, the ordinary roof appeared to have higher Cp values near the edge compared to the large overhang roof. This was attributed to the high velocity in the z-direction at the edge of the ordinary roof, due to the nearby walls that lead part of the flow over the roof. Finally, it was concluded that large overhang will experience higher total uplift force due to the combination of pressure on the lower side and suction on the upper side.

1.2.3. Field monitoring under extreme events and wind tunnel study of wind effects on roof overhangs

The effect of roughness surface and turbulence intensity have a recognized effect on the induced pressure coefficients on both roofs and roof overhangs. A field study was conducted during Typhoons Mujigae and Sarika, which was also supported by detailed wind tunnel tests on a 1:50 scaled model of the low-rise gable roof building that was used during the field measurements (Wang et al. 2020). Three terrain exposures were generated in the wind tunnel corresponding to three surface roughness lengths, zo=0.3m, zo=0.087m, and zo=0.03 m. The model was instrumented with pressure taps on the upper and lower surface of the roof overhang in both model and full-scale measurements. Pressure coefficients on the upper and lower surfaces, and net pressure coefficients of the roof overhang were discussed in detail in this study.

It was found that as the turbulence intensity increases, the maximum magnitude of the RMS and minimum pressure coefficients increases. The correlation coefficients of wind pressure were significantly influenced by the turbulence intensity on the front edge of the overhang and the edge near the building wall, while the turbulence intensity had a little effect on the correlation coefficients on the corner of the roof overhang.

The variation of the different pressure coefficients (mean, RMS, max and min) shows a good agreement between the wind tunnel measurements and the field measurements. However, the reduced scale experimental results underestimated the peak coefficients compared to field measurements, which was attributed to the Reynolds number mismatch between the wind tunnel and the full-scale tests. Finally, the comparison of the experimental results - model scale and full-scale – to the ASCE 7-16, showed that ASCE 7 was in general more conservative.

1.2.4. Numerical simulations to study the wind loads on overhangs

(Majid et al. 2016) investigated the effect of roof overhang length on the pressure coefficient underneath the overhang considering the presence of an attached secondary space directly below the overhang. The CFD analysis used the Reynolds-averaged Navier-Stokes equations (RANS) with an RNG k-ε turbulence model. Four overhang widths were used, including 0.5 m, 0.75 m, 1.0 m, and 1.25 m overhangs while the roof for the four models had the same pitch of 27°. The study showed that the diameter of the recirculation eddy increased with increasing the overhang length. The highest positive pressure coefficient was formed at the wall underneath the 0.5 m overhang, due to the smaller eddies that were formed and lead the flow to impinge the wall directly.

1.2.5. Effect of overhangs on wind pressures on low-rise hip roof buildings

(Ahmad and Kumar 2002) investigated the effect of different overhang length and eave height aspect ratios on the wind pressures on a hip roof with pitch of 30°. The focus of this study was on the main roof loads rather than the overhang areas. Experiments were carried out in a wind tunnel at the University of Roorkee, Roorkee (India). Six hip roof building models of a building 14 m x 7 m and 2.9 m eave height were constructed at 1:50

scale. Three of the models had overhang widths of 0.5 m, 0.75 m and 1.1 m while the height remained constant, and the aspect ratio was 0.4. The remaining three models have variable height and aspect ratios of 0.4, 0.5 and 0.6 while the overhang length was fixed at 1.1 m.

Both the overhang and aspect ratio variations were found to influence the magnitude and distribution of pressures on the hip roof. The maximum peak pressures among the three overhangs have been found to occur at the edge corner of the 0.75m overhang. The peak pressure on the corner edge for the 1.1 m overhang was also high but a bit smaller than the peak pressure of the 0.75 m overhang.

One other study (Vickery 2008) is considered as one of the most extremely important studies in studying the wind induced loads on soffits and adjacent walls and their correlations. This study investigated low-rise buildings with a hip roof of slope 4:12 and overhang width of 0.51 m. The models are composed of one-, two-, and three-story buildings that have been tested in a wind tunnel. This study suggested that the soffit pressure coefficient can be taken exactly the same as the wall pressure coefficient for both positive and negative pressures. The findings from this study have been adapted later in ASCE 7-16 and ASCE 7-22, suggesting that the positive pressure coefficient of the soffit equal to the positive pressure coefficient of the walls, without mentioning any details about the negative pressure coefficient. In addition, the commentary does not provide any information about the maximum width where this assumption can be valid. Therefore, it is extremely important to investigate the effect of different overhangs width on both positive and negative pressures and the soffit correlation with the walls.

1.2.6. Experimental study of wind loads on gable roofs of low-rise buildings with overhangs

The wind pressure distribution on gable roofs with overhangs was investigated by (Huang et al. 2018) through an extensive amount of wind tunnel tests. The study considered 99 test cases with various roof pitches, height-depth ratios, and width-depth ratios. The experiments were conducted at Tongji University and the models included cases with 11 different roof pitches, 3 different height-depth ratios, and 3 different width-depth ratios. Pressure taps were placed on the upper and lower surfaces of the roof overhangs.

For roof pitch of 0° to 9.5°, the negative block (i.e. area averaged) pressure coefficient increased while for roof pitch larger than 9.5°, the block pressure coefficient linearly decreased. The negative block pressure coefficients on overhangs decreased from – 2.0 at the roof pitch of 0°– 10° to a positive block pressure coefficient of 0.1 at the roof pitch of 60°.

1.2.7. Wind load on overhangs in a low gable building in presence of free-standing wall

Some studies investigated the presence of a free-standing wall or the interference of other buildings on loads on overhangs. (John et al. 2008) experimentally studied the effect of a free-standing wall (boundary wall) on the pressure variation on the overhang for a gable roof building with a 25° slope **Fig.1. 5**. The wind tunnel model was at 1:25 scale and the overhang length was 1.5 m at full scale. The study found that the edge of the overhang experiences severe changes in pressure values with change in the distance of the boundary wall from the parent building. It was found that the maximum value of the net positive pressure occurred when the free-standing wall was located at a distance 3h from the building, where h is the building height. For a stand-alone case without the wall, the

overhang experienced the maximum negative net pressure. On a follow up study, (John et al. 2011) examined the interference effect of boundary wall on pressure variation on the roof overhang, the roof, and the wall for a gable roof building. Overall, it was concluded that the boundary walls may significantly reduce the wind pressures on roof overhangs while this interference effect reaches its maximum up to a certain distance after which there is practically no effect.

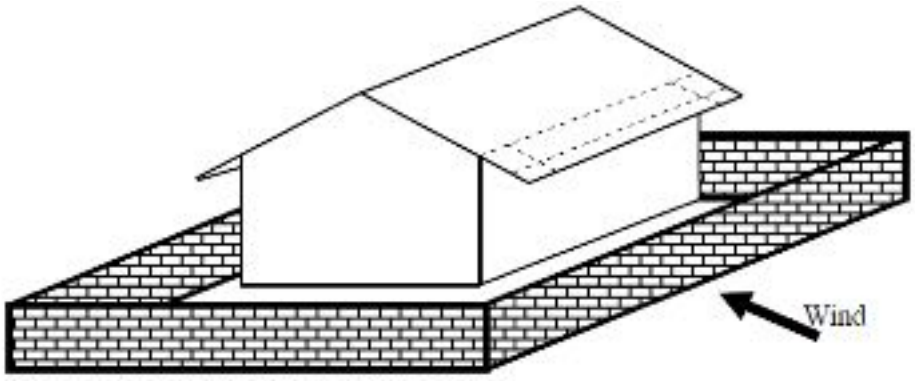

Fig.1. 5: A sketch for a gable roof building with overhang surrounded by boundary wall (John et al. 2008)

Table 1. 1: Different configuration and findings for overhangs in previous studies

Different Aspects	Methodology	Findings
Roof Geometry (Stathopoulos and Luchian 1994)	- Two gable roof models with slopes 4:12 and 12:12 were studied	- Positive pressure on the upper surface found to be higher on the 12:12 slope. - Higher pressure and suction at 4:12 slope
Roof Geometry (Huang et al. 2018)	- 99 models all with overhangs have 11 different roof pitches, 3 different height-depth ratios, and 3 different width-depth ratios.	- Negative block pressure coefficients on overhang decreased from – 2.0 at the roof pitch of 0°– 10° to a positive block pressure coefficient of 0.1 at the roof pitch of 60°.
Length of Overhang (Wiik and Hansen 1997)	- Cp values on two models with two overhangs width 0.3 m, 3.4 m were studied experimentally.	- Different location for stagnation point between the two models. - Higher uplift force in case of the large overhang width. - Higher Cp near the upper edge for shorter overhang width.
Length of Overhang (Majid et al. 2016)	- A numerical investigation studied the effect of four overhangs (0.5 m, 0.75 m, 1.0 m, and 1.25 m) on Cp underneath the overhang.	- Diameter of the recirculation eddy increased with increasing the overhang length. - Highest wall pressure occurred underneath the shortest overhang.
Length of Overhang (Ahmad and Kumar 2002)	- Hip roof models with overhang length (0.5 m, 0.75 m, and 1.0 m) were studied for Cp coefficients.	- Overhangs were found to influence magnitude and distribution of pressure on roof. - Max peak pressure were found at the edge corner of 0.75 m overhang.
Interference of walls (John et al. 2008)	- Cp coefficients on overhang in a gable roof building with the presence of a boundary wall located around the building.	- The maximum value of the net positive pressure was at a case when the free-standing wall located a distance 3h from the building, where h is the building height. - The overhang experienced the maximum negative net pressure when there was no wall.
Effect of Roughness surface (Wang et al. 2020)	- A model was tested for three roughness surfaces, zo= (0.3 m, 0.087 m and 0.03 m)	- Increasing the turbulence intensity, causes increase in the magnitude of minimum pressure on overhangs.

1.3. Limitations of Previous Studies

The previous studies on roof overhangs included different configurations and valuable findings related to pressure coefficients on overhangs. However, some of these studies had some limitations that need to be considered and help us identify research gaps and priorities. For instance, Wiik and Hansen (1997) examined two models with two rather extreme widths for roof overhangs (i.e. 0.3 m and 3.4 m) and did not consider intermediate widths. Ahmad and Kumar (2002) examined three widths of roof overhangs (i.e. 0.5 m, 0.75 m and 1.0 m) and it was found that the 0.75 m overhang had the maximum negative peak Cp while the 1.0 m overhang had the lowest value. Widths over 1.0 m might provide additional details on the behavior of longer overhangs. Majid et al. (2016) examined four widths of roof overhangs numerically which is not expected to provide valuable input from a codification point of view.

In summary, previous studies did not adequately examine the relation between the Cp magnitude at adjacent walls and underneath the roof overhang. Moreover, there was not enough knowledge at what length of the overhang does the Cp differ from the adjacent wall Cp (i.e. basic assumption implemented by ASCE7-16). Finally, smaller-scale models did not allow for high pressure tap resolution and did not consider any Reynolds number effects.

Therefore, it was decided to perform physical testing at a large scale and consider the following configurations:

- A Hip roof of slope 4:12 and 6:12 with three different overhang widths (0.6 m, 1.2 m and 1.8 m) with horizontal soffit to study the variation of Cp on the upper and

lower surface of the overhang, and on the adjacent wall. This shall be used for codification purposes with ASCE 7-16.

- A Hip roof of slope 4:12 with two different overhang width (0.6 m and 1.2 m) but with no horizontal soffit to study the variation of Cp on the upper and lower surface of the overhang and compare it with similar cases but with horizontal soffits in terms of surface uplift pressure.

1.4. Research Objectives and Tasks

A physical testing at a large-scale was performed to clarify for the first time how the pressures on the wall relate to the overhang and for what distance, and at what point the wall pressure cease to affect the overhang. The previous studies that examined roof overhangs were limited because they considered only small-scale wind tunnels. To overcome this limitation, the proposed study herein will be conducted at the Wall of Wind (WOW), a national large scale experimental facility, at Florida International University (FIU). The large-scale wind tunnels like the WOW, consider the effect of Reynolds number that was violated before in small wind tunnels. In addition, the large-scale models that will be carried out at the WOW allow for high pressure tap resolution. This study shall contribute to a new empirical model that govern the accurate relation between the wall surface pressure and the soffit pressure, and this model will be ready to implement and ideally could be merged into code provisions for roof overhangs. Therefore, the research objectives can be summarized as follows.

- **OBJECTIVE #1:** Investigate overhang undersurface versus wall pressure correlation and development of a new empirical model

- Previous studies did not adequately examine the relation between the pressure coefficient '*Cp*' magnitude at adjacent walls and underneath the roof overhang.
- By testing different cases and parameters for roof overhangs, an empirical model will be developed to govern the correlation between the pressure on the wall surface and the pressure on the soffit.

- **OBJECTIVE #2:** Investigate the effect of overhang width on wind-induced load
  - There was not enough knowledge about the width of the overhang at which the soffit *Cp* differ from the adjacent wall *Cp* (i.e., basic assumption implemented by ASCE 7-16).
- **OBJECTIVE #3:** Utilize larger models to allow for a more detailed pressure monitoring and explore permissible reduction in pressure taps instrumentation
  - Smaller-scale models did not allow for high pressure tap resolution and did not consider any Reynolds number effects.
  - Physical testing at a large scale will be performed to clarify how the pressures on the wall relate to the overhang and for what distance.
- **OBJECTIVE #4:** Codification study with ASCE 7-10, ASCE7-16 and ASCE7-22
  - The latest three versions of ASCE 7 have some differences in terms of roof zoning area and different peak Cp's.
- **OBJECTIVE #5:** Develop a machine learning model to predict surface pressure
  - Train the data obtained from the experimental testing to predict surface pressure coefficients.

1.5. Dissertation Structure

The remainder of this dissertation is organized into the following chapters:

Chapter 2 provides the design, construction, and pressure results of large-scale testing of scale 1:10 for different eight models with hip roof of two different slopes and three different overhang widths. The chapter goes through the methodology, instrumentation, and pressure coefficients that were captured among the surfaces of the walls, soffits, and overhangs.

Chapter 3 proposes the analytical program that comprises of a new codification study that was developed for roof overhangs design and an empirical model for wall and soffit correlations. The codification study is based on a statistical approach rather than the envelope approach with a reduction factor that has been commonly used before. The empirical model governs the correlation between wall pressure coefficient and soffit pressure coefficient for both positive and negative pressures.

Chapter 4 tackles the development of a machine learning models that can predict the pressure coefficients on the surfaces of walls and soffits based on training the experimental data from the wind tunnel testing.

Chapter 5 summarizes the major findings and contributions of this study in enhancing wind standards and code provisions.

Chapter 6 proposes a potential future work related to wind induced loads on roof overhangs.

CHAPTER II. LARGE-SCALE TESTING OF HIP ROOF WITH OVERHANGS

This chapter provides the design, construction, and pressure results of large-scale testing of scale 1:10 for different eight models with hip roof of two different slopes and three different overhang widths. The chapter goes through the methodology, instrumentation, and pressure coefficients that were captured among the surfaces of the walls, soffits, and overhangs.

2.1. Methodology

The large-scale experimental campaign was conducted at the Wall of Wind (WOW), Experimental Facility at Florida International University (FIU) (Gan Chowdhury et al. 2017). The 12-fan WOW has been designated by the National Science Foundation (NSF) as one of the nation's major "Experimental Facilities" (EF) under the Natural Hazards Engineering Research Infrastructure (NHERI) program. WOW serves as a distributed, multi-user national facility that provides the natural hazards research community with access to research infrastructure.

2.1.1. Test building

A hip-roof building layout was selected with roof slope 4:12, and full-scale dimension of eave height of 7.5 m and horizontal dimensions of 12.2 m by 15.24 m as shown in Fig.2.1. This configuration is commonly used in the residential market. Table 2.1 shows the prototype and model dimensions of the eight models considered. The eight models were named in this study from Model A to H. Model A to C had a roof slope 4:12 and an inclined overhang with width of 0.6 m, 1.2 m, 1.8 m, respectively, covered underneath with a horizontal soffit. Models D to F had a roof slope 6:12 with an inclined

overhang width of 0.6 m, 1.2 m, 1.8 m covered underneath with a horizontal soffit. The last two models (models G and H) had a roof slope 6:12 and inclined overhang width of 0.6 m, and 1.2 m, respectively, with no cover underneath (i.e., with no horizontal soffit). The latter models were tested for the purpose of comparison between the same models with horizontal soffit in terms of uplift pressure which are not presented in this study. The layout for the eight models is shown in **Fig.2. 2** to **Fig.2. 9**. The models were made of polycarbonate plastic sheets that were attached to a wooden frame to eliminate vibrations and built to a scale of 1:10.

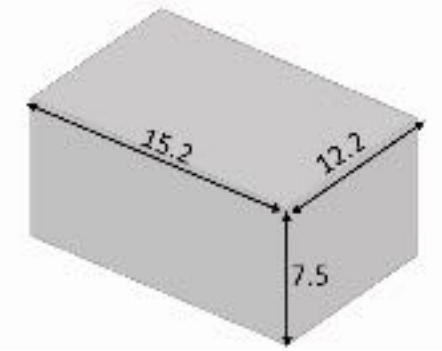

Fig.2. 1: Parent two-story building (full-scale dimensions in m)

Table 2. 1: Prototype and Models dimensions

Model	Model	Roof Slope	Building Dimensions		Scale	Model Dimensions		Notes
			L x W x h	Overhang		L x W x h	Inclined Overhang	
			(m)	(m)		(m)	(cm)	
A	Hip Roof	4:12 (18.4°)	15.2 x 12.2 x 7.3	0.6	1:10	1.52 x 1.22 x 0.73	6	With horizontal soffit
B				1.2			12	
C				1.8			18	
D		6:12 (26.3°)		0.6			6	
E				1.2			12	
F				1.8			18	
G				0.6			6	With inclined soffit
H				1.2			12	

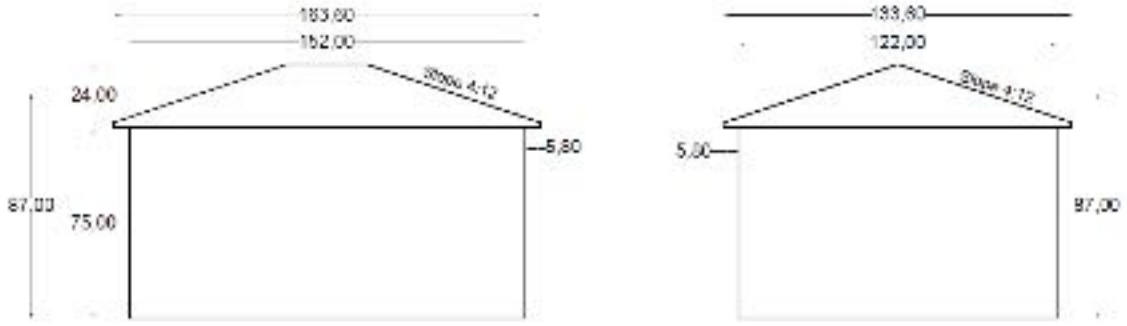

Fig.2. 2: Model A layout (a) Elevation View (b) Side View (all dimensions are at model-scale in cm)

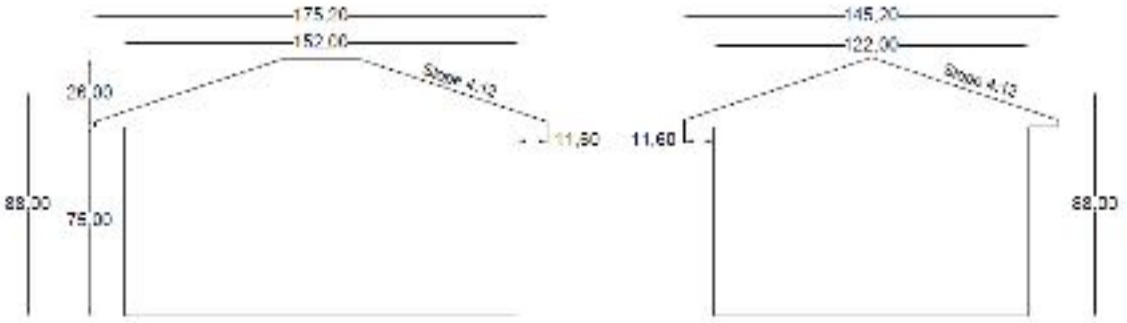

Fig.2. 3: Model B layout (a) Elevation View (b) Side View (all dimensions are at model-scale in cm)

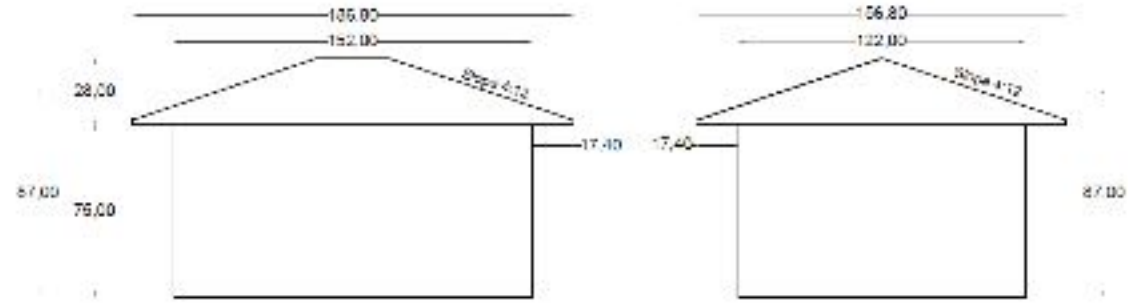

Fig.2. 4: Model C layout (a) Elevation View (b) Side View (all dimensions are at model-scale in cm)

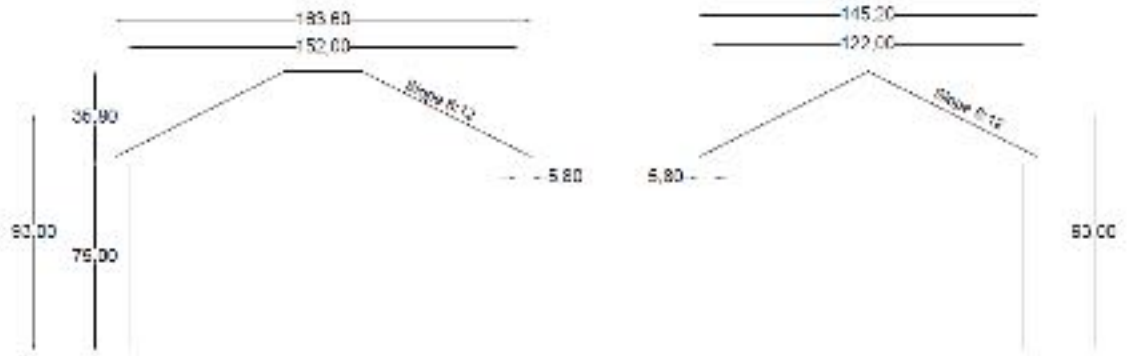

Fig.2. 5: Model D layout (a) Elevation View (b) Side View (all dimensions are at model-scale in cm)

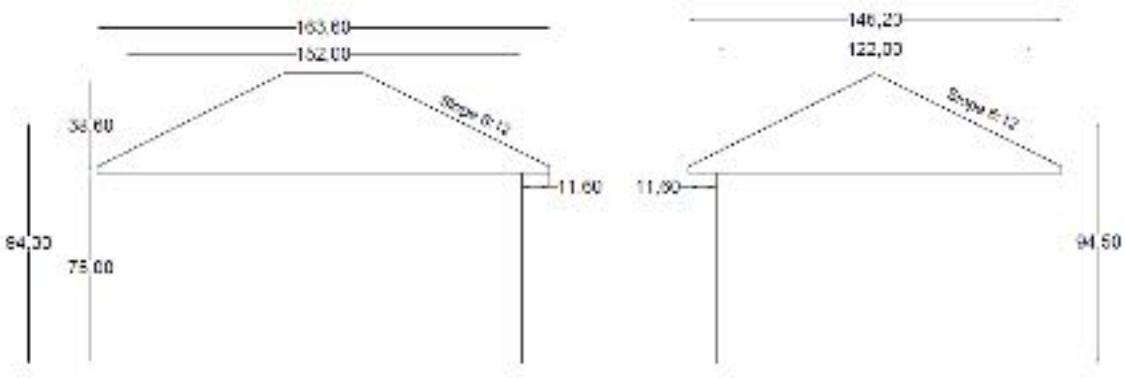

Fig.2. 6: Model E layout (a) Elevation View (b) Side View (all dimensions are at model-scale in cm)

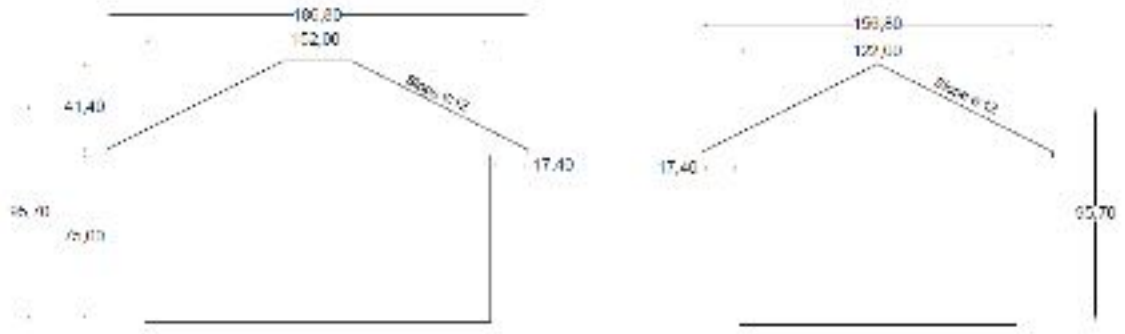

Fig.2. 7: Model F layout (a) Elevation View (b) Side View (all dimensions are at model-scale in cm)

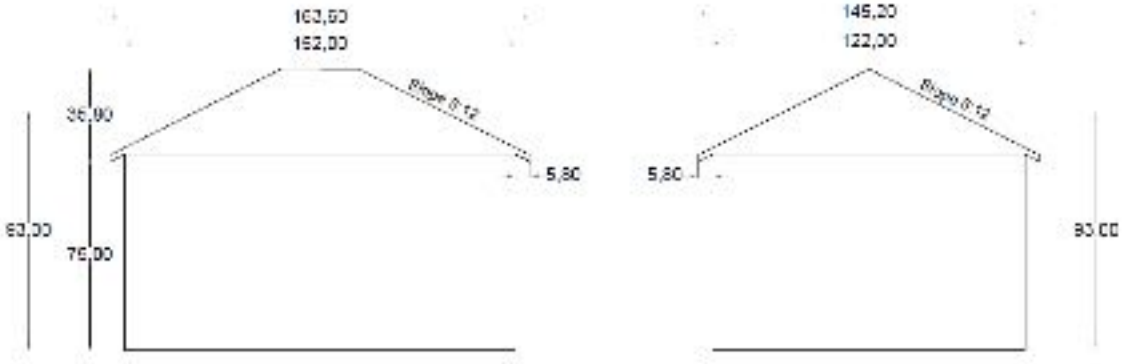

Fig.2. 8: Model G layout (a) Elevation View (b) Side View (all dimensions are at model-scale in cm)

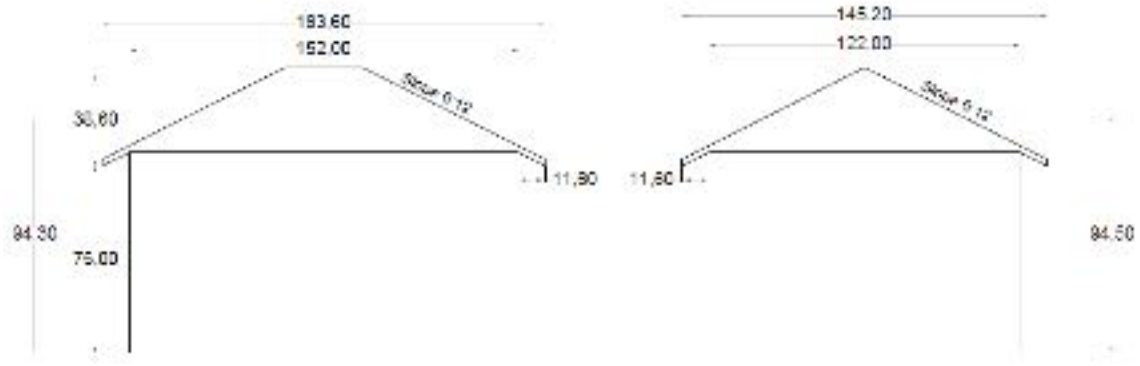

Fig.2. 9: Model H layout (a) Elevation View (b) Side View (all dimensions are at model-scale in cm)

2.1.2. Instrumentation and test protocol

All the models were equipped with pressure taps on the walls, the top surface of the overhangs and the bottom surface of soffits, as well as on the roof area adjacent to overhangs. The pressure taps on the roof and overhangs were placed within zone 3 and 2e as specified in ASCE 7-16 (**Fig.2. 10**), where a is defined in ASCE7-16 as follows: the smaller of 10% of the least horizontal dimension (shall not include any overhang distance) or 0.4h, where h is the roof mean height, and a shall not be less than either 4% of the least horizontal dimension or 0.9 m. The pressure taps were connected to a sensitive pressure scanning system (Scanivalve ZOC33). The maximum pressure that could be measured by this module is 2482 Pa (0.36 psi). The experimental tests were conducted for 40 wind directions for each model (i.e., 0° → 360° with increments of 10 degrees plus the four corners) as shown in **Fig.2. 11** with a target wind speed of 40 mph (17.88 m/s) generated by the fans. The sampling time for each direction was 60 seconds and the sampling frequency was 520 Hz. The eight 1:10 scaled models were tested for open terrain exposure roughness of zo=0.02 m, which is category 'C' per ASCE 7. The nominal wind speed at roof mean height varies according to each model and range from 0.87 m to 0.94 m due to

turbulence generated from the roughness elements and spires upstream of the turntable is 22.3 m/s.

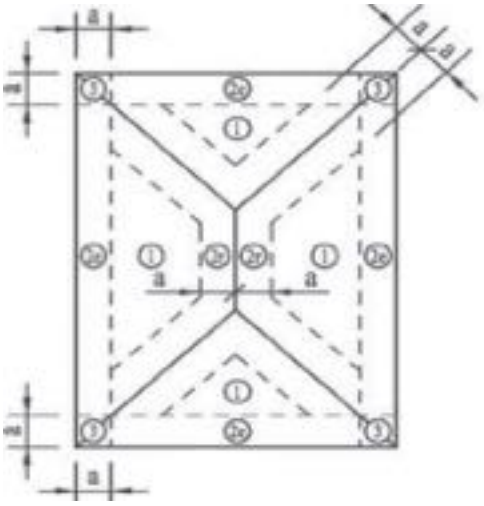

Fig.2. 10: Assigned zones for hip roof in ASCE 7-16

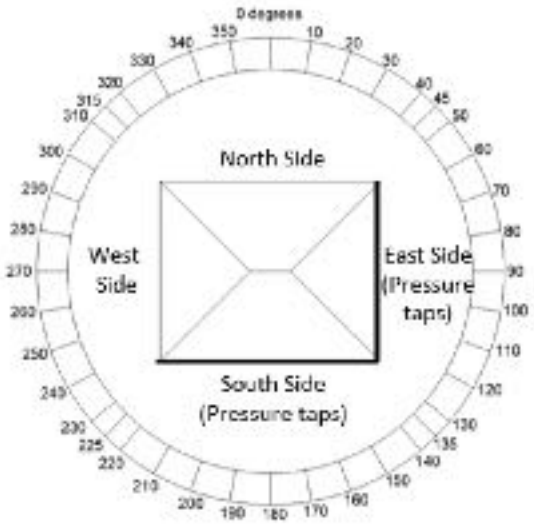

Fig.2. 11: Wind directions tested at the WOW

Each model has different number of pressure taps added on walls, soffits, roof with overhangs due to the variation in roof slope and roof overhang width (Mostafa et al. 2022). The pressure taps were added on two sides (walls, soffit, and roof with overhangs) of each model since the models were symmetric and were tested as shown in **Fig.2. 12** to **Fig.2. 14**. These two sides are identified as south and east sides. The south side corresponds to the 1.52 m wall and the east side corresponds to the 1.22 m wall. Pressure taps at each wall and adjacent overhang and soffit were placed with equal spacing for the evaluation of net pressure coefficients, pressure correlation and regression analyses. **Fig.2. 15** shows the two-story hip roof models tested in the WOW for both models and photographs of the two models on the turntable in the WOW, respectively.

Table 2. 2: Number of pressure taps in each model

Model	Pressure taps on roofs	Pressure taps on soffits	Pressure taps on walls	Total Number of Pressure Taps
A	128	86	130	344
B	112	92	100	304
C	148	112	102	362
D	106	72	100	278
E	112	92	100	304
F	136	116	100	352
G	106	72	120	298
H	112	92	120	324

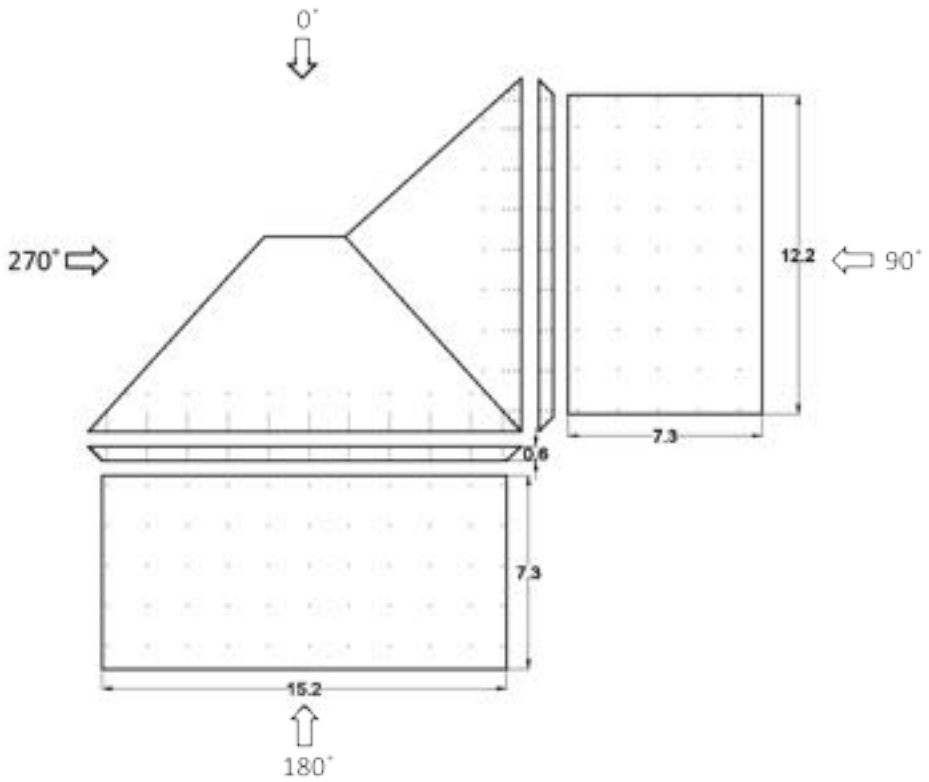

Fig.2. 12: Pressure taps layout on walls, soffits, and roof with overhangs of 0.6 m (m) – Model D

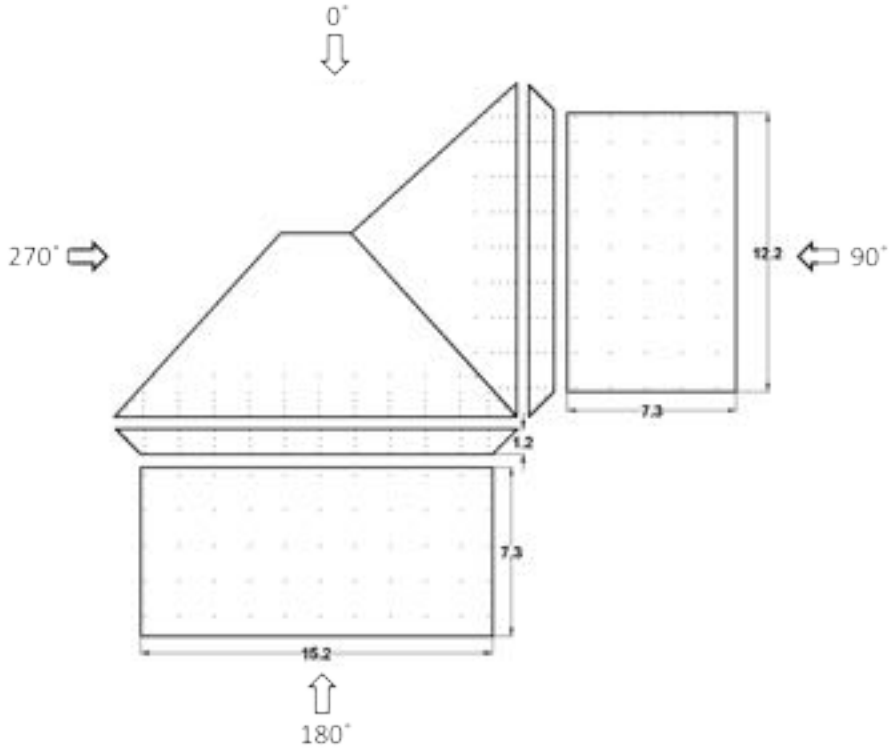

Fig.2. 13: Pressure taps layout on walls, soffits, and roof with overhangs of 1.2 m (m) – Model E

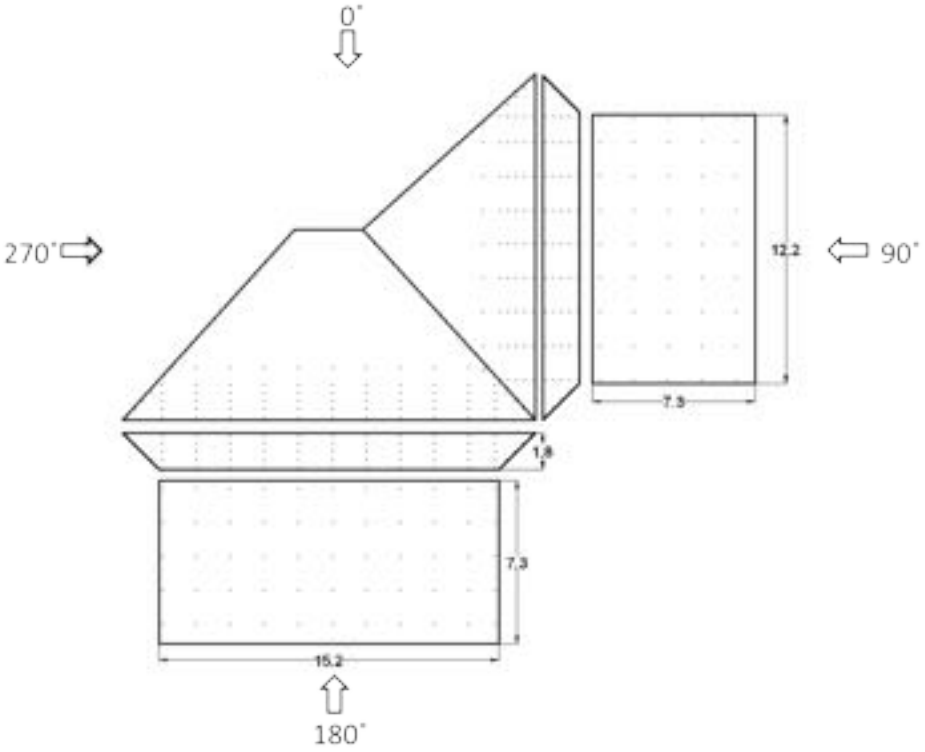

Fig.2. 14: Pressure taps layout on walls, soffits, and roof with overhangs of 1.8 m (m) – Model F

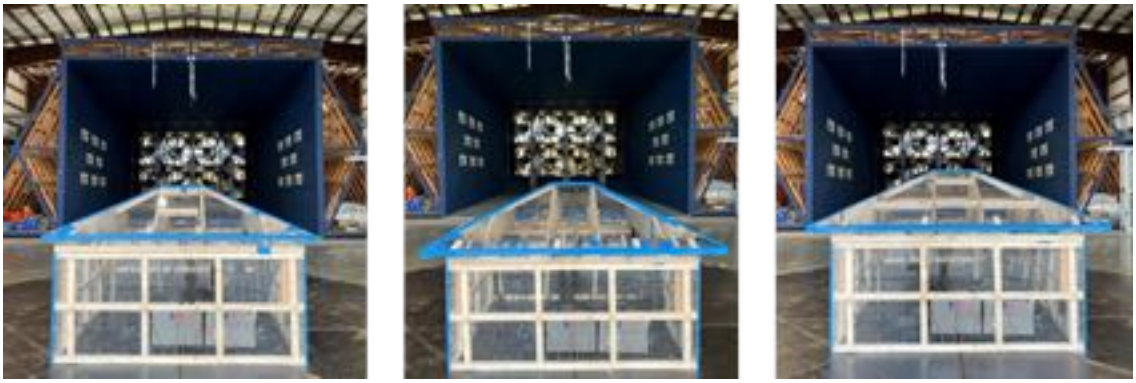

(a) (b) (c)

Fig.2. 15: Photograph for testing models on the turntable at the Wall of Wind (a) Model D (0.6 m) (b) Model E (1.2 m) (c) Model F (1.8 m)

2.2. Wind speed and turbulence intensity profiles

Wind speed profile measurements have been taken for the open terrain simulations before testing. Open terrain exposure (exposure C) was generated in the wind tunnel corresponding to surface roughness length, zo = 0.02 m. Different iterations were generated at the WOW to adjust the automated roughness element and spire angles to match the ESDU wind profile. The automatic roughness elements were placed at 15 degrees and spires were at 30 degrees. **Fig.2. 16** shows the wind speed and turbulence intensity profile for open terrain for scale 1:10 used at the WOW. The turbulence intensity profile did not match with the ESDU because of the missing low frequency and therefore was compensated by the post-test partial turbulence simulation (PTS) approach (Asghari Mooneghi et al. 2016; Banks et al. 2015; Guo et al. 2021; Mooneghi et al. 2016; Moravej 2018; Moravej et al. 2019). The PTS is an analytical method based on quasi-steady assumptions relying on the match of the non-dimensional power spectrum of the longitudinal turbulence and the large-scale and full-scale spectrum for high frequencies. The entire spectrum is obtained using gaussian probability distribution for the low-

frequency effects with the high frequency data obtained during testing in the wind tunnel. The peak pressure coefficient is estimated by dividing the sample time (60 sec) into subintervals where peak values could be treated as independent, while the full-scale sampling time of one hour is a sufficient sampling time to achieve stable statistics when measuring fluctuating wind loads. The number of sub-intervals used was 100 (the max number that can be used was 180 according to some calculated values related to the t-gust, time ratio and cut off frequency as specified in the PTS approach) and the time of each subinterval was 0.6 second. The partial turbulence simulation method uses Fisher Tippet Type 1 distribution in estimating the probability of the peak pressure coefficient for not exceeding that peak pressure coefficient in the subinterval. The peak pressure coefficient for each interval is calculated based on the peak pressure and the mean velocity of the full sample period with full spectrum turbulence and it is based on mean hourly dynamic pressure. The peak pressure coefficient for 3 sec is obtained by rescaling using equation 4 which is based on 3-second gust (Durst 1960) dynamic pressure. The wind spectrum was compared to the Von Karman spectrum at full scale for open terrain (**Fig.2. 17**) - note that for open terrain zo ranges from 0.01 m to 0.15 m according to table C26.7-1 in ASCE7-16. The PTS approach accounts for the deviation between the normalized area under the curve for the wind tunnel spectrum and Von Karman spectrum, as described in the ASCE 49-21 standard (ASCE 2022).

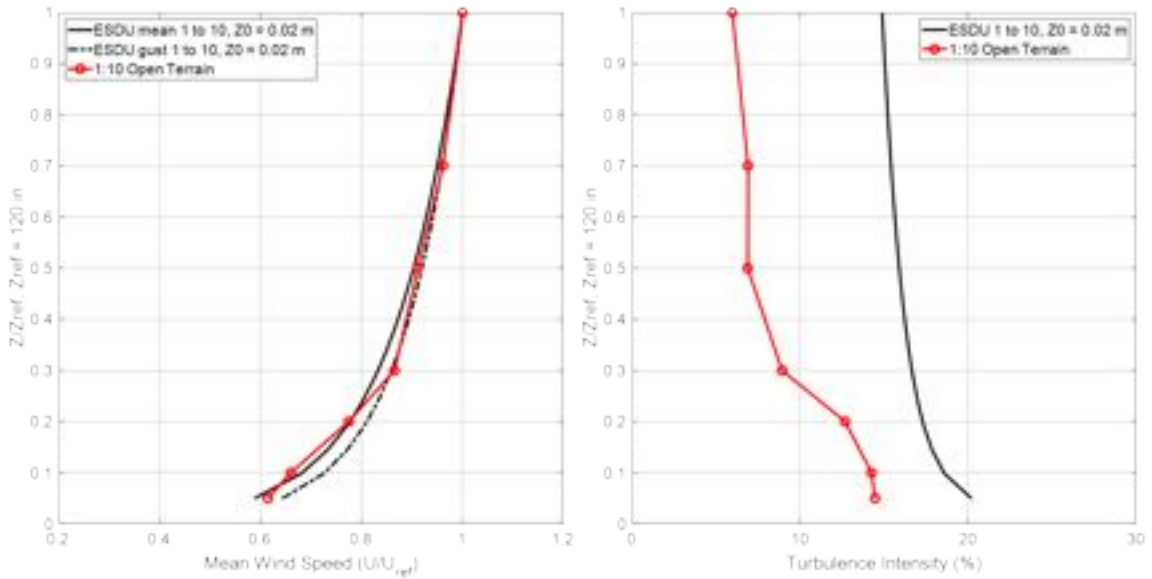

Fig.2. 16: Wind speed and turbulence intensity profile for open terrain setup for 1:10 scale.

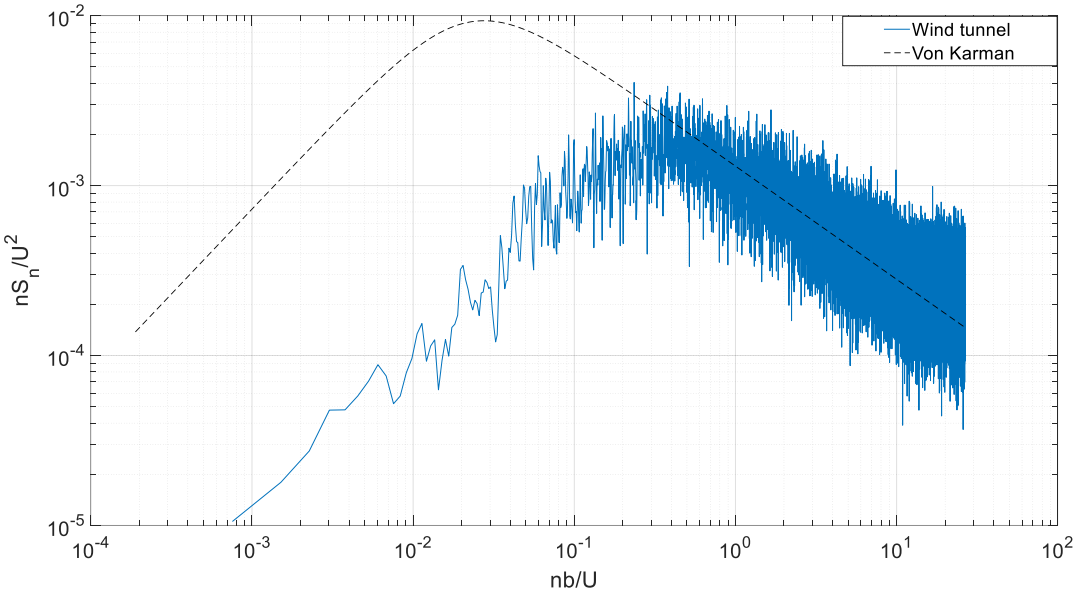

Fig.2. 17: Wind spectra at roof mean height 87.5 cm (34.5 in) for open terrain

2.3. Results & Discussions

Data analysis was performed on the data acquired from the conducted experimental testing to measure the peak and mean pressure coefficients among the surfaces. This section discusses the pressure coefficients as peak and net pressure coefficients between

the upper surface of the overhangs and the soffit surface. In addition, the pressure fluctuations between the wall taps and soffit taps are discussed with the regression and correlation coefficient analysis between the wall taps and adjacent soffit taps.

2.3.1. Pressure coefficients

The acquired raw data from each pressure tap measure the relative pressure between the pressure at the tap location and the static pressure at the WOW ambient pressure in psf. First, a transfer function was applied for correction of the tubing distortion - a onetime process done for any wind testing project using flexible tubing to connect pressure taps to the pressure scanners. The pressure tubing was a regular Alphawire single black tubing (PVC 105-16) of an internal diameter 0.135 cm. The tap side length that was used for all the pressure taps was 19.3 cm, while the connector side was 30.5 cm. The transfer function was applied according to the used tap side length. The transfer function process consists of a Labview code generating random white noise data as analog signals to a pressure signal generator (i.e. audio amplifier). The distortion of pressure signals caused by the tubing is compensated for using the inverse transfer function method described (Irwin et al. 1979) and a low pass filter at 250 Hz is applied. The transfer function causes the deviation RMS between the long tubing data and short tubing data to reach $2x10^{-4}$. Afterwards, the PTS approach was applied to calculate peak pressure coefficients. The model parameters for PTS (Table 2) were calculated from the wind flow profile using cobra probes at different heights, while the prototype parameters were calculated using ESDU 84011 and 83040 (ESDU,1993a, ESDU,1993b) for variation of wind speed and turbulence intensity, respectively.

Table 2. 3: PTS parameters for open terrain

Parameter	Prototype		Model	
Iu (%) Turbulence Intensity	Iu_p	20.0	Iu_m	8.11
Lu (m) Integral Length Scale	Lu_p	82.2	Lu_m	0.313
H (m) Roof height	b_p	8.763	b_m	0.8763
V (m/s)	U_p	33	U_m	16.80
test time (minutes)	T_p	60	T_m	1

As mentioned earlier, the pressure scanning modules used in the aerodynamic test measure the relative pressure in psf. These pressure values are presented here as normalized pressure coefficients (C_p) computed using equation 1, where ΔP is the relative pressure at the tap location, ρ is the standard air density $1.225\ kg/m^3$, V_{ref} corresponds to reference wind speed at specified height which is in this study the mean wind speed at mean roof height 87.0 cm. It is important to note that the air density value while testing was 1.194 kg/m^3, which was used in data processing. Consequently, statistical pressure coefficient parameters were also computed by using their corresponding pressure change parameters, as shown in equations 2 and 3. Peak pressure coefficients are referred to as the minimum (highest suction/negative pressure) and maximum (highest positive pressure). Importantly, note that for any positive sign represents a pressure directed towards the surface while a negative sign represents a pressure directed away from surface (suction). Throughout this study, peak pressure coefficients were identified either as local (single tap) or area-averaged (two or more taps).

$$Cp = \frac{\Delta P}{0.5\ \rho\ V_H^2} \tag{1}$$

$$C_{p\,mean} = \frac{P_{mean}}{0.5\rho V_H^2} \quad (2)$$

$$C_{p\,peak} = \frac{P_{peak}}{0.5\rho V_H^2} \quad (3)$$

$$Cp_{peak\ 3-\text{sec}} = Cp_{peak}\ (\frac{V_H}{V_{3-sec}})^{\,2} \quad (4)$$

Where, V_H is the wind speed at roof mean height, V_{3-sec} is the peak wind speed averaged over 3 sec.

2.3.2. Peak pressure coefficients

In total, 40 wind directions were tested (see **Fig.2. 11**) to determine the peak max and min C_p for each pressure tap time history record. **Fig.2. 18** to **Fig.2. 23** show the peak max/min pressure coefficients for models A to F, respectively at 180˚ wind direction for the south walls, soffits, and roofs. For model A at wind direction of 180˚, the peak min Cp near the overhang corner was -3.9, and for model B the peak min C_p near the overhang corner was -3.3, while for model C the peak min C_p near the overhang corner was -2.7. The same for model D, E and F, the peak min Cp was -3.2, -3.0 and -2.4, respectively. It is apparent that the 0.6 m overhang was exposed to higher peak min C_p near the edge compared to the 1.2 m and 1.8 m overhang for both roof slopes. This can be attributed to the high velocity in the vertical direction towards the edge, due to the walls that lead part of the flow over the roof (Wiik and Hansen 1997). Moreover, it is apparent that the overhangs of roof slope 4:12 are exposed to higher suction compared to overhangs of roof slope 6:12. In both cases, the peak max C_p at the center of the soffit was 1.2 - 1.4 at 180˚ wind direction and the peak max at the upper part of the wall was 1.4 at 180˚ wind direction. In the following figures, C.L is a denotation to a cut line.

Overhang = 0.6 m (South Side)	Roof Slope 4:12 	W. D = 180˚ 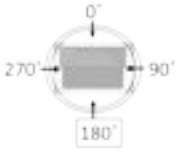

Min Peak C_p of overhang with part of roof

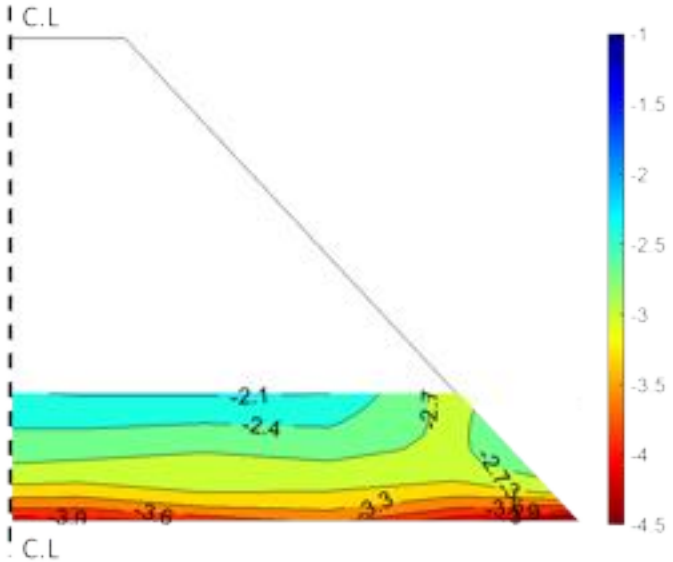

Max Peak C_p of soffit

Max Peak C_p of wall

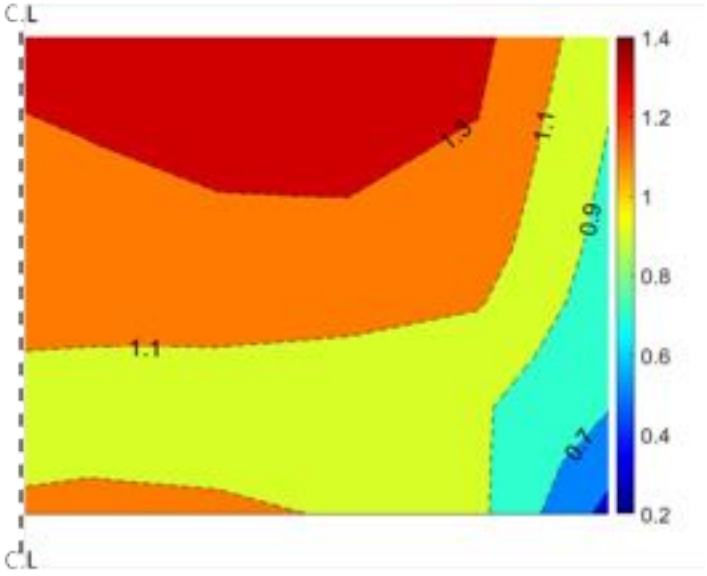

Fig.2. 18: Pressure coefficient contour plots for Model A at wind direction of 180º

Overhang = 1.2 m (South Side)	Roof Slope 4:12 	W. D = 180˚ 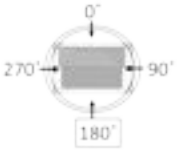

Min Peak C_p of overhang with part of roof

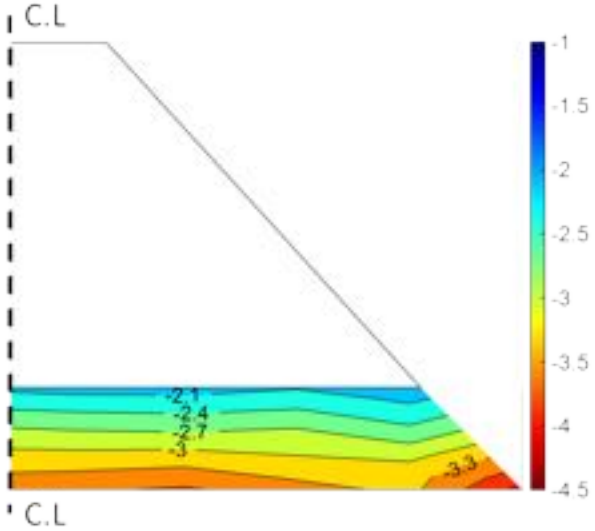

Max Peak C_p of soffit

Max Peak C_p of wall

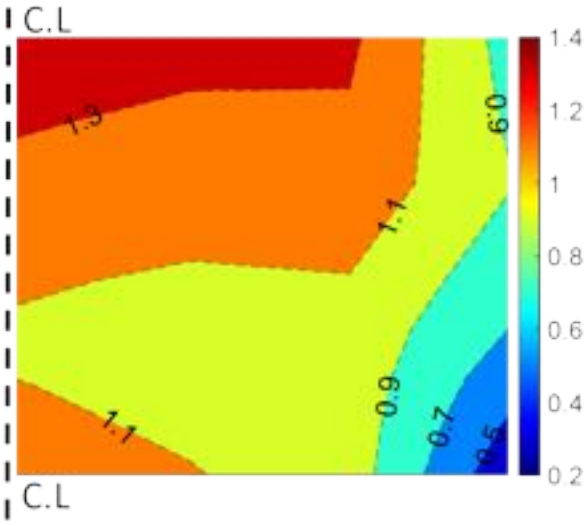

Fig.2. 19: Pressure coefficient contour plots for Model B at wind direction of 180º

Overhang = 1.80 m (South Side)	Roof Slope 4:12 	W.D= 180˚ 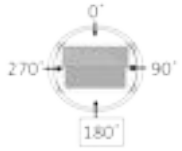

Overhang with part of roof- Min Peak C_p

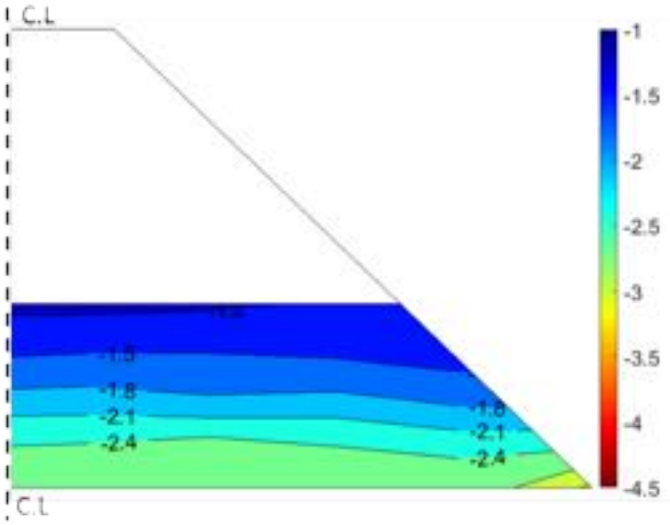

Soffit-Max Peak C_p

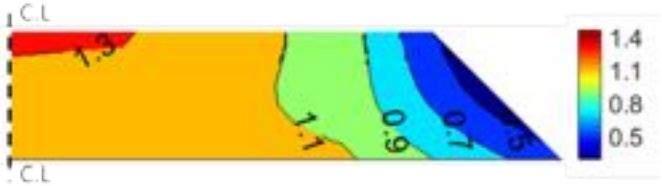

Wall-Max Peak C_p

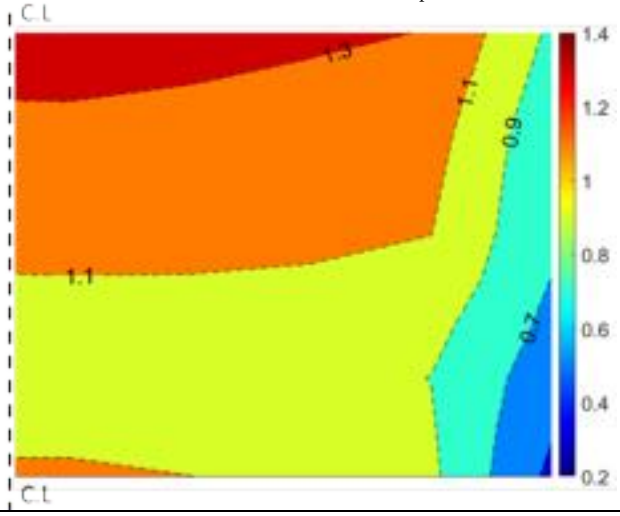

Fig.2. 20: Pressure coefficient contour plots for Model C at wind direction of 180º

Overhang = 0.6 m (South Side)	Roof Slope 6:12 	W.D= 180˚ 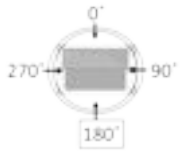

Overhang with part of roof- Min Peak C_p

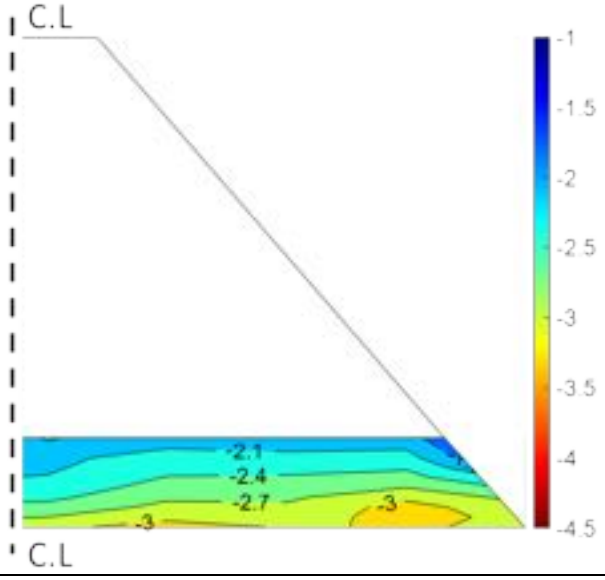

Soffit-Max Peak C_p

Wall-Max Peak C_p

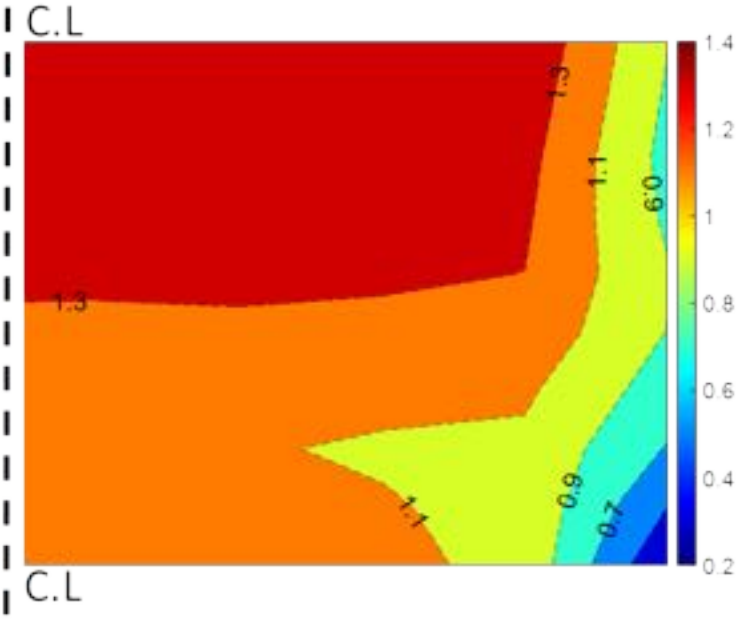

Fig.2. 21: Pressure coefficient contour plots for Model D at wind direction of 180º

Overhang = 1.20 m (South Side)	Roof Slope 6:12 	W.D= 180˚ 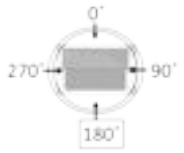

Overhang with part of roof- Min Peak C_p

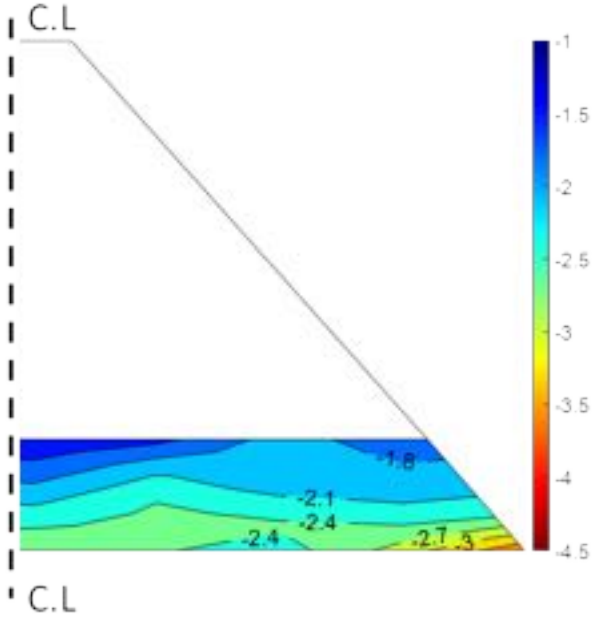

Soffit-Max Peak C_p

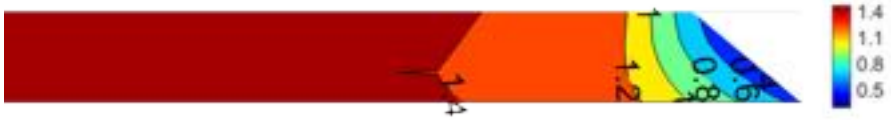

Wall-Max Peak C_p

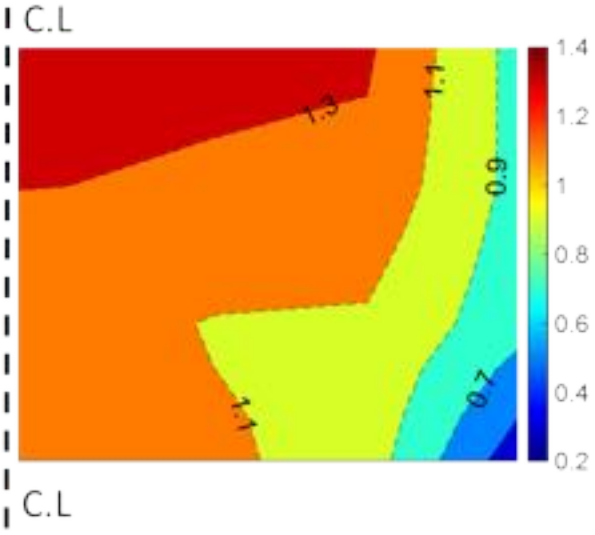

Fig.2. 22: Pressure coefficient contour plots for Model E at wind direction of 180º

Overhang = 1.80 m (South Side)	Roof Slope 6:12 	W.D= 180˚ 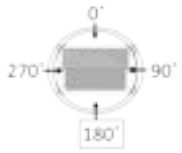

Overhang with part of roof- Min Peak C_p

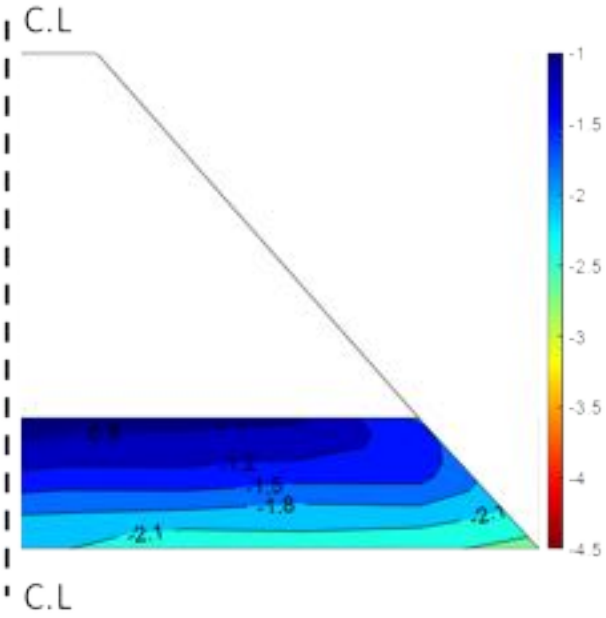

Soffit-Max Peak C_p

Wall-Max Peak C_p

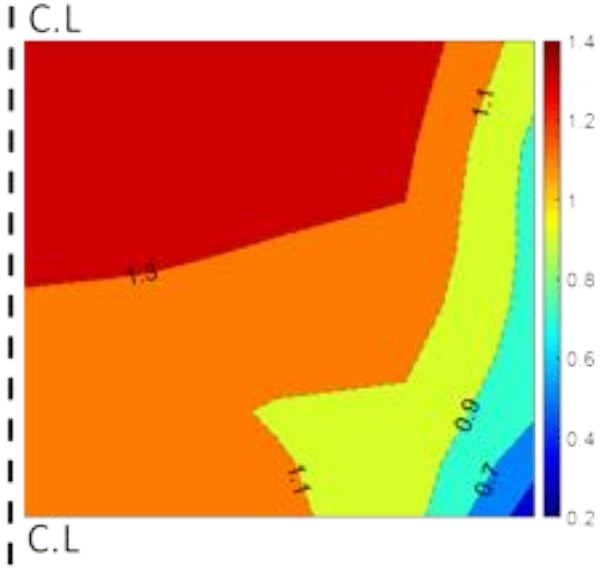

Fig.2. 23: Pressure coefficient contour plots for Model F at wind direction of 180º

2.3.1. Net pressure coefficients

Instrumenting the overhangs with pressure taps at both upper and lower surfaces allows for separate monitoring of pressure coefficients at either surface (C_p, overhang; C_p, soffit) or their simultaneous effect at the same location of the overhang (C_p, net). This allows for a clearer understanding of the net pressure coefficient behavior and its correlation to the upper taps of the underneath wall. The C_p, net was calculated twice, first by subtracting the C_p time history for overhang upper surface taps by corresponding lower surface taps (soffit) at the same locations and second for the overhang upper surface taps with the corresponding wall upper taps, then PTS was applied as previously to get the peak C_p, net. This approach was implemented to investigate the similarity between C_p, net between overhang taps and soffit taps versus overhang taps and wall taps. This analysis was implemented on two of the models (A and C) which have the narrowest and widest overhangs, and it was found that there was a small difference between the C_p, net using the lower surface taps or using the wall taps. The reason is that the pressure/suction on the overhang upper surface is controlling the net pressure coefficients causing only small differences between the net pressure using soffit taps versus wall taps (Mostafa et al. 2022b). For model A, all wind directions result in similar net pressure coefficients when using the two approaches. Likewise, for model C, the two approaches show similar net pressure coefficients for the predominant positive wind directions, such as 180º, while wind directions that induce suctions, such as 270º, show some differences between the net pressure coefficients. For instance, at wind direction of 270º the peak C_p , net is -1.9 when the soffit pressure is subtracted, and -1.50 while applying overhang upper surface pressure to upper wall pressure. **Fig.2. 24** shows the representative azimuthal graph for wind

directions of 180º and 270º for model C. Higher absolute net pressure coefficients occurred when the soffit pressures were used, in all other wind directions.

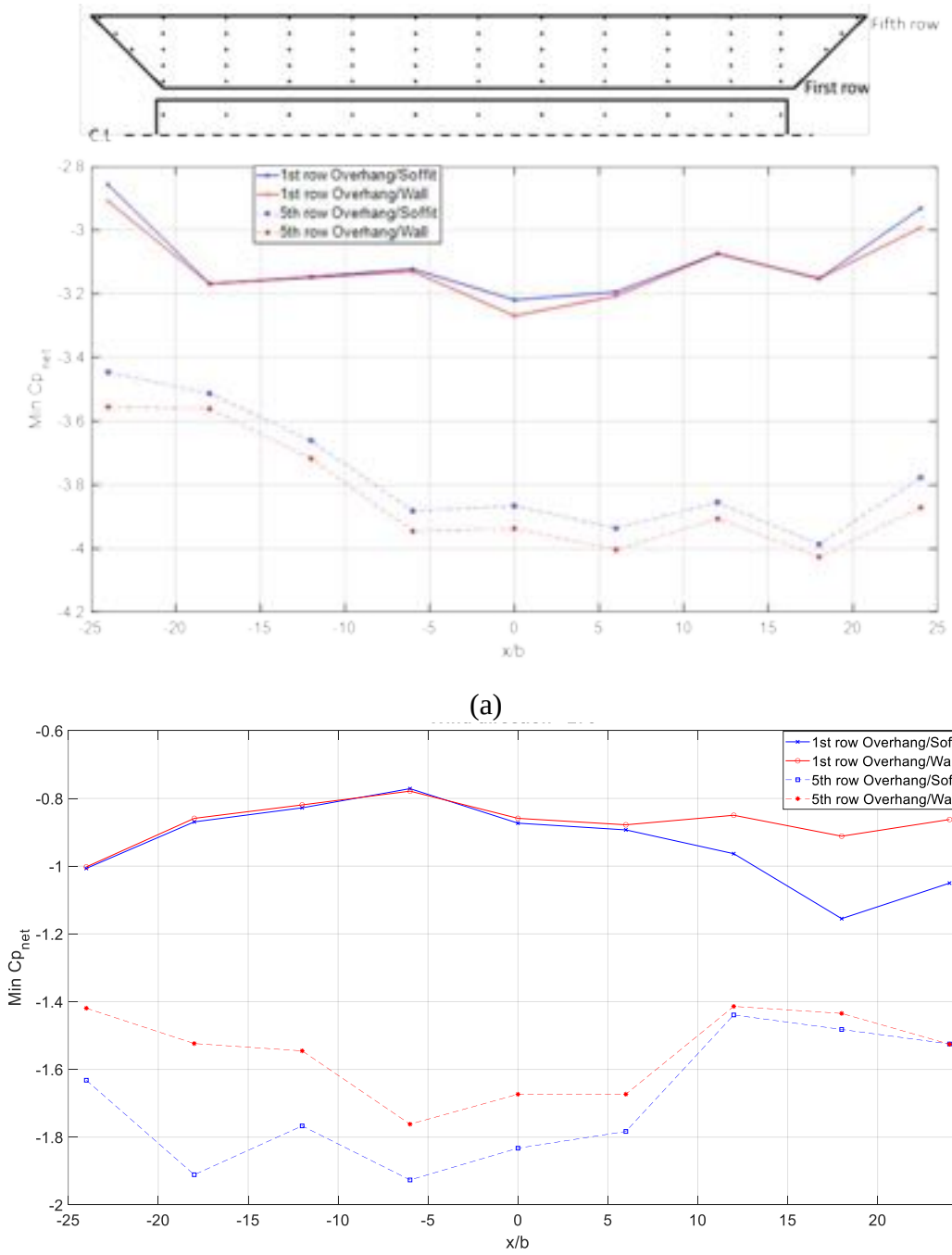

Fig.2. 24: Net Pressure coefficient contour plots for south overhang for Model C (a) W.D of 180º (b) W.D of 270º

2.3.2. Correlation and regression analysis of wind pressures on soffits and adjacent walls

The pressure taps in walls and soffits were placed with equal spacing, to compare the C_p of upper taps on the wall with the adjacent taps on the soffit using correlation and regression analysis. For all the figures that include the wall and the soffit, the shorter side of the soffit is the wall side (lower side), and the longer side of the soffit is the edge side (upper side). The taps shown in the dashed box in **Fig.2. 25** used as sample taps for comparison between soffits and wall pressure fluctuations along wind directions, while the taps in the solid box used to derive the correlation coefficients, correlation contour plots, and perform the regression analysis. This part of analysis shows the results and discussion for models D, E, and F, as a sample of comparison between three different overhang width with the same roof slope (6:12).

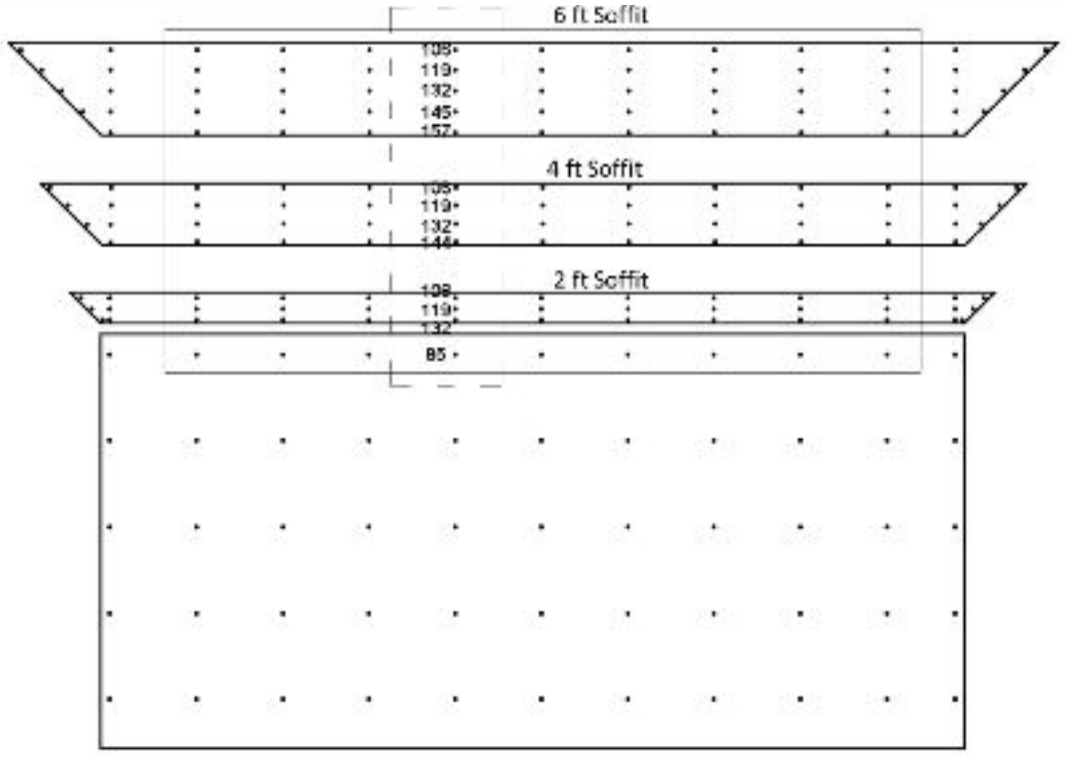

Fig.2. 25: Walls and soffits pressure taps used in regression and correlation analysis

2.3.3. Pressure fluctuations at the middle taps of the soffit/wall

One of the upper taps in south wall (tap 85) was used to display the similarity in pressure fluctuations between the upper taps of the wall with the corresponding taps in the soffit (**Fig.2. 25**). The peak max and peak min pressure coefficients of one of the upper taps in south wall (taps 85) were compared with the adjacent soffit taps (106, 119 and 132), (106, 119, 132 and 144), (106, 119 132, 145 and 157) of model D, E and F, respectively for the 40 wind directions. **Fig.2. 26** displays the peak max and peak min for the chosen wall and soffit taps for all wind directions. It is apparent that the peak max C_p's were similar along the adjacent taps in all wind directions. In contrast, the peak min C_p's used to slightly change for soffit taps located away from the wall. For instance, for wind directions from 135º to 225º, the wall and soffit taps were mainly exposed to positive pressure, thus, the peak min C_p ranged from 0 to -0.5, while the positive C_{ps} values were very similar and ranged from 0.6 to 1.45. This supports the assumption in ASCE 7-16 and ASCE 7-22 that the pressure coefficient at the bottom covering of the roof overhang shall be taken as the external pressure coefficient on the adjacent wall surface. The edge pressure taps in the soffit experienced more suction compared to the middle or the inner row. The soffit is exposed to more turbulence underneath and this turbulence increased near the edge where more separation occurs. Consequently, pressure taps at the soffit edge had higher peak min C_p than the middle and inner taps. It is important to note that tap 85 on the wall is not the middle tap, but shifted towards one of the sides, thus the pressure fluctuations are not symmetric between 90˚ and 270˚.

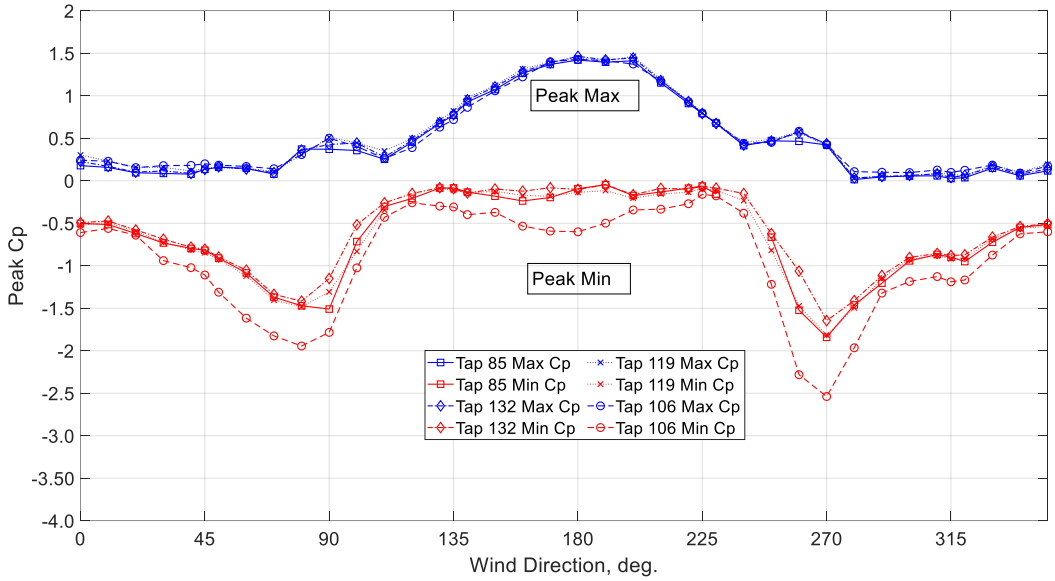
Peak Max
Peak Min
Tap 85 Max Cp
Tap 85 Min Cp
Tap 132 Max Cp
Tap 132 Min Cp
Tap 119 Max Cp
Tap 119 Min Cp
Tap 106 Max Cp
Tap 106 Min Cp
Peak Cp
Wind Direction, deg.

(a)

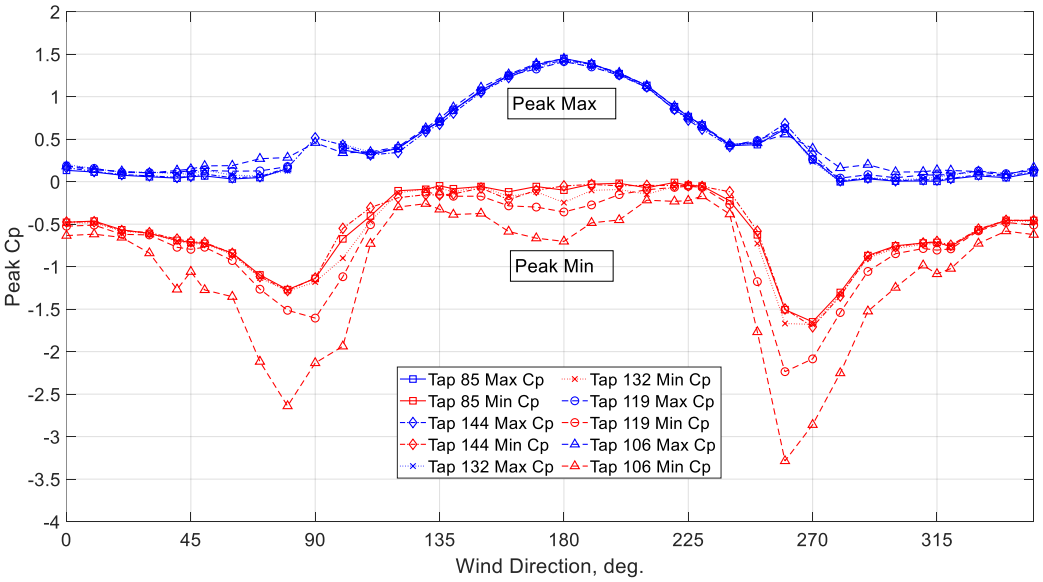
Peak Max
Peak Min
Tap 85 Max Cp
Tap 85 Min Cp
Tap 144 Max Cp
Tap 144 Min Cp
Tap 132 Max Cp
Tap 132 Min Cp
Tap 119 Max Cp
Tap 119 Min Cp
Tap 106 Max Cp
Tap 106 Min Cp
Peak Cp
Wind Direction, deg.

(b)

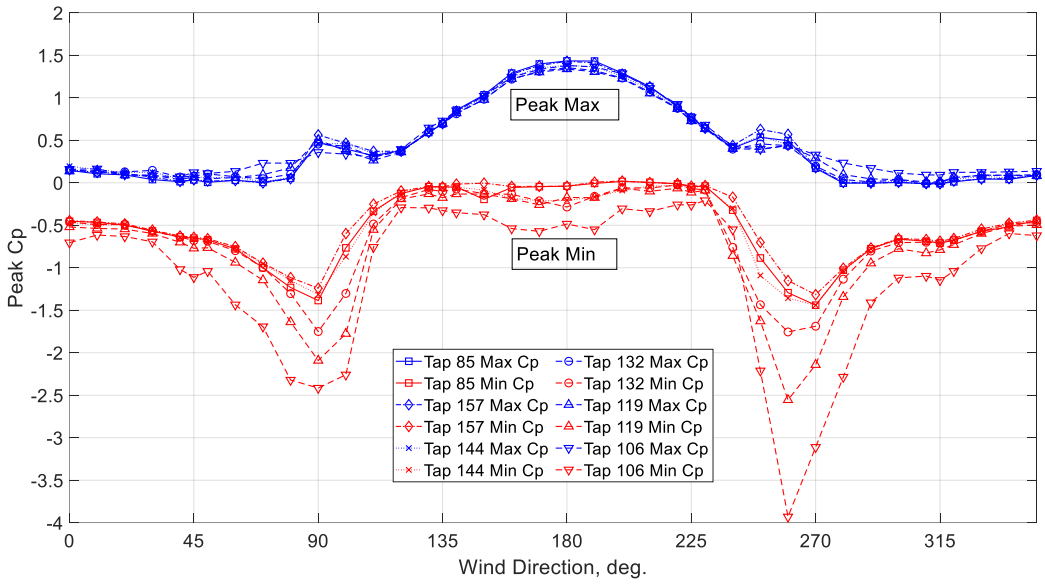

(c)

Fig.2. 26: Peak Max and Peak Min for one of the upper wall taps with adjacent soffit taps for (a) Model B (b) Model C (c) Model D

2.3.4. Correlation Coefficients between taps of soffit/wall

Correlation coefficients were analyzed between the C_p time series of soffit taps with upper wall taps as shown in the solid box in (**Fig.2. 25**). **Fig.2. 27** to **Fig.2. 29** provide correlation coefficient contour plots for south soffit for model D, E, and F, respectively, for four wind directions (0˚, 90˚, 180˚ and 270˚). For all the soffit plots the wall side is the upper side of the plots, and the soffit edge is the lower side of the plots. Generally, wall taps are well correlated with soffit taps near to the wall. The R factor ranges from 0.68 to 0.98 for model B and C, and ranges from 0.6 to 0.96 for model F. The highest correlation occurred when the south wall and the adjacent soffit were at the windward (wind direction 180°) or in the wake region (wind direction 0°), i.e., the wall and the soffit were exposed to predominantly positive pressure or predominantly suction, respectively. Model D and E show almost the same correlation coefficient when the models are placed in the windward

(180º degree), and the correlation coefficient at the corner significantly decreases for model F when placed in the windward direction. The correlation coefficients for models D and E are significantly higher at the outer edges compared to model F, for all other shown directions. This indicates that the correlation coefficients for wider overhang significantly decrease compared to narrower overhangs, especially when the taps are exposed to suctions. For instance, at wind direction 90° and 270°, suction occurred at the south and separations caused more turbulence underneath the soffit that caused reduction in correlation coefficients. It was concluded that the soffit pressure is less correlated with the wall at the outer edges compared to the near wall surfaces.

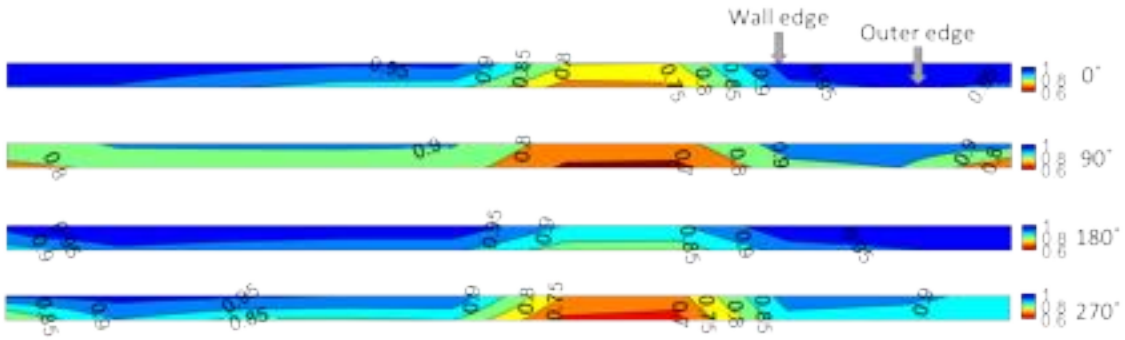

Fig.2. 27: Correlation Coefficients contour plots for south soffit – Model D

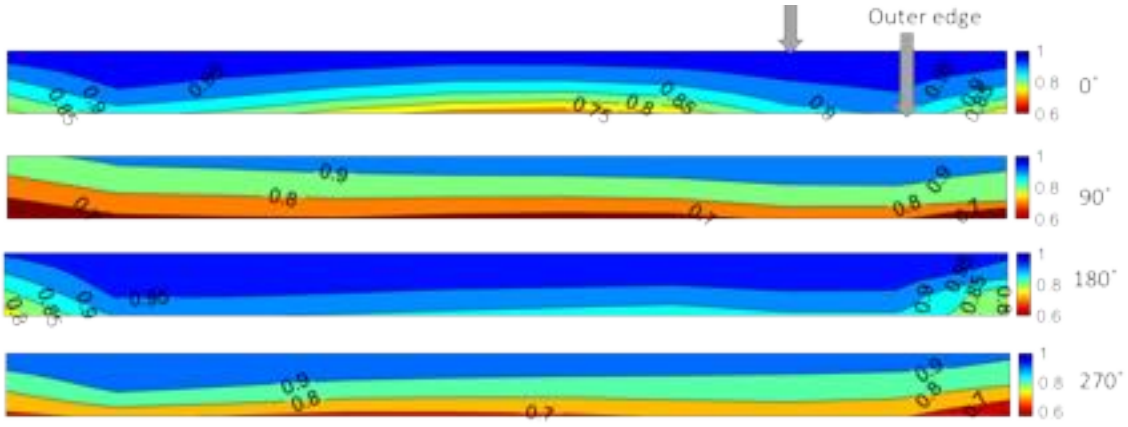

Fig.2. 28: Correlation Coefficients contour plots for south soffit – Model E

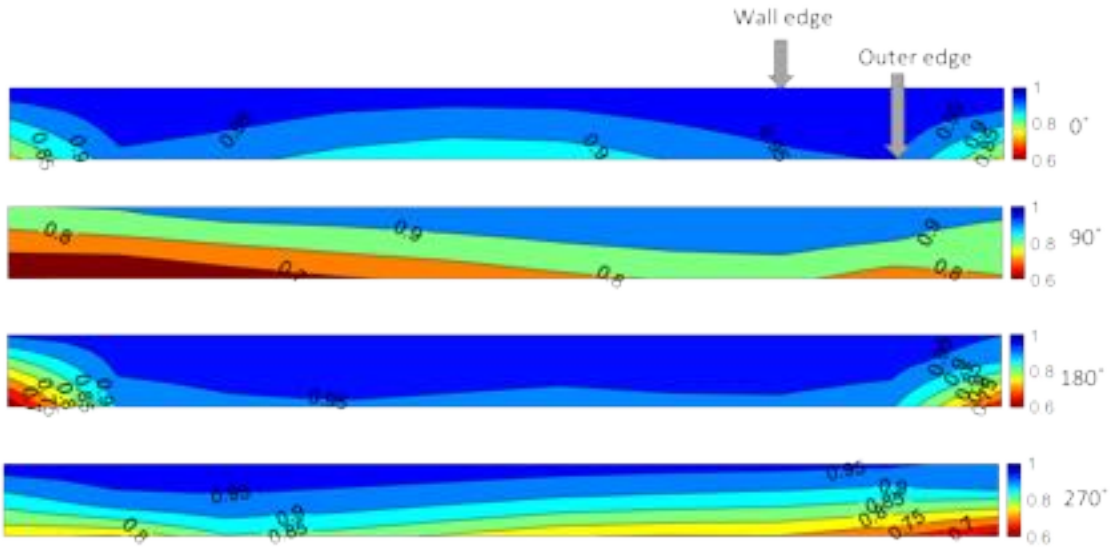

Fig.2. 29: Correlation Coefficients contour plots for south soffit – Model F

2.3.5. Overhangs with covered and uncovered soffits (Uplift pressure)

Wind tunnel tests were carried out on two additional models (models G and H) which have the same roof slope and overhang widths with models D and E respectively, but with uncovered soffits as shown in **Fig.2. 8** and **Fig.2. 9**. The aim of testing these two models was to investigate the effect of uncovered soffits (inclined soffits) on pressure coefficients variation compared to covered soffits (horizontal soffits). In addition, it was important to analyze the difference in uplift forces and uplift pressures between the covered and uncovered soffits. Data analysis which included correlation coefficients, regression analysis, peak pressure coefficients, and uplift forces was carried out on these two models. Overall, it was found that there is not much difference between the two soffit cases in terms of regression analysis, peak pressure coefficients and correlation coefficients.

A comparison between the uplift forces for the two models was also carried out. First, the uplift forces were calculated for each pressure tap as a function of the net pressure coefficient between the upper and lower surface of the overhang and the tap tributary area

using equation 5. The wind-induced pressure is a function of the applied wind speed; thus, a wind speed of 156 mph which is a category 5 hurricane was used in calculating the forces. It is important to note that the comparison between the uplift pressure for different overhangs is not affected by the assigned value of wind speed, while the magnitude of each uplift force/pressure is affected by the applied wind speed value. For instance, at wind direction of 180˚, the uplift pressures are -10.5 KN/m^2 (-221 lb/ft^2) and -9.5 KN/m^2 (-198 lb/ft^2) for models D and E, respectively as shown in **Fig.2. 30** and **Fig.2. 31**. These values are dependent on the wind speed but in terms of comparison between the uplift pressure, model D is exposed to higher uplift pressure than model E regardless the wind speed value. The uplift pressure over the total surface area of the overhangs is calculated as the summation of forces for each pressure tap over the summation of the tributary areas for all pressure taps. This procedure was applied for all the 40 wind directions. The uplift pressures were plotted with the wind direction, as shown in **Fig.2. 30** to **Fig.2. 33**. It is apparent that for the same overhang width, the uplift pressures over the total surface area of the overhangs are similar for covered and uncovered soffits. Clearly, the 2 ft overhang (model D) is exposed to higher uplift pressures compared to the 4 ft overhang (model E), and this was expected due to the smaller surface area of the 2 ft overhang.

$$F_{L(i)\theta} = C_{p(i)\theta} * 0.5 * \rho * V^2 * A_i \quad (5)$$

$$P = \frac{\sum_i^n F_L}{\sum A_i} \quad (6)$$

where, F_L is the uplift force for tap (i) at wind direction (θ), $C_{p(i)\theta}$ is the 3-sec peak net pressure coefficient for the upper taps and the lower taps on the same location on the

overhangs at wind direction (θ), ρ is the air density, V is the wind speed, A_i is the tributary area of tap (i), and P is the uplift pressure at the total surface area of the overhang.

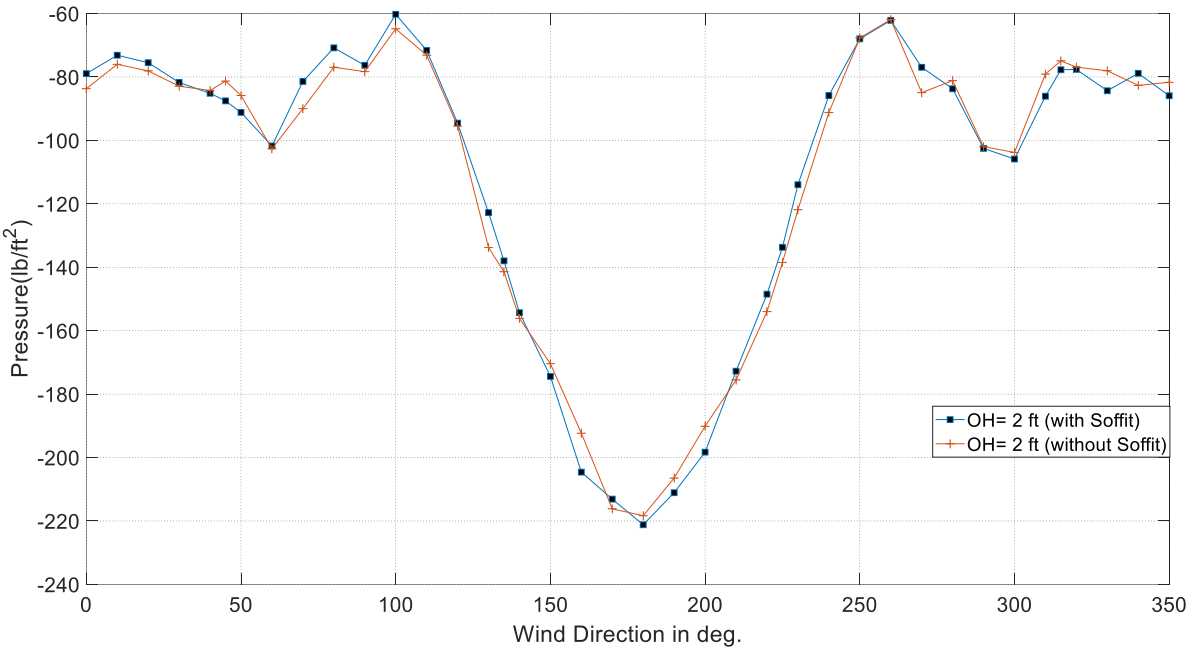

Fig.2. 30: Uplift pressure over the 2 ft overhang surface area along wind directions for covered and uncovered soffits

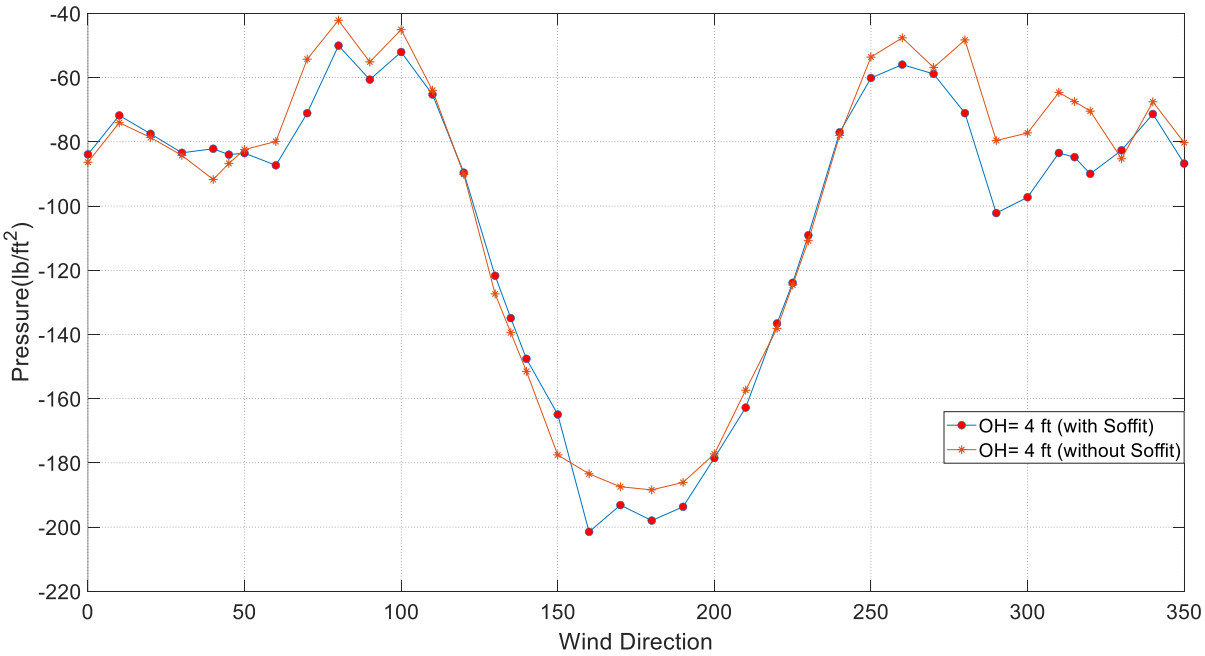

Fig.2. 31: Uplift pressure over the 4 ft overhang surface area along wind directions for covered and uncovered soffits

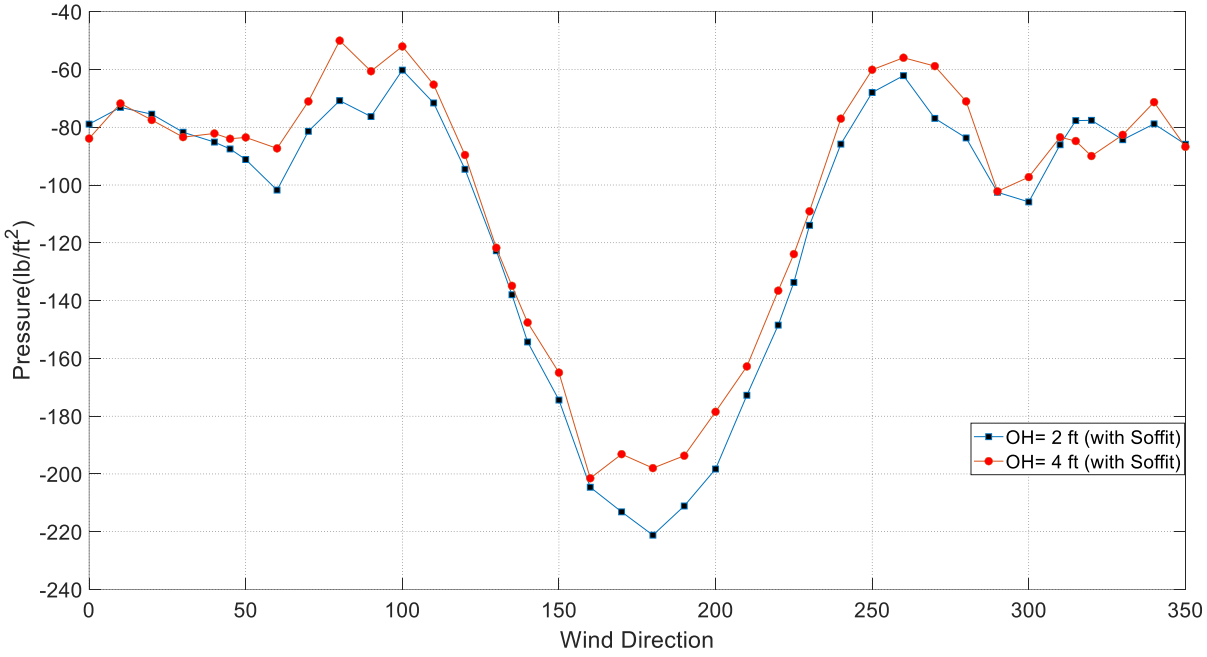

Fig.2. 32: Uplift pressure over the 2 ft and 4 ft overhang surface area along wind directions for covered soffits

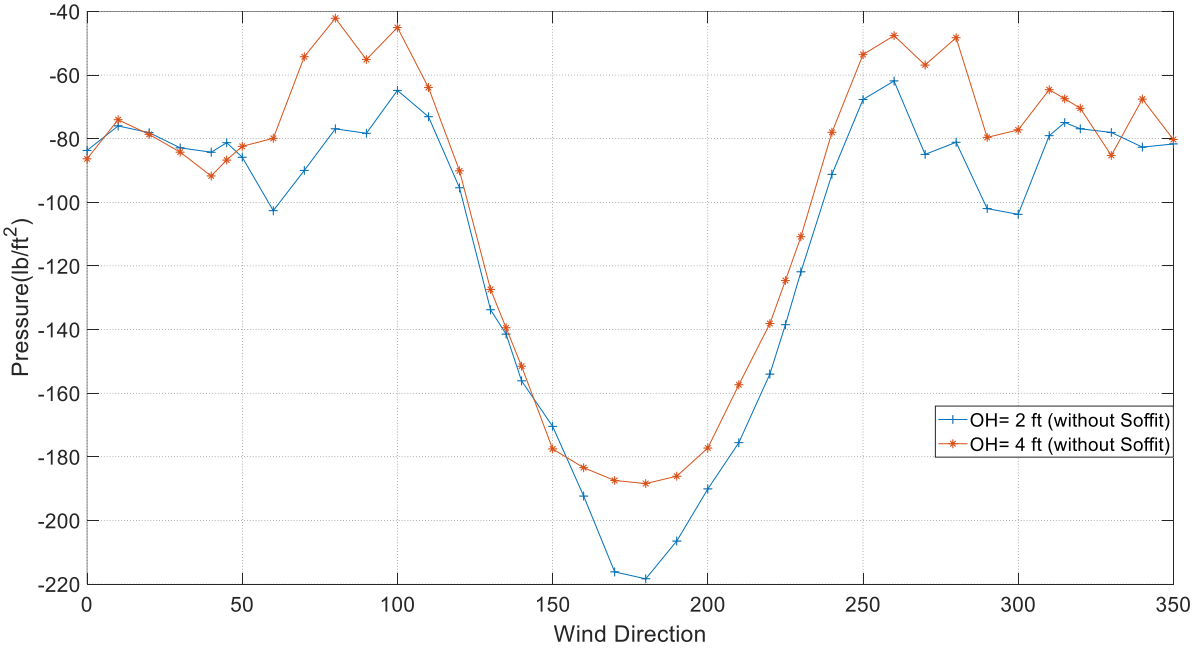

Fig.2. 33: Uplift pressure over the 2 ft and 4 ft overhang surface area along wind direction for uncovered soffits

CHAPTER III. Analytical Program

This chapter comprises of two major branches for the developed analytical study. The first branch is the empirical model which correlate the relationship between the soffit pressure coefficient and the adjacent wall pressure coefficient for both positive and negative pressures. The second branch is a codification study for roof overhangs and walls using the experimental data from the wind tunnel testing.

3.1. Empirical Model

This section discusses the developing of an empirical mode for correlating the pressure coefficients between walls and soffits. There is an assumption in ASCE 7-16 and ASCE 7-22 that state that the positive pressure coefficients on soffits may be taken exactly the same as the pressure coefficient on walls (Vickery 2008), without mentioning the maximum width of the soffit for which this assumption is valid. In addition, this assumption is only valid on positive pressure coefficient without providing any information on negative pressure coefficients.

3.2. Regression Analysis of Pressures on Soffits and Adjacent Walls

The pressure taps in walls and soffits were placed with equal spacing, to compare the C_p of upper taps on the wall with the adjacent taps on the soffit using regression analysis. For all the figures that include the wall and the soffit, the shorter side of the soffit is the wall side (lower side), and the longer side of the soffit is the edge side (upper side).

One of the objectives of this research study was to correlate the effect of wall pressure to the soffit pressure and investigate how the width of soffit would affect this correlation. Regression analysis is used to measure the relation between two variables and

one of the most common forms is the Pearson's correlation (R factor) which ranges from 0 (no correlation) to 1/-1 (perfect correlation). This factor follows Eq. (7) and was used later in Regression analysis as well.

$$R = \frac{\Sigma(x_i-\bar{x})(y_i-\bar{y})}{\sqrt{\Sigma(x_i-\bar{x})^2\Sigma(y_i-\bar{y})^2}} \quad (7)$$

Regression analysis was done on the wall upper taps and adjacent soffit taps for all the models. Regression analysis was done to get the relationship between the pressure coefficients of the soffit taps with the wall taps. This relationship either shows a decrease or increase of the pressure coefficient for each row of the soffits compared to pressure coefficients of the walls. For all the models, the corner taps for walls and soffit were not considered in correlation as shown in **Fig.3. 1** to **Fig.3. 6**, only the taps inside the dashed box included in analysis, because the separation of the flow occurs at the corner of the building, so the Cp of these taps have lower values compared to other taps and may not be significant to be accurate for regression. For models of 0.6 m overhang width, the first row is the one next to the wall and the third row is the outer edge row, similarly for the models of overhang width of 1.2 m and 1.8 m, the first row is the row adjacent to the walls and the fourth and fifth rows are the edge rows, respectively. It was found from the regression plots that the positive peak pressures were well correlated (i.e., R-squared values near to 1) for the near and far rows for all the models, while for the negative peak pressure, R-squared value significantly decrease as the taps locate far from the wall, especially for wider soffits. Moreover, it is apparent from the regression plots, that the slope for the positive peak pressure coefficient in all the models is close to 1 and this supports the assumption in ASCE 7-16 and ASCE 7-22. However, for peak negative pressure coefficients the soffit and wall

taps are not well correlated, and the slope is not close to 1 due to the divergence of peak negative pressure coefficients for the soffit and wall soffit especially for wider overhangs.

To validate the current findings, the results were compared to one of the few relevant studies that was identified in the literature (Vickery 2008). The latter study investigated the correlation between the wall and the soffits pressure on one-, two-, and three-story buildings of a hip roof of slope 4:12 and soffit width of 0.5 m. That was the same as Model A, B and C that were investigated in the present study and were compared to Vickery's study. The linear regression model matches well with Vickery's model for positive pressure coefficients for wall and edge rows for all the models of 0.6 m, 1.2 m, and 1.8 m overhang width, and for negative pressure for the first row only of the three models. Acute divergence between the two studies for negative pressure coefficients started to happen in row 3, row 4, and row 5 which are the edge rows of the 0.6 m, 1.2 m, 1.8 m overhangs width respectively. The acute divergence with Vickery's study is expected to happen since Vickery studied only one width of short overhangs of 0.5 m, while at the edge of wider overhangs (0.6 m, 1.2 m, and 1.8 m) deemed to be too different in terms of peak negative pressure coefficients. However, the peak positive pressures still match well, even by increasing overhang width. It is important to note that models with roof slope of 6:12 were not compared with Vickery's study, due to the in similarity in roof slope.

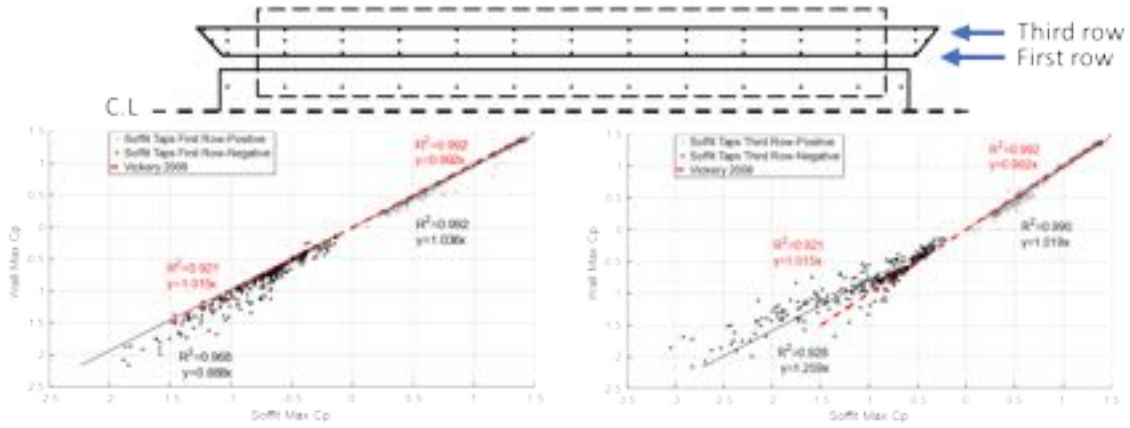

(a) (b)

Fig.3. 1: Linear Regression Relation between Upper Taps in South Wall and (a) first row of taps (b) third row of taps in soffit for roof (18.4˚) of overhang width 0.6 m.

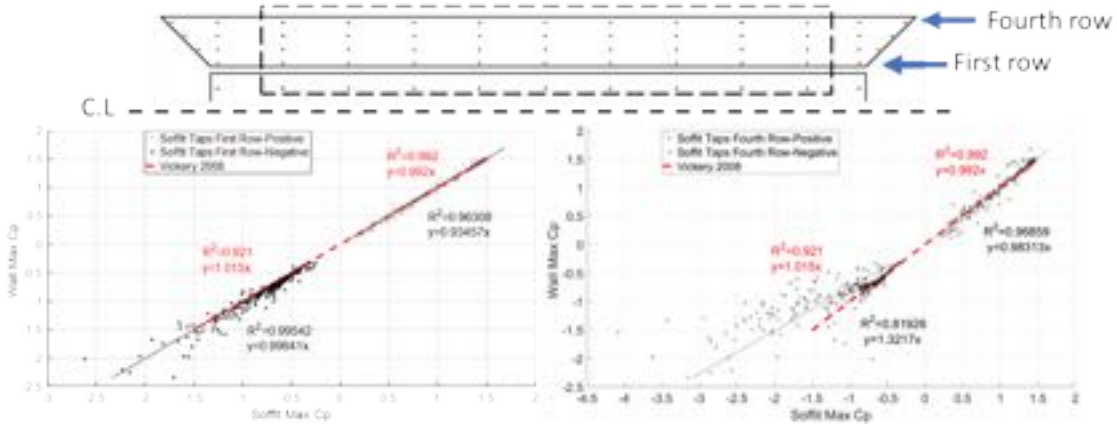

(a) (b)

Fig.3. 2: Linear Regression Relation between Upper Taps in South Wall and (a) first row of taps (b) third row of taps in soffit for roof (18.4˚) of overhang width 1.2 m.

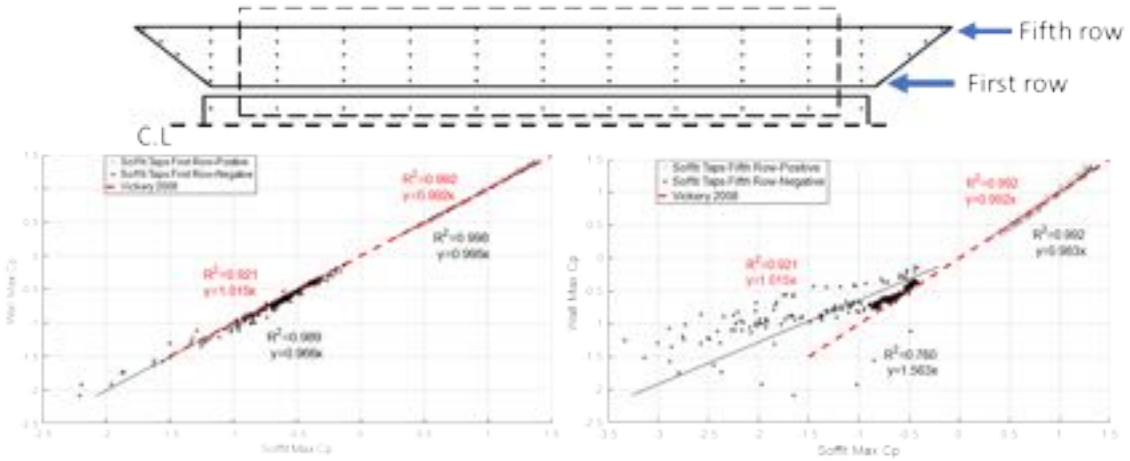

(a) (b)

Fig.3. 3: Linear Regression Relation between Upper Taps in South Wall and (a) first row of taps (b) third row of taps in soffit for roof (18.4˚) of overhang width 1.8 m.

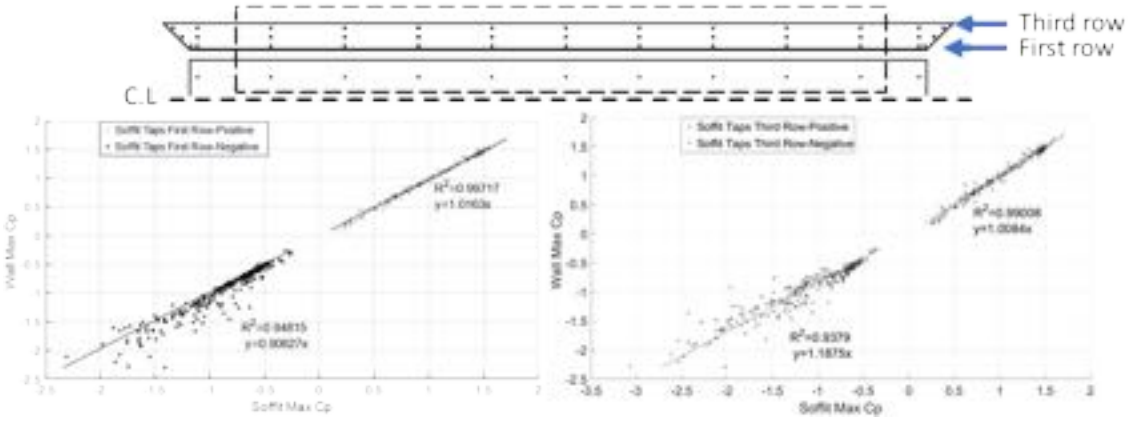

(a) (b)

Fig.3. 4: Linear Regression Relation between Upper Taps in South Wall and (a) first row of taps (b) third row of taps in soffit for roof (26.6˚) of overhang width 0.6 m.

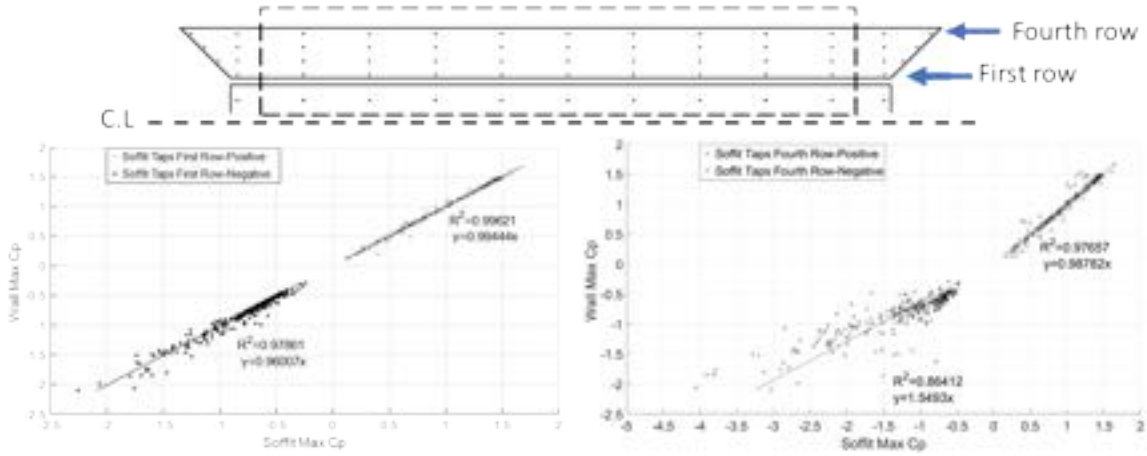

(a) (b)

Fig.3. 5: Linear Regression Relation between Upper Taps in South Wall and (a) first row of taps (b) third row of taps in soffit for roof (26.6˚) of overhang width 1.2 m.

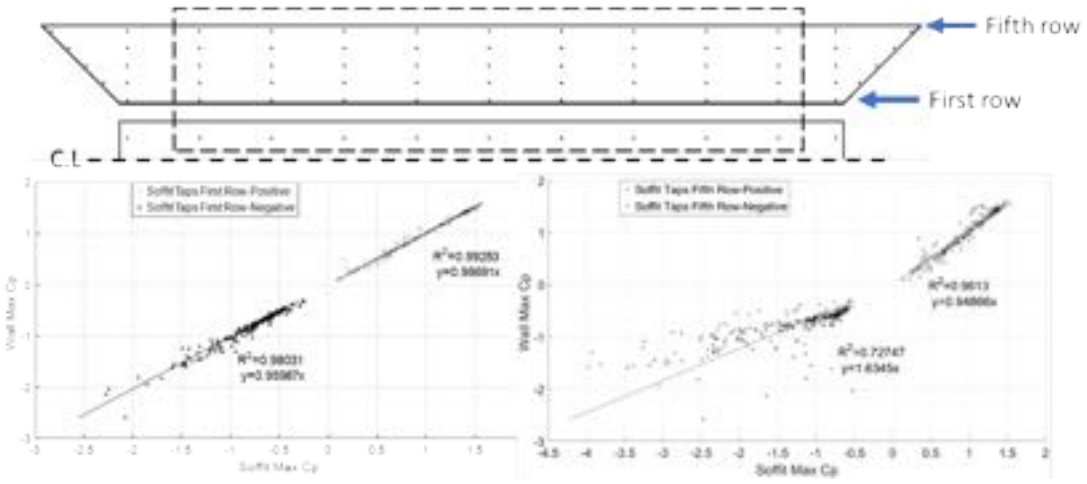

(a) (b)

Fig.3. 6: Linear Regression Relation between Upper Taps in South Wall and (a) first row of taps (b) third row of taps in soffit for roof (26.6˚) of overhang width 1.8 m.

3.3. Correlation equation for soffit and wall pressure coefficient

Based on the regression analysis plots, it was concluded that the positive pressure coefficients on the soffit may be taken exactly the same as the pressure coefficients on the wall, regardless of the overhang width and roof slope. However, this shall not be the case for negative pressure coefficient, especially for wider overhang width. Thus, using the experimental data and the performed regression analysis, an empirical model was developed to govern the relation between walls and soffits positive and negative pressure coefficients.

The model was developed using the experimental data from all the models from one side (i.e., south side) along the 40 wind directions. It is important to note that the positive pressure coefficients were investigated using 15 wind directions that dominate the positive pressure on the south wall as shown in **Fig.3. 7**, and the negative pressure coefficients were investigated using the other 25 wind directions that govern the negative pressure coefficients as shown in **Fig.3. 8**.

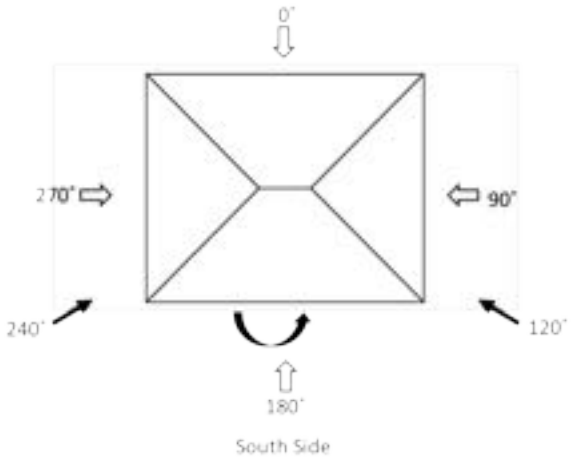

Fig.3. 7: Wind directions used for developing the empirical model for positive pressure

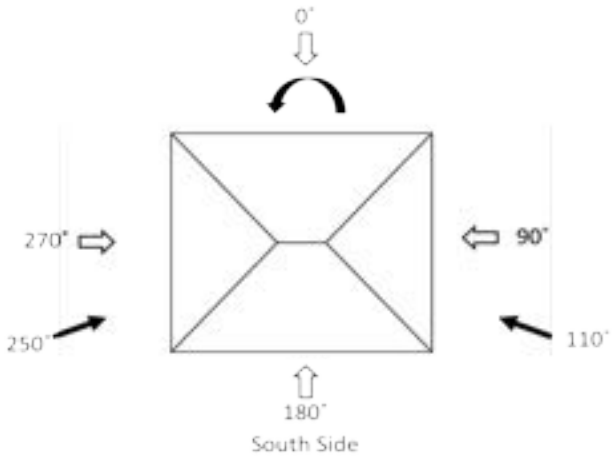

Fig.3. 8: Wind directions used for developing the empirical model for negative pressure

Different parameters have been considered while developing the empirical models for soffit pressure coefficients, such as the soffit width, roof slope and wall surface pressure coefficient. For positive pressure coefficient, the empirical equation that govern the wall and soffit pressure coefficient is exactly the same as the assumption in ASCE 7-16 and ASCE 7-22, which state that the soffit positive pressure can be taken the same as the adjacent wall pressure coefficient. Therefore, despite the overhang width, or the roof shape and slope, the positive pressure coefficient on the soffit can be calculated as Eq. (8).

$$Cp_{Soffit} = Cp_{Wall} \quad (8)$$

The empirical model for negative pressure coefficient is more challenging in terms of developing a linear relation between the soffit and the wall pressure coefficients. This is due to the turbulence occurring underneath the soffit which affects the suction among the soffit and among the walls independently for different wind directions. However, a relation has been developed for predicting the soffit pressure coefficient from the wall pressure coefficient that is a function of the overhang width. The roof slope did not seem to have a recognizable effect on changing the wall and soffit pressure coefficients, therefore, the empirical equation is not governed by roof slope. The empirical equation for negative pressure coefficients as shown in Eq. (9) can be used for preliminary estimating the critical soffit pressure coefficient by knowing the corresponding wall pressure coefficient, and the soffit width. **Table 3. 1** shows the measure and predicted peak min Cp using the developed empirical equation. It is worth mentioning to note that the positive pressure on the soffit is more critical regarding the net pressure coefficient on the overhangs because the positive pressure on the soffit is added to the negative suction on the upper surface of the overhang which cause higher peak net pressure coefficient.

$$Cp_{Soffit} = 3.50 * Cp_{Wall} - 0.68 * W + 5 \quad (9)$$

Where, W is the overhang width in meters.

Table 3. 1: Measured peak min Cp vs calculated empirical peak min Cp

	Measured Peak Min Cp-Wall	Measured Peak Min Cp-Soffit	Empirical Peak Min Cp-Soffit
Roof (18.4˚) – 0.6 m OH	-2.156	-3.045	-2.95
Roof (18.4˚) – 1.2 m OH	-2.33	-4.08	-3.97
Roof (18.4˚) – 1.8 m OH	-2.18	-3.62	-3.85
Roof (26.6˚) – 0.2 m OH	-2.3	-3.06	-3.46
Roof (26.6˚ – 1.2 m OH	-2.4	-4.05	-4.22
Roof (26.6˚ – 1.8 m OH	-2.25	-3.9	-4.10

3.4. Area Averaged pressure coefficients

In total, 40 wind directions were tested to determine the maximum and minimum peak C_p for each pressure tap beside investigating the pressure gradients on groups of taps on the overhangs and walls and compare it to different versions of ASCE 7 for codification purposes using the area-averaged C_p values with the corresponding effective area. The area averaged peak Cp values were calculated for both roof overhangs/soffit and for adjacent walls. The wall positive Cps in ASCE 7-16 and ASCE 7-22 are assumed to be equal to soffit Cps. Thus, it was important to discuss and include the walls pressure coefficient in this study. The area-averaged peak C_p values were computed for each wind direction by considering single or multiple sets of pressure taps and assigning them to their corresponding tributary area. The pressure taps were placed in an orthogonal pattern, thus the tributary area for each tap was approximated by rectangular areas (Simiu and Scanlan 1996). The area averaged peak Cp values were calculated for both roof overhangs/soffit and for adjacent walls. The wall positive Cps in ASCE 7-16 and ASCE 7-22 are assumed to be equal to soffit Cps. Thus, it was important to discuss and include the walls pressure coefficient in this study.

3.4.1. Area Averaged pressure coefficients for hip roofs overhangs

This section discusses the area-averaged pressure coefficient findings and attempts a comparison of the experimental results to the GC_p design guidelines of the latest three versions of ASCE 7 which provides a comprehensive review for the latest changes between the three versions in terms of different Cp's and roof zoning areas. Area averaged pressure taps were considered according to the specified zones for hip roof of slope 4:12 and 6:12 in plots assigned to roof angle of 7˚ to 20˚, and 20˚ to 27˚, respectively in ASCE 7-16 and ASCE 7-22. GC_p are calculated first in which the tributary area A_i for each tap i inside the desired averaged area at any wind direction θ is multiplied by its wind pressure coefficient time history $Cp_i(\theta, t)$, then the sum is divided by the summation of all the tributary area for the selected taps of interest following Eq. (10) (Simiu and Scanlan 1996), then using PTS to calculate the peak 3 sec as complied with Eq. (6).

$$GCp_{av}(\theta, t) = \frac{\sum_i Cp_i(\theta,t)\, A_i}{\sum_i A_i} \quad (10)$$

3.4.1.1. Comparisons with ASCE 7-10 & ASCE 7-16

The experimental results for overhang's peak net pressure coefficient in terms of effective area were plotted and compared to the latest three versions if ASCE 7 GC_p plots. Zone 2 in ASCE 7-10 was defined later in ASCE 7-16 as zones 2e and 2r Fig. 1. The net pressure coefficient was calculated as the algebraic sum of the overhang's top surface and the overhang's bottom surface (soffit). In ASCE 7-16, there are two GC_p plots for hip roof of angle 7˚ to 20˚ with overhangs, one for $h/B \geq 0.8$ and the other for $h/B \leq 0.5$, where h is the roof mean height and B is the horizontal dimension of the building normal to wind direction. There are no separate plots for different h/B for the hip roof of angle 26.6 ˚ (i.e., between 20˚ and 27˚).

As expected, both plots show the expected monotonically decreasing relationship between the effective area and the magnitude of the net pressure coefficients. For models of roof slope 4:12 (i.e., roof angle of 18.4˚), and according to the dimension of all the models 15.2 m by 12.2 m and roof mean height of 8.76, the h/B for south side (longer side) is 0.57 and for east side (shorter side) is 0.71. It is important to note that h/B criteria are only assigned for GC_p plots of roof angle of 7˚ to 20˚ and in ASCE 7-16 only. Most of the peak net GC_p values for both south and east sides were above the upper bound of the plot (-2.9) and (-2.5) respectively, for ASCE 7-16, and above the upper boundary of (-2.2) for ASCE 7-10, **Fig.3. 9** and **Fig.3. 10**, while for zone 3 only local point exceeded the upper bound of ASCE 7-16 (-3.1 and -3.5) for h/B of 0.57 and 0.71, respectively and ASCE 7-10 (-3.7) as shown in **Fig.3. 11**. For models of roof slope 6:12 (i.e., roof angle of 26.6˚), there are no specific plots for different h/B for roof angle between 20˚ to 27˚, thus all the plots comprise the peak net GC_p values for both south and east sides together **Fig.3. 12**. For zone 2e, many local and area averaged pressure taps were above the upper bound for ASCE 7-16 (-2.5) and ASCE 7-10 (-2.2). It is important to note that the smallest effective wind area is based on local pressure for one tap. For zone 3, most of the GC_p values for all the models were entirely below the upper bound for ASCE 7-16 (-3.1) and ASCE 7-10 (-3.7) with some local points of one tap exceeding the upper bound for only model of 0.6 m overhang. Therefore, based on the distributions of net pressure coefficients with ASCE 7 GC_p plots, this may suggest that ASCE 7-16 is less conservative compared to the experimental testing regarding zone 2e for any overhang width, while regarding zone 3 it is less conservative compared to experimental testing only for short overhang width (i.e., 0.6 m).

Roof angle 18.4˚- Overhang width 0.6 m (Zone 2e)

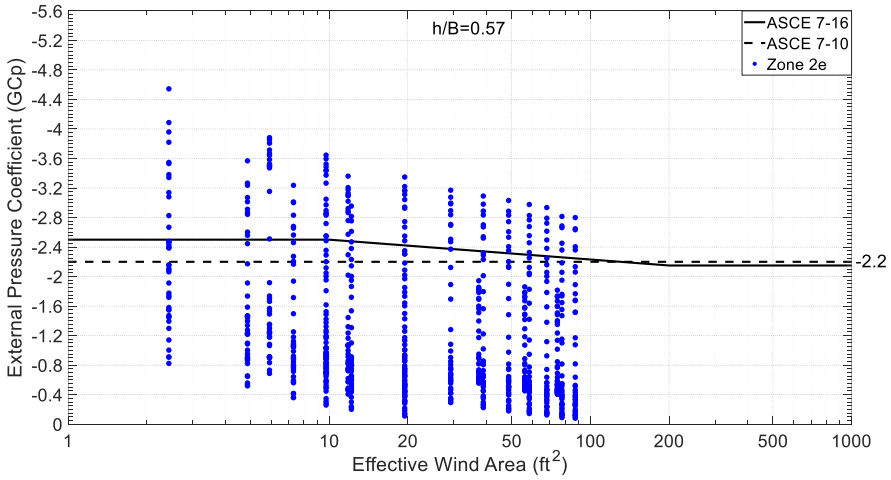

Roof angle 18.4˚- Overhang width 1.2 m (Zone 2e)

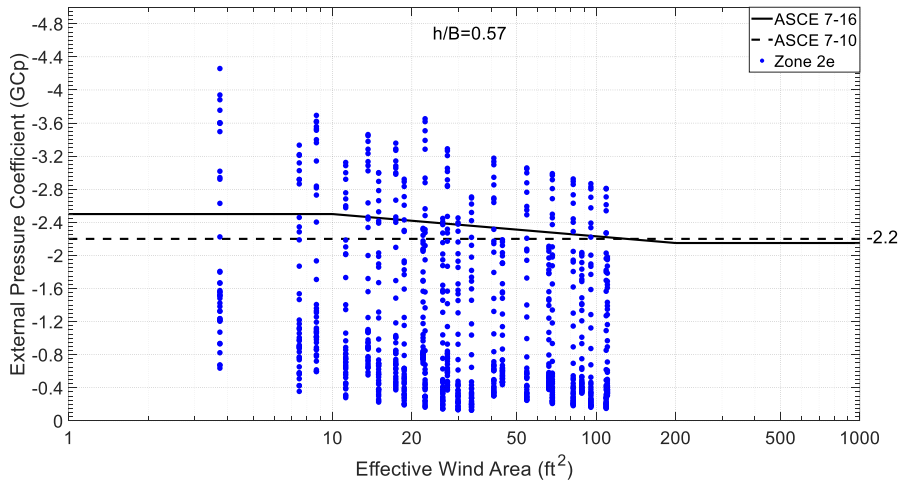

Roof angle 18.4˚- Overhang width 1.8 m (Zone 2e)

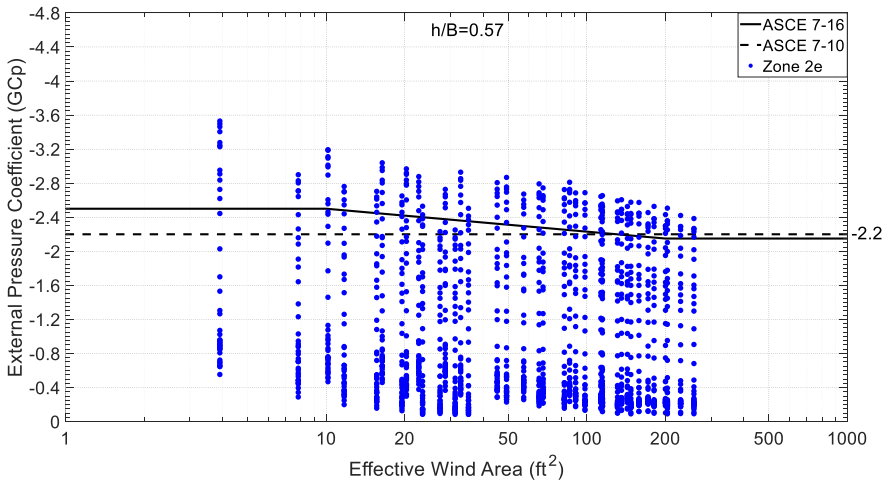

Fig.3. 9: Critical area-averaged net pressure coefficient for zone 2e for south side compared to GC_p plot in ASCE 7-16 and ASCE 7-10 for the 18.4˚ deg roof

Roof angle 18.4˚- Overhang width 0.6 m (Zone 2e)

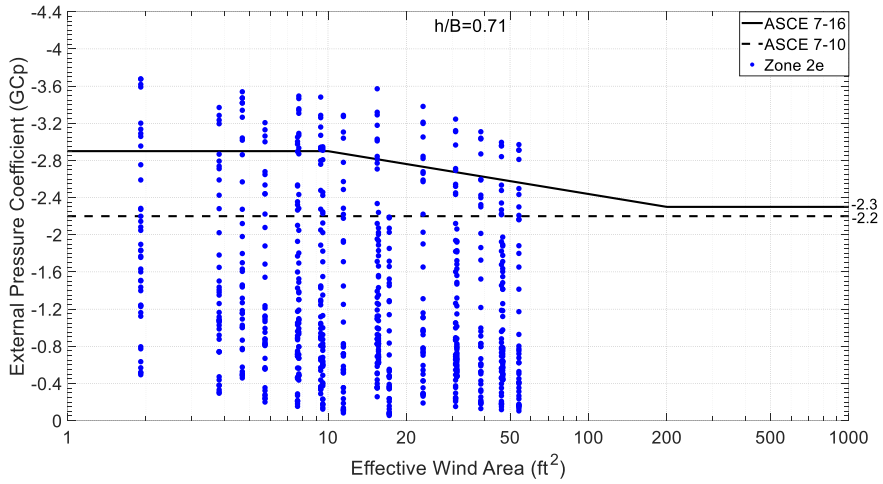

Roof angle 18.4˚- Overhang width 1.2 m (Zone 2e)

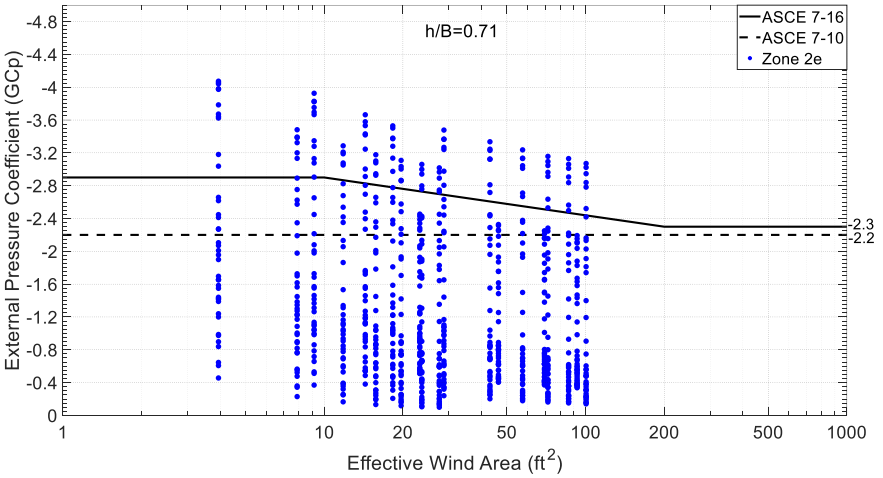

Roof angle 18.4˚- Overhang width 1.8 m (Zone 2e)

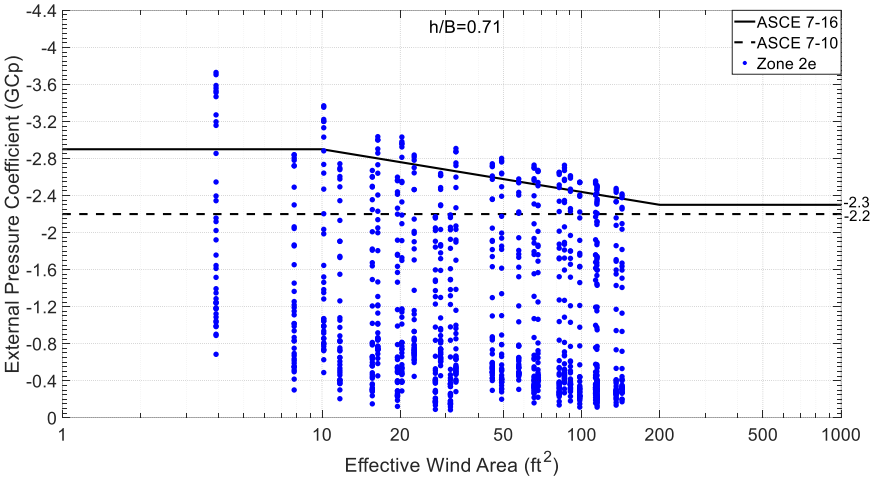

Fig.3. 10: Critical area-averaged net pressure coefficient for zone 2e for east side compared to GC_p plot in ASCE 7-16 and ASCE 7-10 for the 18.4˚ deg roof

Roof angle 18.4˚- Overhang width 0.6 m - 1.2m -1.8m (Zone 3)

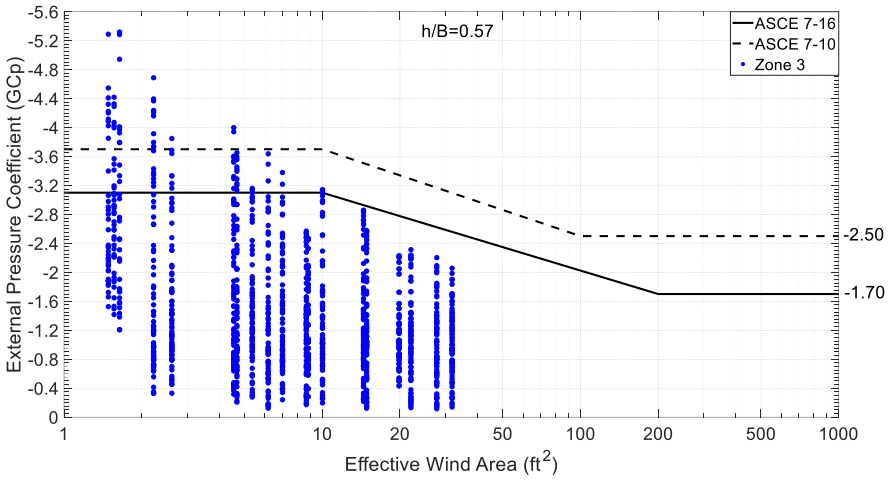

Roof angle 18.4˚- Overhang width 0.6 m - 1.2m -1.8m (Zone 3)

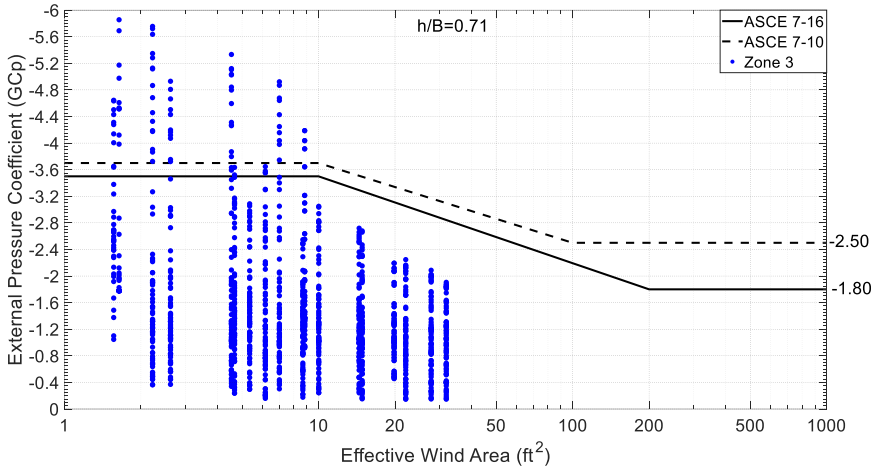

Fig.3. 11: Critical area-averaged net pressure coefficient for zone 3 for south and east side compared to GC_p plot in ASCE 7-16 and ASCE 7-10 for the 18.4˚ deg roof

Roof angle 26.6˚- Overhang width 0.6 m - 1.2m -1.8m (Zone 2e)

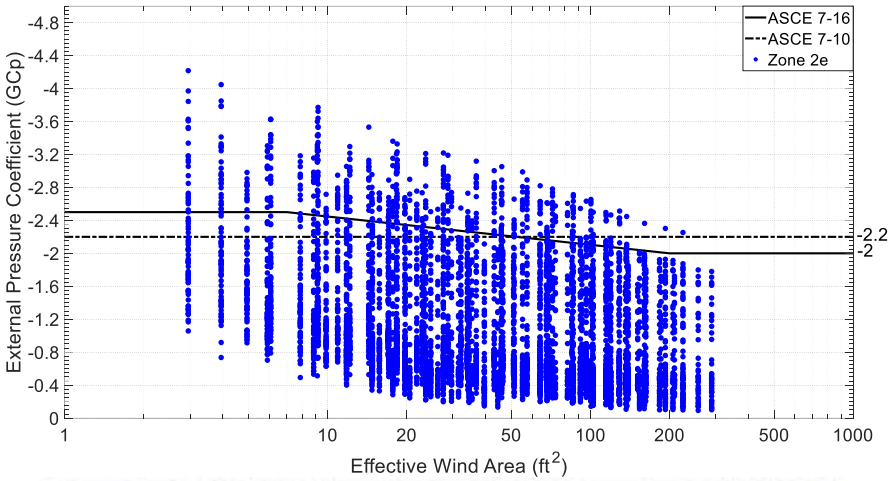

Roof angle 26.6˚ - Overhang width 0.6 m - 1.2m -1.8m (Zone 3)

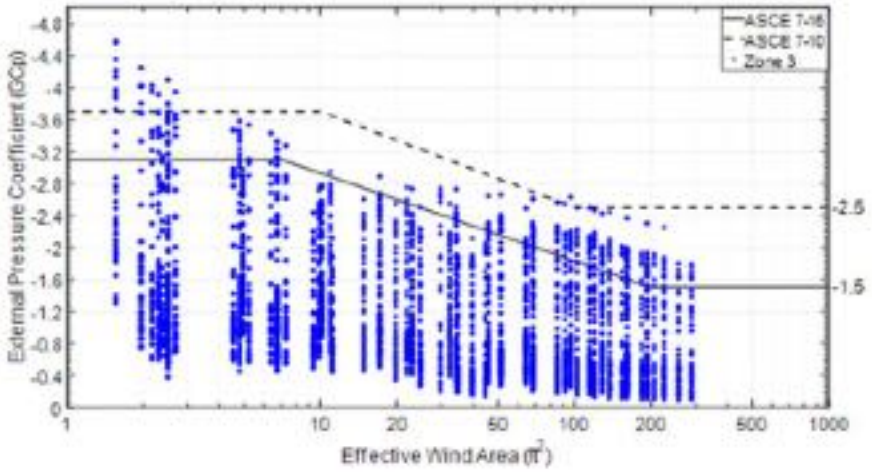

Fig.3. 12: Critical area-averaged net pressure coefficient for zone 2e and zone 3 for south and east side compared to GC_p plot in ASCE 7-16 and ASCE 7-10 for the 26.6˚ deg roof

3.4.2. Comparison with ASCE 7-22

In addition to the comparison made with ASCE 7-10 & ASCE 7-16, the experimental results for overhang's peak net pressure coefficient were plotted and compared to ASCE 7-22 GC_p plots. The zoning criterion is different between ASCE 7-22 and ASCE 7-10/7-16, both the edge and the corner are specified as zone 3 instead of zone 2/2e. The upper bound for ASCE 7-22 is calculated as the sum of negative upper bound for the GC_p plot for the applicable roof surface and the positive upper bound for GC_p plot for the wall surface with x grid of [1 10 100 500 1000]. The x grids for GC_p plots of walls in

ASCE 7-22 is [1 10 500 1000], while for hip roofs of angle 7˚ to 20˚ is [1 10 200 1000], and roof angle 20˚ to 27˚ is [1 10 100 1000], thus in **Fig.3. 13** and **Fig.3. 14**, the ASCE 7-22 boundaries were drawn to account for all the x grid between both GC_p plots for walls and roofs. As mentioned earlier, the positive pressure for the wall and soffit (towards the surface) is in the same direction as the negative pressure for the roof overhangs (away from the surface).

All the plots **Fig.3. 13** and **Fig.3. 14** show the expected monotonically decreasing relationship between the effective area and the magnitude of the net pressure coefficients. For the 18.4˚ deg roof, magnitudes of most of the tap combinations were below the upper bound (-3.6), except for some local taps and areas specifically for 0.6 m overhang. For 26.6˚ deg roof most of the peak net GC_p values were below the upper bound of the plot (-3.4) with some points exceeding the upper bound for smaller tributary areas or single local tap for 0.6 m overhang. This may suggest that ASCE 7-22 is more conservative compared to the other two older versions, but still a bit less conservative compared to the experimental testing regarding zone 3 for short overhang width only (i.e., 0.6 m). though some revisions appear to still be necessary.

Roof angle 18.4˚- Overhang width 0.6 m

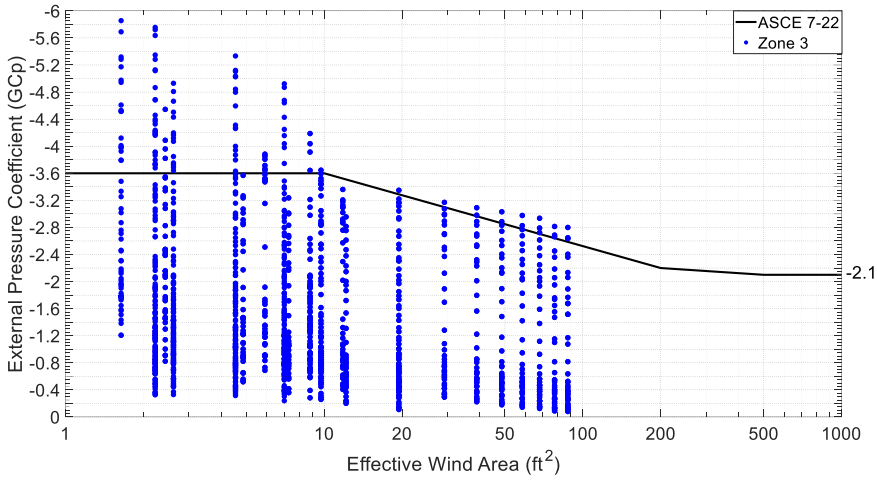

Roof angle 18.4˚ - Overhang width 1.2 m

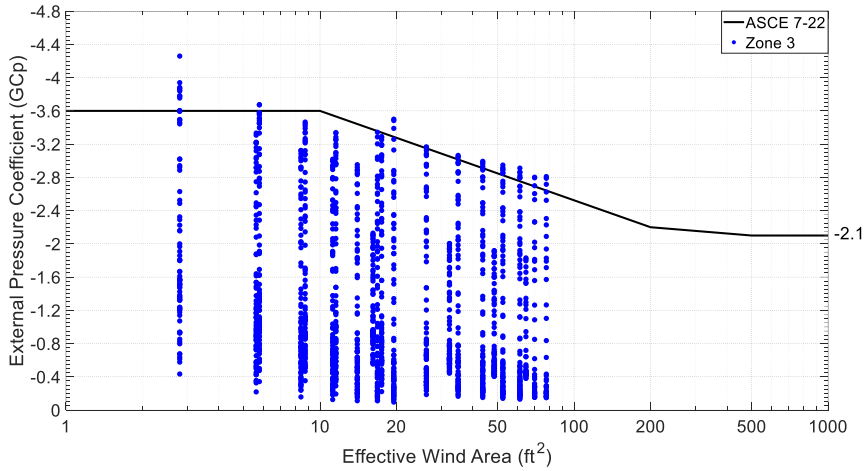

Roof angle 18.4˚- Overhang width 1.8 m

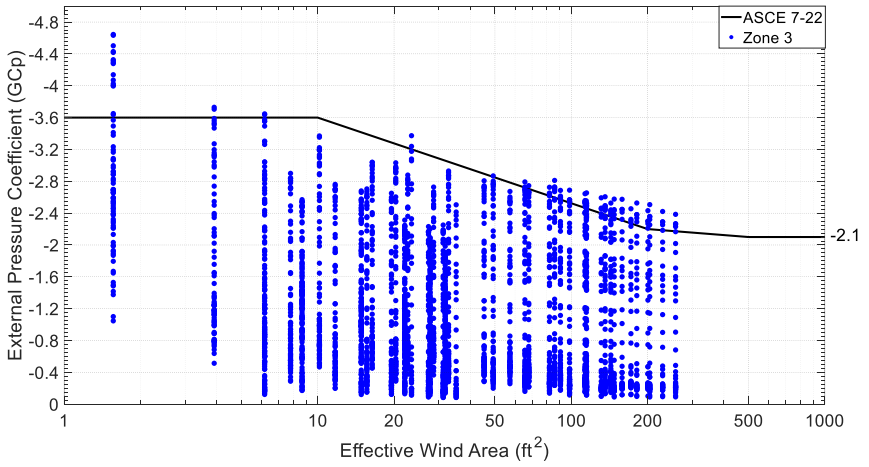

Fig.3. 13: Critical area-averaged net pressure coefficient for zone 3 compared to GC_p plot in ASCE 7-22 for the 18.4˚ deg roof

Roof angle 26.6˚- Overhang width 0.6 m

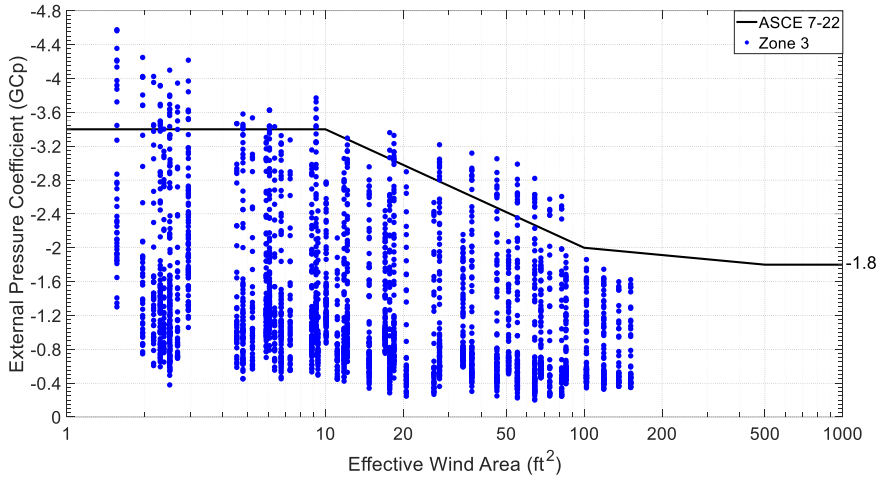

Roof angle 26.6˚ - Overhang width 1.2 m

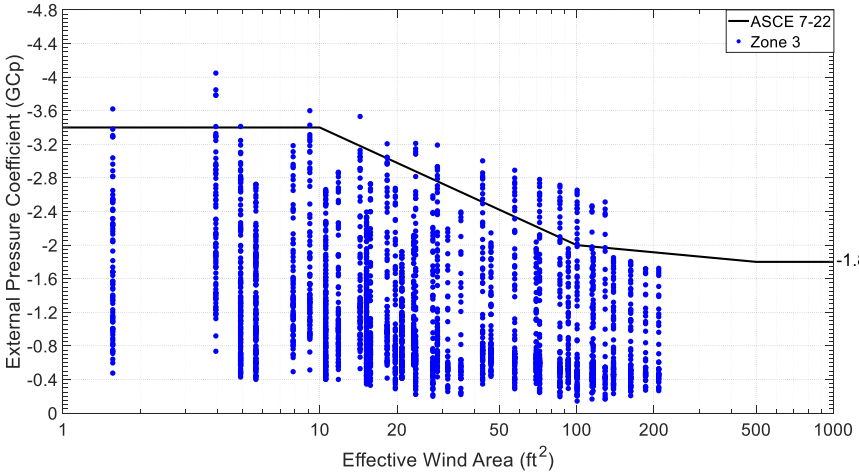

Roof angle 26.6˚- Overhang width 1.8 m

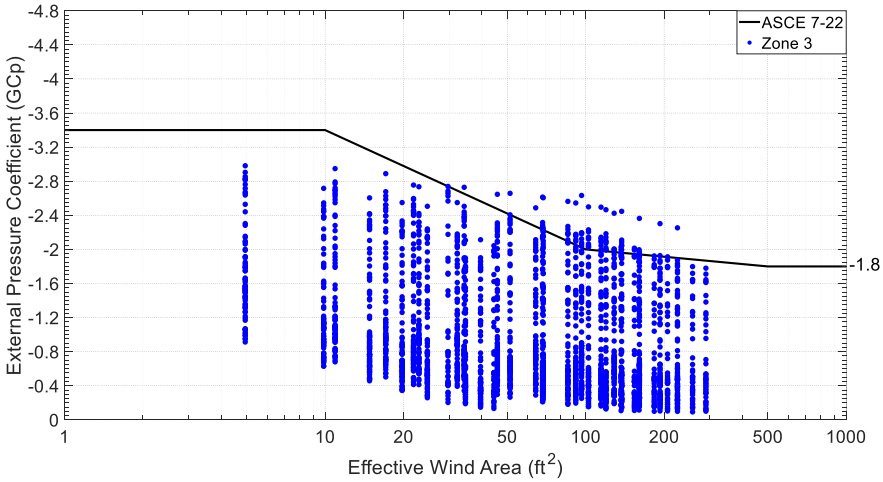

Fig.3. 14: Critical area-averaged net pressure coefficient for zone 3 compared to GC_p plot in ASCE 7-22 the 26.6˚ deg roof

3.5. Area Averaged pressure coefficients for walls

In addition to the area-averaged analysis of hip roofs of both angles, area-averaged pressure analysis for walls was done to investigate further the pressure gradients on single or groups of taps among the walls. The same procedures, as overhangs, were followed for the analysis of the external pressure coefficient at the walls. The area of the wall is divided into zone 4 and zone 5 as specified in ASCE 7 (7-10, 7-16, and 7-22), where zone 5 is the edge zone of width 'a' and zone 4 is the remaining area of the wall, as shown in Fig. 2. Constant 'a' was defined before in section 2.

There is not a significant difference among the peak min and peak max pressure coefficients on the adjacent wall of different roof overhang widths for the same roof slope. However, there is some variation between the peak pressure coefficients among the wall surface for different roof angles (i.e., 18.4˚, 26.6˚). **Fig.3. 15** shows the critical area-averaged external pressure coefficient for zone 4 and 5 for adjacent walls of all overhang widths for both roofs. Most of the GC_p values were located between the upper boundary (peak min) and lower boundary (peak max) of GC_p plots as specified in ASCE 7-22. However, GC_p values of some local taps or combination of small areas have exceeded these boundaries. For instance, the GC_p values among zone 5 reach peak min of -3.0 and -2.5 for roof angles of 18.4˚ and 26.6˚, respectively, and reach peak max of 1.9 for both slopes. For zone 4, the GC_p values reach a peak min of -2.3 and peak max of 1.4 for both slopes. Therefore, this may suggest that the code provision is less conservative compared to the experimental results regarding both zones 4 and 5. It is important to note that the slope of the roof has no effect on the wall positive pressure coefficients when the walls are located in the windward direction but have more considerable effect for other

wind directions such as leeward direction or generally where suction occurs. As can be seen in **Fig.3. 15**, the peak max pressure coefficients among the walls for both roof slopes are almost the same (2.0), while the peak min pressure coefficient for adjacent walls is -3.0 and -2.5 for roof slope of 18.4˚ and 26.6˚, respectively. From a design perspective, the wall is being designed for both peak max and peak min pressure coefficients, however, the peak min pressure coefficient is more critical and always govern the design procedures for the walls.

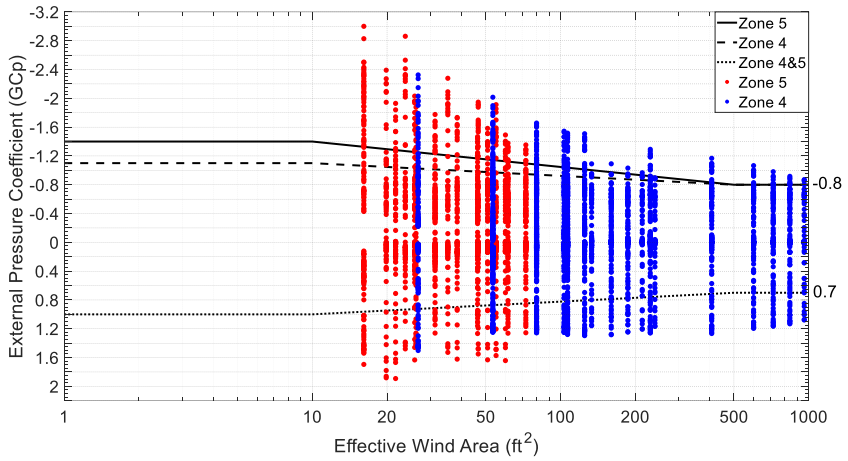

(a)

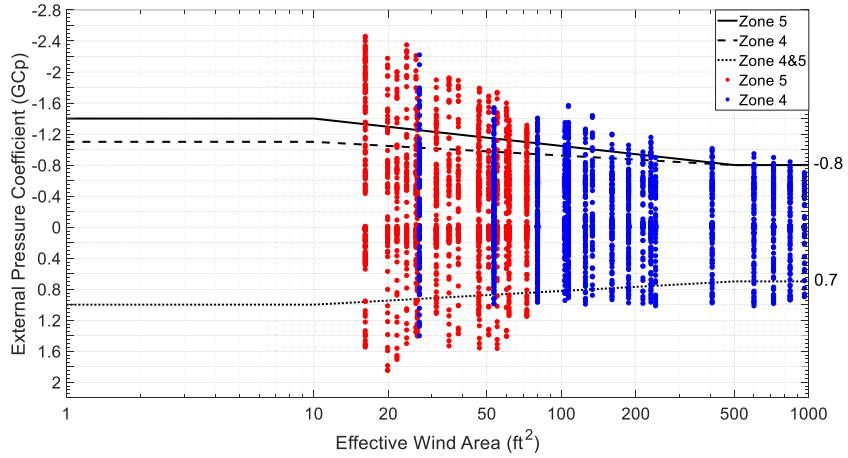

(b)

Fig.3. 15: Critical area-averaged external pressure coefficient for zone 4 and 5 for walls compared to GC_p plot in ASCE 7-22 for (a) roof angle 18.4˚ (b) roof angle 26.6˚

3.6. Codification Study

This section presents two approaches for the codification study to enhance the design guidelines for future code of practices. The first approach is an envelope approach which confines all the experimental data underneath the boundaries based on the critical net pressure coefficient for overhangs and for external pressure coefficients for walls. The second approach is a statistical approach similar to the reduction factor of 0.8 by Davenport approach (Stathopoulos 2003) that reduces the critical envelope boundaries due to the uncertainty to expect the most critical wind speed to be originated from the most critical wind direction, and due to some uncertainties in wind tunnel testing.

3.7. Envelope curves for area-averaged net pressure coefficients

The area-averaged pressure analysis for the experimental data with GC_p plots, compared with the last three versions of ASCE 7 (7-10, 7-16, and 7-22), for both roof overhangs and adjacent walls was shown in the previous section. Based on this parametric study, it is apparent that none of the upper boundaries for the GC_p plots of the latest three versions of ASCE 7 was entirely adequate when compared to the experimental results in terms of design guidelines. Thus, a proposed design provisions for GC_p plots for roof with overhangs, and for walls as well, may enhance the design guidelines for future versions of code of practices.

The three different versions of ASCE 7 in terms of roof overhangs design guidelines are studied towards codification purposes. There are some major differences related to the design of roof overhangs between the recently released version of ASCE 7-22 and the previous two versions (ASCE 7-10 and ASCE 7-16) in terms of zoning criteria for the roof surface, and the GC_p plots with effective wind area. As mentioned earlier, zones 2 and 2e

in ASCE 7-10 and ASCE 7-16 respectively, were assigned with the corners under zone 3 in ASCE 7-22. In addition, the two versions of ASCE 7-10 and 7-16 have separate plots for GC_p with effective wind area for roofs with overhangs, while in ASCE 7-22 there are no separate plots for overhangs. Though, in ASCE 7-22 the net pressure coefficient for roof overhangs is calculated as the sum of the GC_p of the overhang's top and bottom surfaces, where the GC_p of the top surface is the same as the applicable roof surface, while the GC_p of the overhang's bottom surface is the same as the adjacent wall surface, and there are no specified GC_p plots according to different h/B in ASCE 7-22, as included in ASCE 7-16. Furthermore, ASCE 7-10 has assigned roof angle from 7˚ to 27˚ for both gable/hip roofs under the same category, which has been changed later in ASCE 7-16/7-22 to have different plots for gable roofs and hip roofs separately and to have separate plots for slope 7˚ to 20˚ and for slope 20˚ to 27˚.

In the current design exercise, envelope lines were superimposed onto each plot of each case to confine underneath all the GC_p value. All the envelope lines of the same category, which are either of the same roof slope or the same assigned zone on roof surface or wall surface, were combined in one plot as shown in **Fig.3. 16** and **Fig.3. 17**. The same for walls, the envelope lines were plotted according to the peak GC_p values for each case as shown in **Fig.3. 18**. However, the GC_p plot for wall as specified in ASCE 7 is not affected by roof shape or slope or overhang width.

Consequently, the peak min envelope line for each plot was defined as the proposed boundary which is similar to the approach in a previous codification work (Davenport et al. 1985). Following this approach will assure that all the GC_p values from the experimental

results will not exceed the proposed boundary. The peak min GC_p value for the proposed boundary for roof angle 18.4˚ is -4.6 and -6 for zone 2 and zone 3, respectively, and for roof angle 26.6˚ is -4.3 and -4.6 for zone 2 and zone 3, respectively, as shown in **Fig.3. 16** and **Fig.3. 17**. Therefore, it is suggested not to assign both the edge and the corner of the roofs into a single zone (i.e. zone 3) as specified in ASCE 7-22. Furthermore, there are not significant changes between the envelope lines based on h/B, as specified in ASCE 7-16. Therefore, it is suggested to follow the approach of ASCE 7-22 and ASCE 7-10 for eliminating h/B criteria that were specified only in ASCE 7-16. In addition, it is important to keep the assigned categories for roof slopes as specified in ASCE 7-16 and ASCE 7-22 (i.e., 7˚ to 20˚ and 20˚ to 27˚). No changes are suggested to be applied on the GC_p peak max boundary for roof overhangs, from ASCE 7-22. It is important to note that GC_p plots for roof overhangs in ASCE 7-10 and ASCE 7-16 do not include the peak max boundary. For walls, the peak min GC_p value for the envelope lines are -2.6 and -3.2 for zone 4 and zone 5, respectively, while the peak max GC_p value for both zones is 1.8. It is suggested not to change the defined zoning criteria for walls, but it is recommended to revise the GC_p plot with the new proposed boundaries for both max and min GC_p.

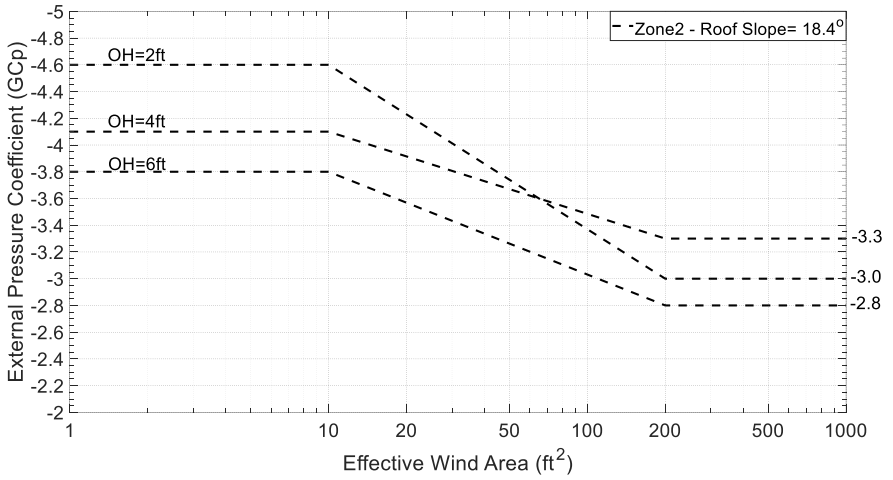

(a)

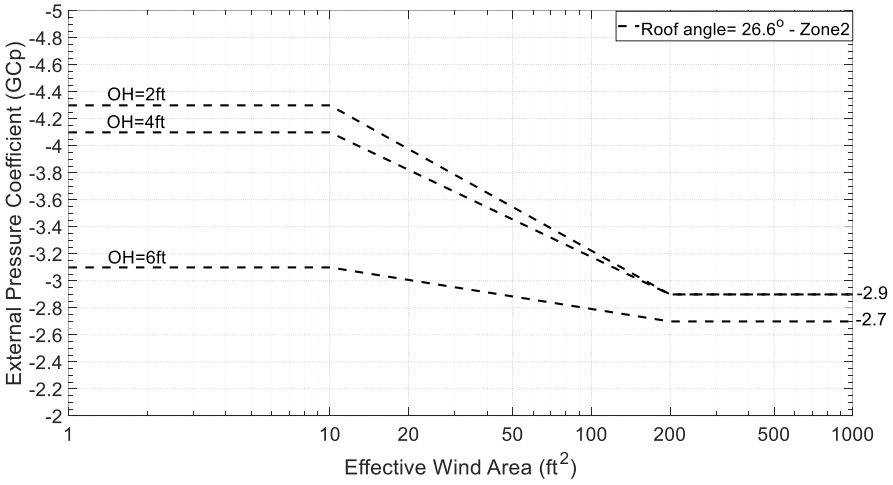

(b)

Fig.3. 16: Area averaging envelope for corresponding ranges for all testing cases for zone 2 (a) 18.4˚ deg roof (b) 26.6˚ deg roof

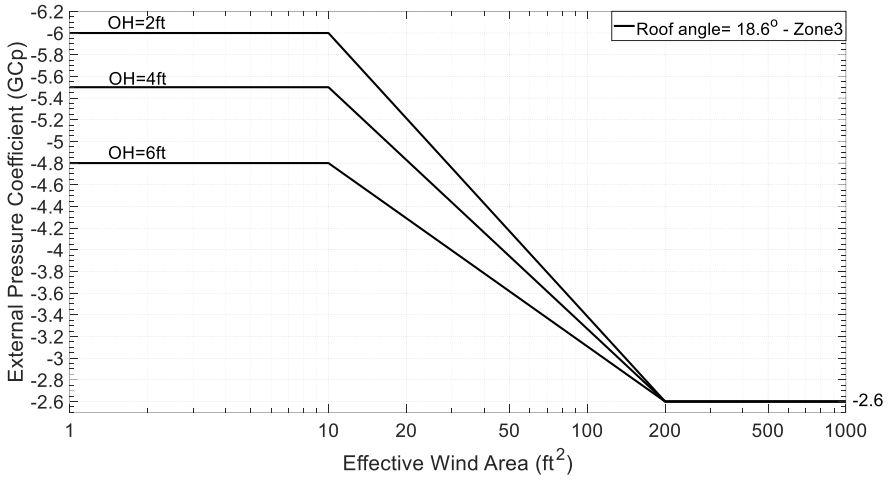

(a)

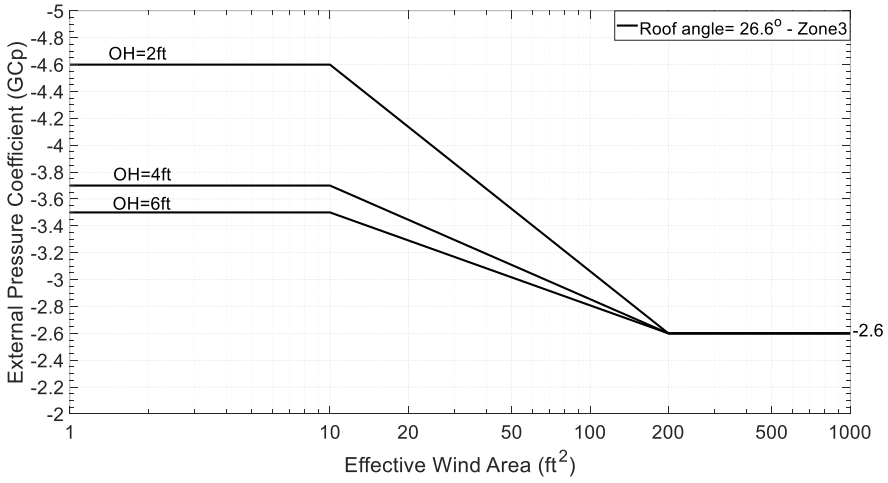

(b)

Fig.3. 17: Area averaging envelope for corresponding ranges for all testing cases for zone 3 (a) the 18.4˚ deg roof (b) the 26.6˚ deg roof

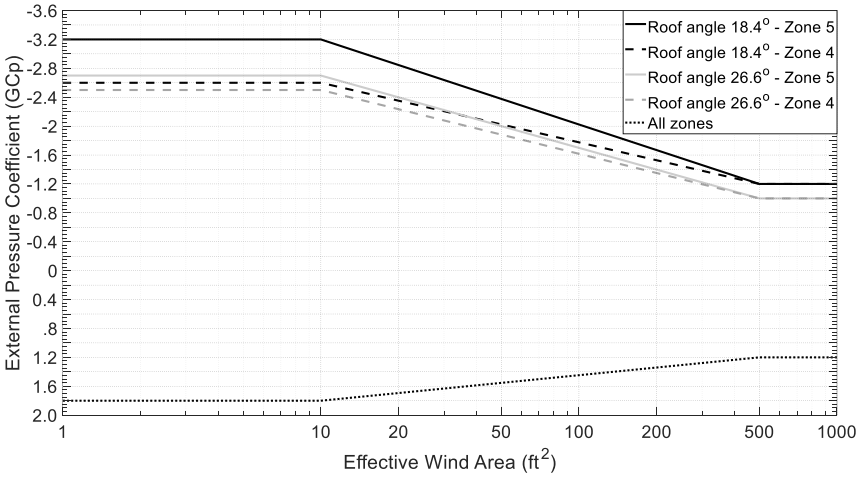

Fig.3. 18: Area averaging envelope for corresponding ranges for all testing cases for walls

3.8. Statistical distribution for area-averaged net pressure coefficients

The plots in the current wind codes and standards, such as ASCE 7, are usually based on the envelope approach discussed in the previous section while multiplied by a reduction factor. The most common reduction factor that is being used was proposed by Davenport and is equal to 0.8 (Stathopoulos 2003). This reduction factor is due to the model uncertainty from two aspects; first, the uncertainty associated with wind tunnel testing in representing the full-scale phenomena, and second the uncertainty in wind climate representation (Davenport et al. 1985). In addition, it would be unlikely for a certain building orientation to expect the most critical wind speed to be originated from the most critical wind direction. Other extensive studies (Davenport et al. 1985; Ho 1992) justified the original approach proposed by Davenport in validating its reliability. The current study proposes a statistical distribution approach which was carried out for all the testing results for both roofs in all zoning areas. The proposed approach was then compared with Davenport approach in terms of codified wind pressure coefficient. The statistical approach investigated the probability density function (PDF) for all the area-averaged net pressure

using kernel fit distribution. In addition, the histogram fit for area-averaged net pressure coefficient for 18.4˚ deg roof and 26.4˚ deg roof, are plotted to investigate the range of GC_p with the highest frequency as shown in **Fig.3. 19** and **Fig.3. 20**, respectively. It is apparent that most of the net pressure coefficients for 18.4˚ deg roof are located within range of -0.2 to -3.5 for zone 2 and -0.2 to -4.5 for zone 3, while for 26.6˚ deg roof most of the points are located within a pressure coefficient range of -0.2 to -3 for zone 2 and -0.2 to -3.5 for zone 3. Few local points have GC_p that exceeded the previous mentioned ranges. The design value from ASCE 7-10/7-16 were placed on the histogram plots to show the distribution of the critical pressure coefficient to the code provision guidelines. While the design values for ASCE 7-22 (i.e., -3.6 for 18.4˚ deg roof and -3.4 for 26.4˚ deg roof, both for zone 3) were not shown on the plot since the zoning criteria are different with previous versions. It is apparent that the provision guidelines are less conservative compared to lower frequency area-averaged points on the edges and corners of the overhangs that exposed to higher net Cp with low frequency.

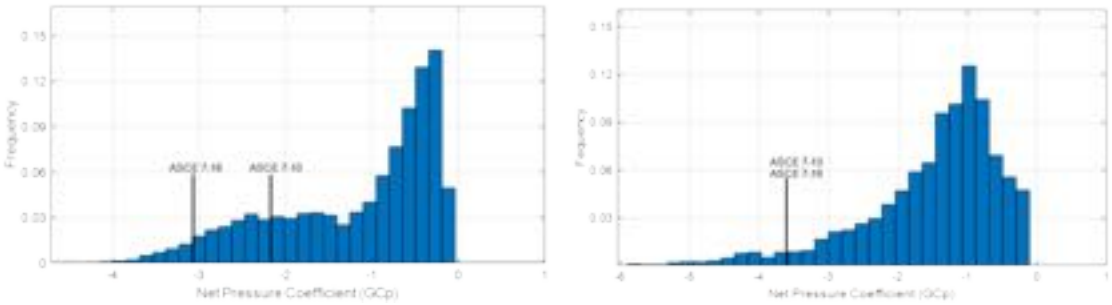

(a) (b)

Fig.3. 19: Histogram for area-averaged points with distribution fit for roof angle of 18.4˚ (a) zone 2 (b) zone 3

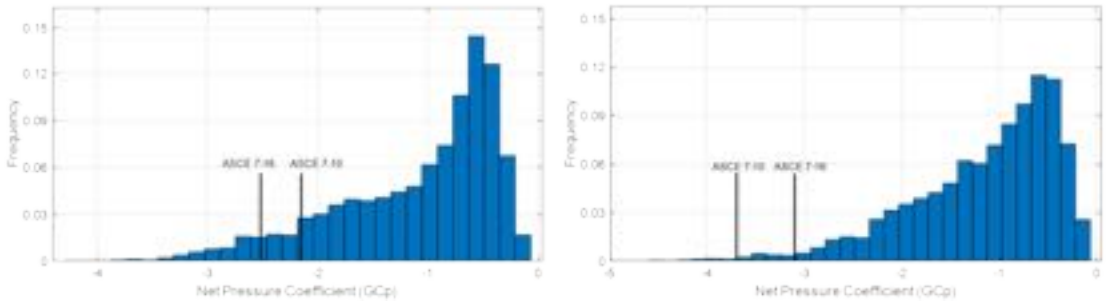

(a) (b)

Fig.3. 20: Histogram for area-averaged points with distribution fit for roof angle of 26.6˚ (a) zone 2 (b) zone 3

The area-averaged net pressure coefficients were plotted in terms of probability density function (PDF) using kernel distribution fit to estimate the density distribution for net pressure coefficients of both roofs for the two-zoning area. Kernel density is a fundamental data smoothing procedure defined as the sum of a kernel function on each data point. **Fig.3. 21** and **Fig.3. 22** show the kernel fit distribution for zone 2 and zone 3, respectively for both roofs. Both plots show a negative skew due to the longer tail on the left side of the distribution. The negative tail is due to the small probability density value for higher net pressure coefficient. In addition, high positive kurtosis values are expected with the negative skewness due to the sudden increase in the probability density function with lower net pressure coefficients. It is important to note that the higher the absolute value of the skewness, the higher the kurtosis value for each kernel fit.

The kernel fit distribution is important in assessing the probability where some values could be exceeded. For instance, it was observed from **Fig.3. 21** and **Fig.3. 22** that a PDF range of 0.01 to 0.02 is a considerable value to eliminate the negligible probability of exceedance for the corresponding net pressure coefficient. Therefore, a PDF value of 0.015 is a reasonable probability for codified wind pressure coefficients which eliminate

higher net pressure coefficient. By applying the PDF value of 0.015 on the kernel fit plots, the codified values for zone 2 is -3.8 and -3.5 for 18.4˚ deg roof and 26.4˚ deg roof, respectively. Likewise, the codified values for zone 3 is -4.9 and -3.8 for 18.4˚ deg roof and 26.4˚ deg roof, respectively. The same procedures were applied on the walls external pressure coefficients, and the codified peak min values shall be taken for as -2.5 and -2.0 for zone 5, and zone 4, respectively, and peak max value as 1.6 for both zones **Fig.3. 23**. The codified values using the statistical approach of a PDF value of 0.015 were compared with Davenport approach of 0.8 reduction factor, and it was concluded that both approaches are similar in estimating the critical codified pressure coefficients, as shown in **Table 3. 2**. The proposed codified values are more conservative compared to the latest three versions of ASCE 7, which shall play a crucial role in enhancing the wind standard and code of practices.

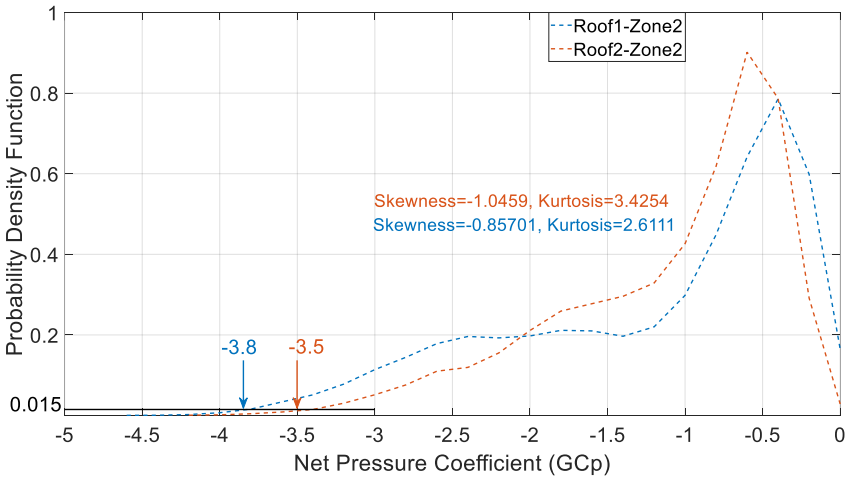

Fig.3. 21: Kernel fit distribution for zone 2 for both roof angles.

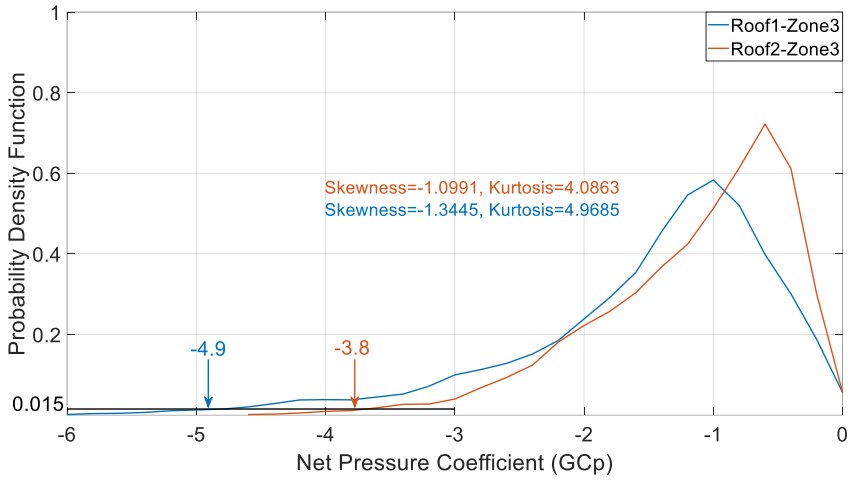

Fig.3. 22: Kernel fit distribution for zone 3 for both roof angles.

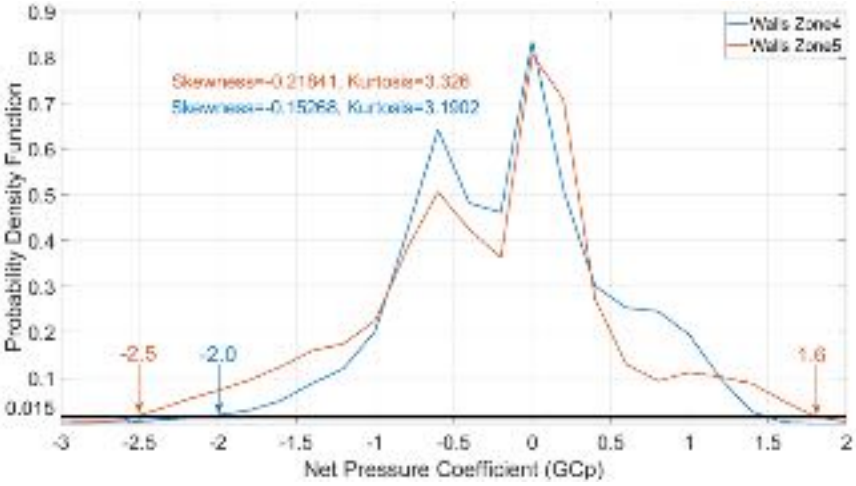

Fig.3. 23: Kernel fit distribution for zones 4 and 5 for walls.

Table 3. 2: A comparison of peak GC_p with Davenport and new statistical approaches.

	Critical measured GC_p	Davenport approach	Statistical approach	ASCE 7-10	ASCE 7-16	ASCE 7-22
Roof (18.4˚) zone 2	-4.55	-3.65	**-3.8**	-2.2	-3.1	-3.6
Roof (18.4˚) zone 3	-5.85	-4.7	**-4.9**	-3.7	-3.7	-3.6
Roof (26.6˚) zone 2	-4.2	-3.35	**-3.5**	-2.2	-2.5	-3.4
Roof (26.6˚) zone 3	-4.58	-3.65	**-3.7**	-3.7	-3.1	-3.4
Walls-Zone 4	-2.5	-2.0	**-2.0**	-1.1	-1.1	-1.1
Walls-Zone 5	-3.0	-2.4	**-2.5**	-1.4	-1.4	-1.4
Walls-Zones 4&5	1.90	1.5	**1.6**	1.0	1.0	1.0

3.9. Recommendation

Based on the area-averaged pressure analysis with the proposed statistical approach, and according to the latest three versions of ASCE 7, the following recommendations can be made towards codification:

- Zoning area for hip roof with overhangs shall not follow ASCE 7-22 and it is suggested to assign the edge of the overhangs to zone 2 and the corner to zone 3 as previous versions (**Fig.3. 24**).
- Roof slope categories as specified in ASCE 7-16 and ASCE 7-22 (i.e., $7^\circ < \theta \leq 20^\circ$ and $20^\circ < \theta \leq 27^\circ$) shall be maintained with no change.

- Elimination of h/B criteria for GC_p plots of roof angles $7^\circ < \theta \leq 20^\circ$ that was specified in ASCE 7-16, shall be maintained as ASCE 7-22, as it was found that the width of the building does not significantly affect the GC_p values.
- Wall zoning criteria shall be kept unchanged as specified in the last three versions.
- **Fig.3. 25** to **Fig.3. 27** provide recommended provisions for the design guidelines of overhangs for hip roof and walls based on the present study.

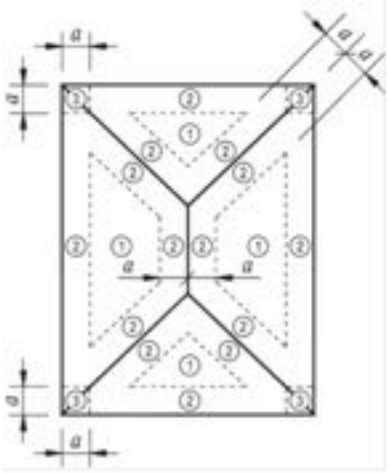

Fig.3. 24: Proposed zoning area for hip roof with overhangs; same as ASCE 7-10

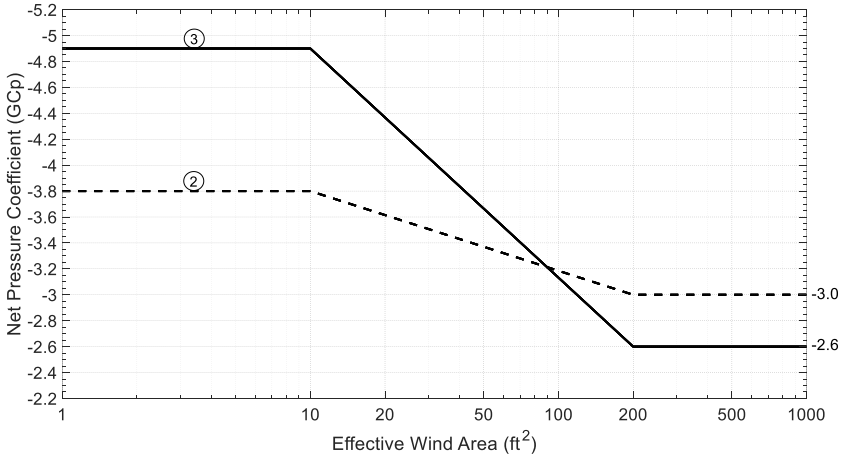

Fig.3. 25: Proposed provisions for $GC_{p,net}$ on roof overhangs of hip roof of angles $7^\circ < \theta \leq 20^\circ$

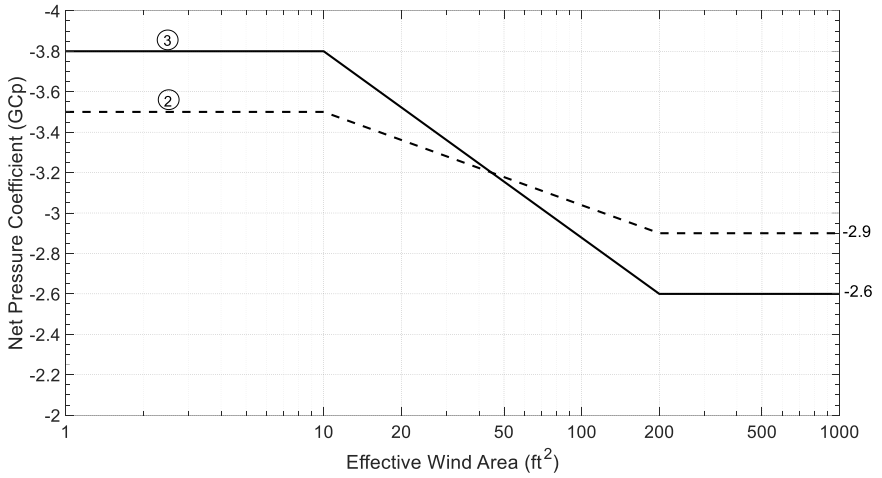

Fig.3. 26: Proposed provisions for $GC_{p,net}$ on roof overhangs of hip roof of angles $20^{\circ} < \theta \leq 27^{\circ}$

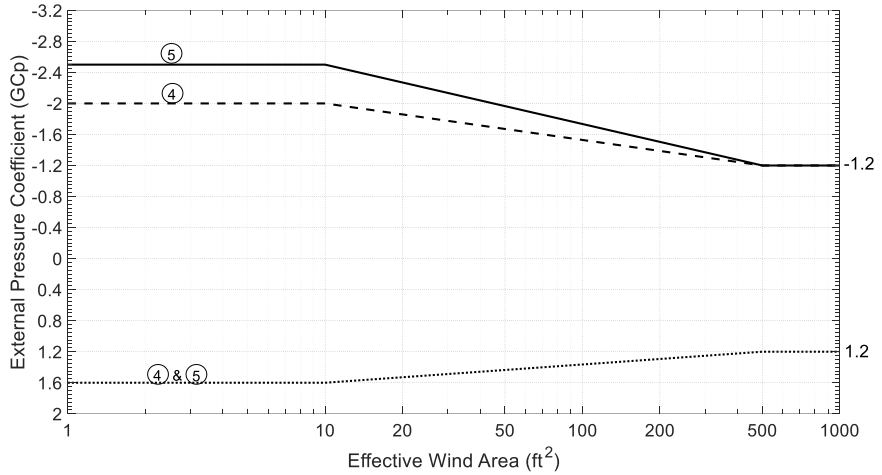

Fig.3. 27: Proposed provisions for $GC_{p,}$ for walls of enclosed, partially enclosed, and partially open buildings

CHAPTER IV. Machine Learning Techniques in Structural Wind Engineering

4.1. Introduction

The effect of wind-induced pressures on buildings and structural has a crucial role in structural design. The pressure coefficients acting upon the surfaces are usually driven either through code standards and provision or through wind tunnel testing. Generally, atmospheric boundary layer wind tunnel (ABLWT) is still the most accurate and reliable tool to study the aerodynamics of structures and buildings, that is able to provide the pressure coefficients, near surface speeds, and aeroelastic response. However, more recent methods such as computational fluid dynamics (CFD), surrogate models, and machine learning (ML) models become more popular in predicting the corresponding wind-induced pressures, wind velocities acting on buildings' surfaces, and wind flow characteristic. ABLWT and CFD simulation sometimes require significant time, cost, and expertise (Cóstola et al. 2009). Therefore, ML techniques have shown interest in identifying a reliable approach for wind-structure interaction in predicting wind speeds and wind-induced pressure. ML are a subset of artificial intelligence (AI) that have been involved across different domains and disciplines including engineering, business, and science over the last decades (Mjolsness and DeCoste 2001). Many recent studies have focused on the prediction of wind-induced pressures on buildings using ML techniques such as artificial neural networks (ANN). (Chen et al. 2003; Fu et al. 2007; Hu and Kwok 2020; Shruti et al. 2021), and the prediction of aeroelastic responses for bridges using ANN (Abbas et al. 2020; Chen et al. 2016; Wu and Kareem 2011). Some other studies used decision tree (DT), ensemble methods such as random forest (RF), extreme gradient boosting (XGB), to

predict surface pressure coefficients on buildings (Gu et al. 2021; Hu and Kwok 2020; Weng and Paal 2022). In addition, fuzzy neural networks (FNN) has been used in prediction of wind loads on large span roofs (Fu et al. 2007), wavelet neural networks (WNN), and convolutional neural network (CNN) have been used in prediction of wind loads on tall buildings (Chen et al. 2021; Oh et al. 2019). A recent state-of-the-art review study has reviewed and discussed the different ML techniques that have been implemented in structural wind engineering domain and the difference of error metrics that can be used in the assessment of model performance (Mostafa et al. 2022a).

Developing ML models require thousands and sometimes millions of data to be able to train the model accurately and show a robust performance on unseen data without being overfitted. This study used the experimental data gathered from the wind tunnel testing of large-scale testing of wind induced loads on roof overhangs that were carried out at the NSF NHERI Wall of Wind (WOW) experimental facility. ML models have been developed for predicting the wind-induced pressure on roof overhangs, soffits and walls using artificial neural networks, decision trees, and ensemble methods such as random forest. The mean, peak min, and peak max pressure coefficient data are used as the response output for training and testing the ML model. The testing process of the ML models aims to assess the performance of the model through some error metrics such as root mean square error (RMSE), correlation coefficient (R^2), mean square error (MSE), and mean averaged error (MAE). From the used three ML techniques, different models have been developed for predicting the mean, peak min, and peak max pressure coefficients each separately.

There are four main types of learning for ML algorithms: supervised learning, unsupervised learning, semi supervised learning, and reinforcement learning (Kang and Jameson 2018; Saravanan and Sujatha 2018). In supervised learning, the computer is trained with labeled set of data to develop predictive models through a relationship between the input and labeled data (i.e. regression and classification). In unsupervised learning, which is more complex, the computer is trained with unlabeled set of data to derive the structure present in the data by extracting general rules (i.e. clustering and dimensionality reduction). In semi-supervised learning, the computer is trained with a mixture of labeled and unlabeled sets. In reinforcement learning, which is so far the least common learning type, the computer acquire knowledge by observing the data through some iterations that require reinforcement signal, to identify the predictive behavior or action (i.e. make decisions) (Hastie et al. 2001; Murphy 2012). The following section will discuss briefly the three machine learning techniques that have been used in this study.

4.2. Machine learning techniques

This section discusses a brief theoretical background on the three ML techniques that have been implemented in this study; artificial neural networks (ANN), decision tree (DT), and random forest (RF) which is a method of the ensemble methods. In addition, this section provides the details of developing the models, the input data, and the output response. ML algorithms are data-hungry processes that require thousands if not millions of observations to reach acceptable performance levels (Mostafa et al. 2022a). There are so many other ML models that can be implemented in structural wind engineering domain, only the used three methods that have been used in this study were discussed briefly.

4.2.1. Artificial neural networks

The concept of ANN is derived from biological sciences, where it mimics the complexity of human brain in recognizing patterns through biological neurons, and thus imitate the process of thinking, recognizing, make decisions, and solve problems (Haykin 2010a; Nasrabadi 2007). ANN has been the most popular method found in the reviewed literature to predict wind-induced pressures, compared to other neural network methods (e.g. CNN or RNN). ANN is robust enough to solve multivariate and nonlinear modeling problems, such as classification and predictions. ANN is a group of layers that comprise multiple neurons at each layer and is also known as Feed-Forward neural network (FFNN). It is composed of input layers, where all the variables are defined and fed into the hidden layers which are weighted and fed into the output layers that represent the response of the operation. The ANN architecture could be written as x-h-h-y which define x number of inputs (variables), h number of hidden layers, and y number of outputs (responses) as shown in **Fig.4. 1**. Each hidden layer comprises of a certain number of neurons that gives a robust model, and this could be achieved by training and trials.

The hidden layers composed of activation functions that apply different weights to the input layer and transfer them to the output layers. The most common activation functions are the nonlinear continuous sigmoid, the tangent sigmoid, and the logarithmic sigmoid (Haykin 2010b). The weights are multiplied with the inputs and calibrated through a training process between the input and output layers to reduce the loss. The training process is applied using the Levenberg Marquardt backpropagation algorithm, which belong to the family of Multi-Layer Perceptron (MLP) network (Waszczyszyn and Ziemiański 2005) and was originally proposed by Rumelhart et al. (Rumelhart et al. 1986).

It consists of two steps: feed forward the values to calculate the error, and then propagate back the error to previous layers (Hagan and Menhaj 1994; Marquardt 1963). The repeated iteration process (epochs) of backpropagation network error continues and it keeps adjusting the interconnecting weights until the network error is reduced to an acceptable level. Once the most accurate solution is formed during the training process, the weights and biases are fixed, and the training process stops. The Levenberg Marquardt is a standard numerical method where it achieves the second order training speed with no need to compute the Hessian matrix and has been demonstrated to be efficient with training networks up to a few hundred weights (Demuth and Beale 1998; Hagan and Menhaj 1994). **Fig.4. 2** shows the output signal for a generic neuron j in the hidden layer h defined in equation 1, where w_{ij}^{h} is the weight that connects the i^{th} neuron of the current layer to the j^{th} neuron of the following layer, x_i is the input variable, b is the bias associated with the j^{th} neuron to adjust the output along with the weighted sum, and f is the activation function that is usually adapted as either a tangent sigmoid or a logarithmic sigmoid, Eq.(11-13) respectively. The (RBF-NN) that was used first by (Broomhead and Lowe 1988), is a function whose response either decreases or increases with the distance from a center point (Bianchini et al. 1995; Park and Sandberg 1991).

$$y_j^h = f\left(\sum_{i=1}^{n} w_{ij}^h x_i^h + b_j^k\right) \tag{11}$$

$$f\,(u) = -1 + \frac{2}{(1 + e^{-2u})} \tag{12}$$

$$f\,(u) = \frac{1}{(1 + e^{-u})} \tag{13}$$

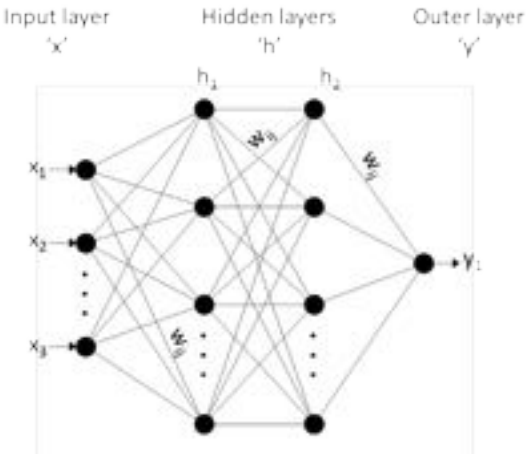

Fig.4. 1: Feed-Forward neural network architecture

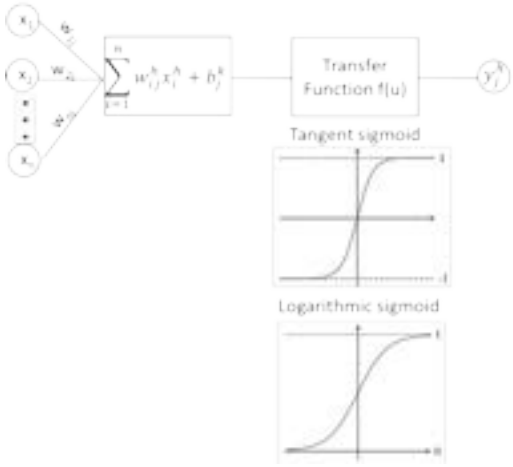

Fig.4. 2: The generic model of neuron *j* in hidden layer *h*

During the training process of BPNN, usually the training is terminated when one of the following criteria is first met: (i) fixing the number of epochs to a certain number, (ii) the training error is less than a specific training goal, or (iii) the magnitude of the training gradient is less than a specified small value (i.e. 1.0×10^{-10}). The training error is the error obtained from running the trained model back on the data used in the training process, while the training gradient is the error calculated as a direction and magnitude during the training of the network that used to update the network weight in the right direction and amount.

4.2.2. Decision Tree (DT)

The DT method is one of the supervised ML models, where the algorithm assigns the output through testing in a tree of nodes and by filtering the nodes (decision nodes) down within the split sub-nodes (leaf nodes) to reach to the final output. The decision trees may differ in several dimensions such as the test might be multivariate or univariate, or the test may have two or more outcomes, and the attributes might be numeric or categorical (Loh 2011, 2014; Nilsson 2005).

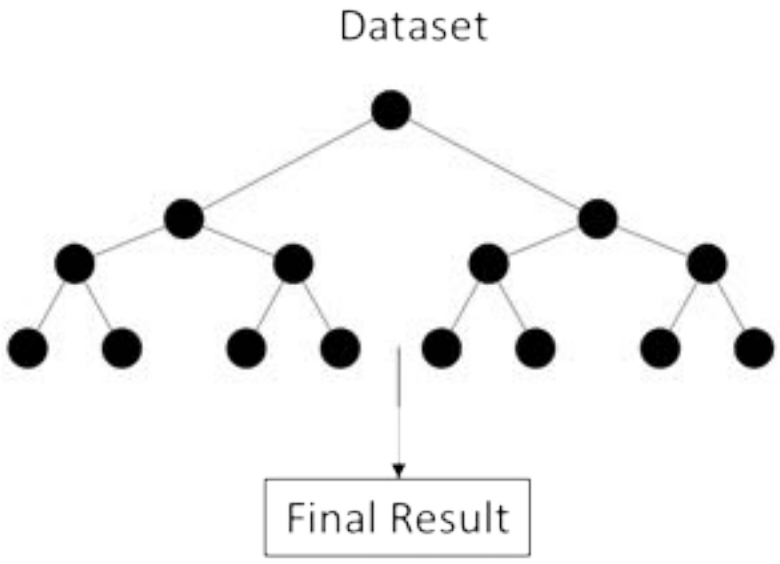

A sketch showing the architecture for decision tree

4.2.3. Ensemble methods

The EM methods include: (1) bagging regression tree that is also referred to as the random forest (RF) algorithm, (2) gradient boosting regression tree (GBRT) or decision tree (GBDT), and (3) extreme gradient boosting (XGB). All EM methods could be defined as a combination of different decision trees to overcome the weakness that may occur in a single tree such as sensitivity to training data and unstableness (Zhou 2012). The forest

generated by the RF algorithm is either trained through bagging, that was proposed by Breiman (Breiman 1996) or through bootstrap aggregating (Hastie et al. 2009). RF splits in each node n features among the total m features, where n is recommended to be $\frac{1}{3m}$ or $\sqrt{2m}$ (Breiman 2001). It reduces the overfitting of datasets and increases precision. Overfitting is overtraining the model which causes it to be particular to certain data sets and lose the generalized aspect desired in ML models. The DT and RF methods are commonly used in classification and regression problems.

GBRT, or also known as GBDT as mentioned above, was first developed by Friedman (Friedman 2001), and is one of the most powerful ML techniques deemed successful in a broad range of applications (Natekin and Knoll 2013; Persson et al. 2017). GBDT combines a set of weak learners called classification and regression tree (CART). To eliminate overfitting, each regression tree is scaled by a factor, called learning rate (Lr) that represents the contribution of each tree to the predicted values for the final model. The predicted values are computed as the sum of all trees multiplied by the learning rate (Elith et al. 2008). Lr with maximum tree depth (Td) determines the number of regression trees for building the model (Hu and Kwok 2020). Previous studies proved that smaller Lr decrease the test error but increase computational time (Natekin and Knoll 2013; Persson et al. 2017; Zhang and Haghani 2015). A subsampling procedure was introduced by Friedman [61] to improve the generation capability of the model using subsampling fraction (Fs) that is chosen randomly from the full date set to fit the base learner.

Another popular method from the EM family is the XGBoost, or XGB as defined above, which is similar to the random forest and was developed by Chen and Guestrin

(Chen and Guestrin 2016). XGB has more enhancement compared to other ensemble methods. It can penalize more complex models by using both LASSO (L1) and Ridge (L2) regularization to avoid overfitting. It handles different types of sparsity patterns in the data, and it uses the distributed weighted quantile sketch algorithm to find split points among weighted datasets. There is no need to specify in each single run the exact number of iterations as the algorithm has a built-in cross validation that takes care of this task.

4.3. Prediction of wind-induced pressures on surfaces using ML techniques

Three machine learning techniques, artificial neural networks, decision trees, and random forest, have been used for predicting the mean and peak pressure coefficients among the wall, the soffits, and the overhangs surfaces. The theoretical background for the three techniques that were used in predicting were discussed earlier in this chapter.

4.3.1. Training, testing, and validating datasets

ML models are developed using two main types of datasets which are training datasets and validating datasets. As discussed earlier, wind tunnel testing was carried out on eight different models in the WOW. The datasets from six models were used in developing the machine learning models. It is important to note that the remaining two models (G and H) are similar to two of the six models (D and E) but without horizontal soffit, therefore no need to train the datasets from G and H. Each of the six models was tested under 40 different wind directions, therefore a total of 240 datasets were used for developing the ML models. 24 datasets were kept and have not been seen by the model for validating the developed ML models. The 24 datasets composed of data from four wind directions (0˚,90˚,180 ˚ and 270 ˚) from the six models. All the other datasets from the

remaining 36 wind directions were used as training datasets for training and testing processes, which formed a total of 216 datasets.

For testing the performance of the ML model, a cross validation process has been used. Most of the previous studies have adopted the three-stage evaluation process of training, testing and validation (TTV), which was proposed by (Reich and Barai 1999) to build a robust ML model. The cross-validation process comprises two steps: first, the dataset is randomly shuffled and is divided into k subsets of similar sizes, then k − 1 sets are used for training and one set is used as the testing set to assess the performance of the model. The stability and the accuracy of the validation method depend mainly on the k value. Hence, the cross-validation method is usually referred to as k-fold cross-validation (Browne 2000; Reich 1997) and is illustrated in **Fig.4. 3**. Many of the reviewed studies used the 10-fold CV method following Refaeilzadeh et al.'s recommendation (Refaeilzadeh et al. 2009) of using k = 10 as a good estimate.

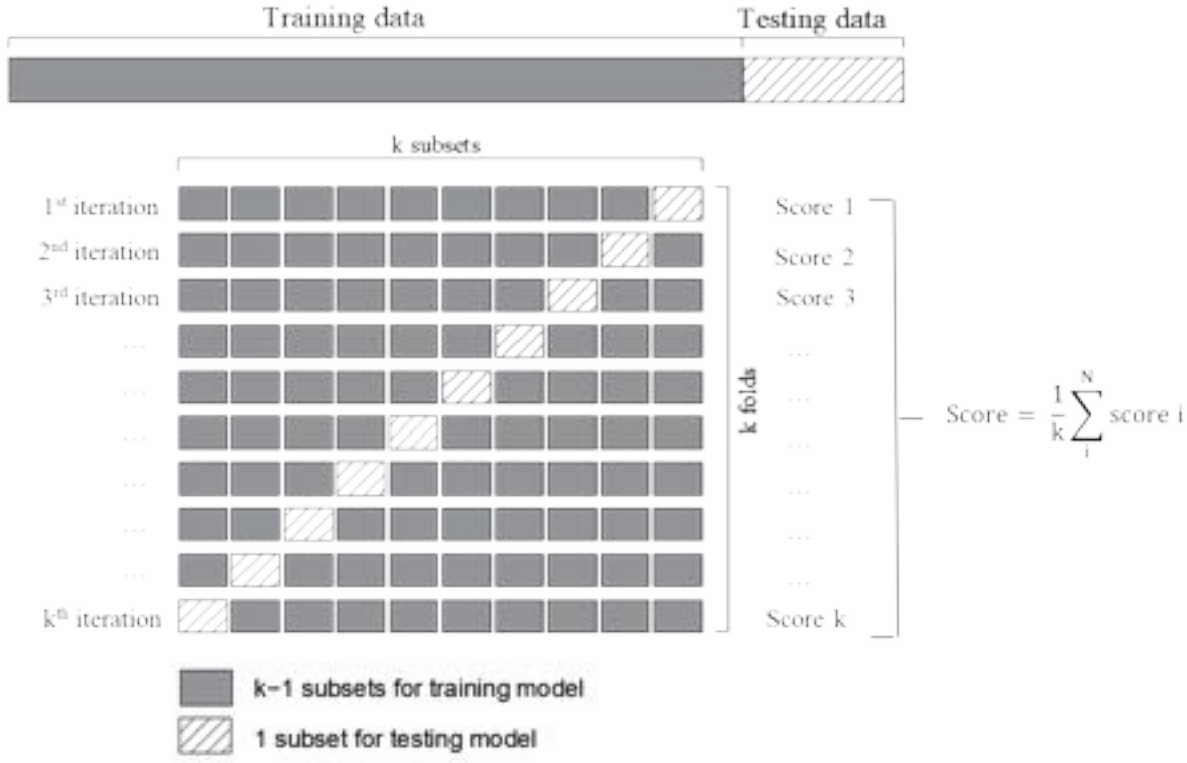

Fig.4. 3: Illustration of the *k*-fold cross-validation method

For developing the ML models, six input parameters were used for training and testing processes. The input parameters included the x,y,z coordinates of all the pressure taps, roof slope (β), overhangs width (OH_w), and wind directions (α). The predicted output response is either mean pressure coefficient ($\overline{Cp}$), peak min pressure coefficient ($\widetilde{Cp}$) or peak max pressure coefficient($\widehat{Cp}$) for walls and soffits surfaces. Thus, three different predictive models were developed using the three mentioned ML techniques (ANN, DT and RF).

4.3.2. Predictions of Pressure Coefficients using Feed Forward Neural Networks

The feed forward neural networks are composed of input layer (x) which has six variable parameters, three hidden layers (h), and one output layer (y). The output layer (y)

is either ($\overline{Cp}$), ($\widetilde{Cp}$), or ($\widehat{Cp}$). **Fig.4. 4** shows a typical neural network architecture that has been used for developing the models of this study. The number of hidden layers in Feed forward ANN were chosen after different iterations to have a high accuracy error metric performance as will be discussed later. **Fig.4. 4** shows the typical neural network architecture that has been used for developing the models of this study and **Table 4. 1** shows the parameters of the developed ANN for pressure coefficients prediction. The number of neurons in hidden layers were determined through many iterations until the error metrics gave the highest performance and least error metric. In predicting the mean pressure coefficient for walls and soffit, three hidden layers were used with 26-22-16 neurons, and for peak max pressure coefficients, 28-23-16 neurons were used in the three layers. While, for predicting the peak min pressure coefficient 49-42-32 neurons in the three layers were used. The model for predicting the peak min pressure coefficient gave the least performance compared to the other models due to the big variations in measured data. In previous studies, the ANN usually used for predicting the mean pressure coefficient due to the high accuracy in prediction. While the peak pressure coefficients were not that accurate due to the small amount of data exposed to higher peak pressure coefficient, which sometimes can be considered as outliers in training the model.

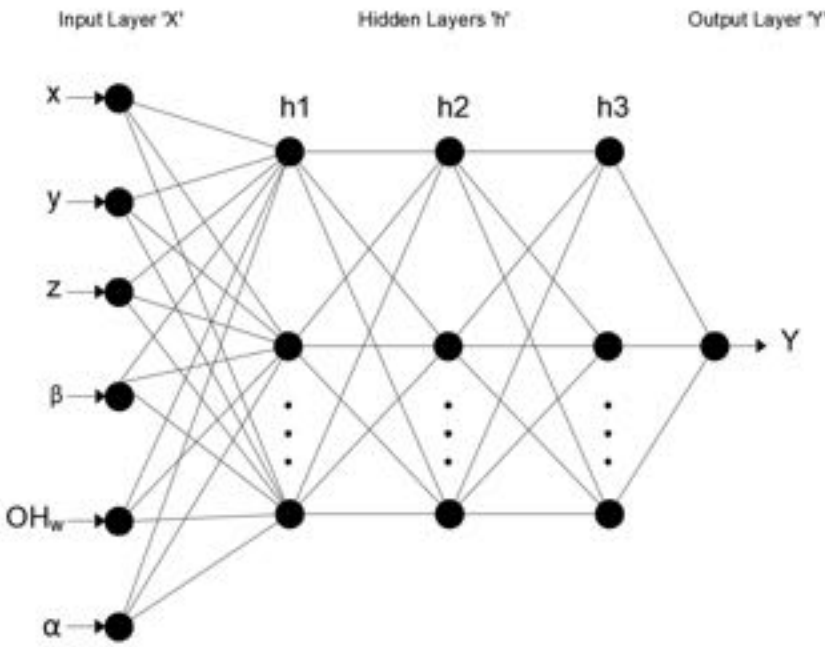

Fig.4. 4: Typical neural network architecture used in the present study (6-h-h-h-1)

Table 4. 1: parameters of developed ANN models

	Walls and Soffit surfaces		
Inputs	x, y, z, β, OH_w, α		
Output	$\overline{Cp}$	$\widehat{Cp}$	$\widetilde{Cp}$
Network structures	6-26-22-16-1	6-28-23-16-1	6-49-42-32-1
Transfer function	Tangent sigmoid $f(u) = -1 + \frac{2}{(1+e^{-2u})}$ 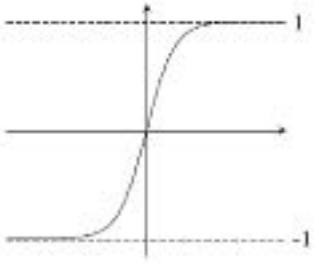		
Training data	α= 0˚ to 360˚ except for 0 ˚,90 ˚,180 ˚ and 270 ˚		
Validating data	0˚,90˚,180˚ and 270˚		

4.4. Model performance assessment

The performance of the ML models in wind engineering applications throughout the reviewed literature was assessed through at least one or more forms of different standard statistical error and standard indices. It is important for any ML model to evaluate the performance of the model using some error metrics or factors. The compiled list of metrics, or factors, calculates the error to evaluate the accuracy between the ML predicted data and a form of ground truth such as experimental data or independent sets of data that were not used in training among others. There is always a lack of consensus on the most accurate metric that can be used.

Several error metrics were used throughout the reviewed literature which include: Akaike information criterion (AIC), coefficient of efficiency (Ef), coefficient of determination (R^2), Pearson's correlation coefficient (R), mean absolute error (MAE), mean absolute percentage error (MAPE), mean square error (MSE), root mean square error (RMSE), scatter index (SI), and sensitivity error (Si). Four error metrics have been used in assessing the performance of the models in this study, which are (R^2), (RMSE), (MSE), (MAE). The equations used to express each of these error metrics for assessing predicted data (p_i) against measured data (m_i) are summarized below Eq.(14-17). For N number of data points (e.g., N could be the number of pressure taps used to provide experimental data), some of the error calculation equations also use average or mean values for predicted data ($\bar{p}$) as well as measured data ($\overline{m}$).

$$R^2 = \frac{\sum_i^N (m_i - \bar{m})(p_i - \bar{p})}{\sqrt{\sum_i^N (m_i - \bar{m})^2 \sum_i^N (p_i - \bar{p})^2}} \quad (14)$$

$$RMSE = \sqrt{\frac{1}{N}\sum_i^N (p_i - m_i)^2} \quad (15)$$

$$MSE = \frac{1}{N}\sum_i^N (\frac{p_i - m_i}{m_i})^2 \quad (16)$$

$$MAE = \frac{1}{N}\sum_i^N |m_i - p_i| \quad (17)$$

In general, MSE was employed in most of the studies and is considered one of the most common error metrics for pressure distribution prediction, but it is not always an accurate error metric. The MSE accuracy decreases when the pressure among the walls is included in the prediction because walls might introduce a pressure coefficient near zero which may cause a great rise as the normalizing denominator (Chen et al. 2021). Nevertheless, MSE is generally stable when used in RF models when the number of trees reaches 100 (Mallick et al. 2020). The RMSE is not affected by the near-zero pressure coefficient as with MSE because it does not include a normalization factor in the calculation. Nevertheless, the lack of normalization is considered a limitation for this metric in the cases where the scale of pressure coefficients changes (Chen et al. 2021). The accuracy of some metric errors increases when their values approach one (i.e., coefficient of determination-R^2), which means that the predicted data are close to the experimental data, and the accuracy of some others increases when their values are close to zero (i.e., root mean square error-RMSE).

Overall, it is important to note that each error metric or factor usually conveys specific information regarding the performance of the ML model, especially in the case of

wind engineering applications (due to variation of wall versus roof pressures for instance), and most of these metrics and factors are interdependent. **Table 4. 2** and **Table 4. 3** show the performance metrics for the developed ML techniques for walls and soffit, respectively. It is apparent that the overall performance of the model is acceptable in terms of predicting the pressure coefficients on the surfaces. However, the ANN models gave the highest accuracy based on the error metric used in assessment.

Table 4. 2 Error metric used in models' assessments for walls.

Index	ANN		DT		RF	
	Training	Validating	Training	Validating	Training	Validating
R^2	0.96	0.99	0.98	0.90	0.98	0.90
RMSE	0.087	0.064	0.071	0.182	0.058	0.1831
MSE	0.007	0.004	0.005	0.033	0.003	0.033
MAE	0.054	0.05	0.035	0.124	0.034	0.123

Table 4. 3 Error metric used in models' assessments for soffits.

Index	ANN		DT		RF	
	Training	Validating	Training	Validating	Training	Validating
R^2	0.96	0.92	0.97	0.89	0.98	0.89
RMSE	0.086	0.130	0.074	0.1527	0.057	0.15
MSE	0.007	0.017	0.0054	0.0233	0.003	0.022
MAE	0.055	0.095	0.0416	0.1052	0.033	0.1045

4.5. Predicting peak and mean pressure coefficient

For validating the performance and accuracy of the developed models, the models have been used to predict the peak max and mean pressure coefficients for walls and soffits for one of the untrained wind directions (i.e. 180˚). The peak max pressure coefficients were predicted for south wall of Model A at 180˚ wind direction, then the predicted pressure coefficients were used in plotting the contour plots for the wall (**Fig.4. 6**).

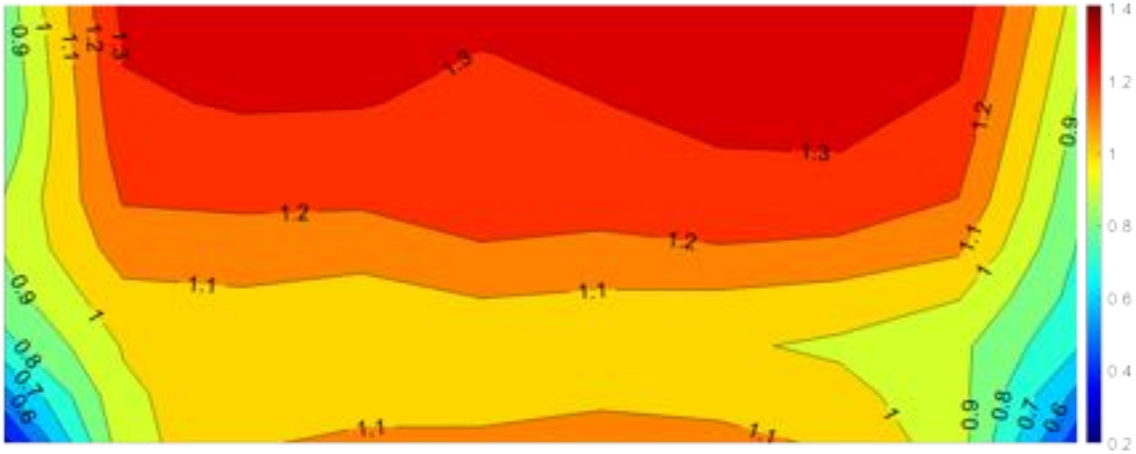

(a)

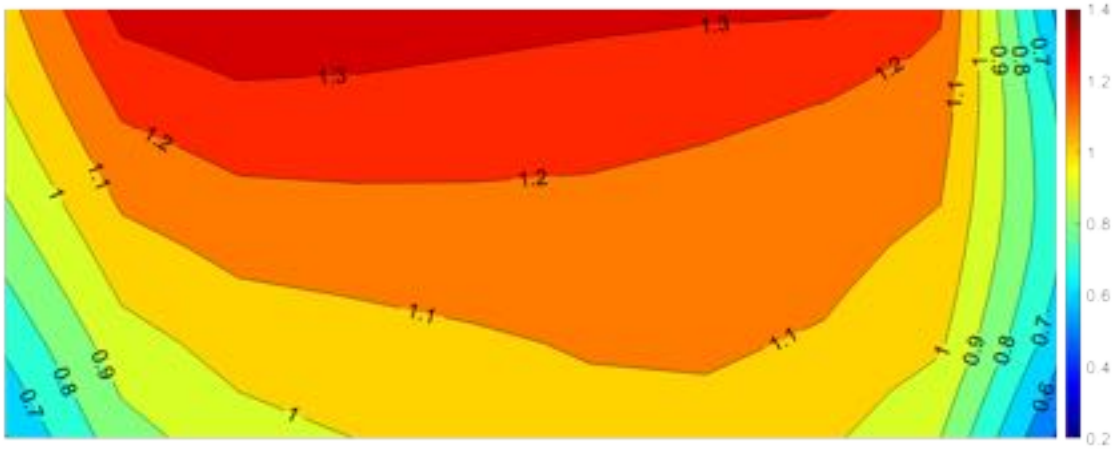

(b)

Fig.4. 5: Peak max pressure coefficient contour plots for south wall of Model A at wind direction of 180º from (a) experimental model (b) ANN model (c) DT model (d) RF model

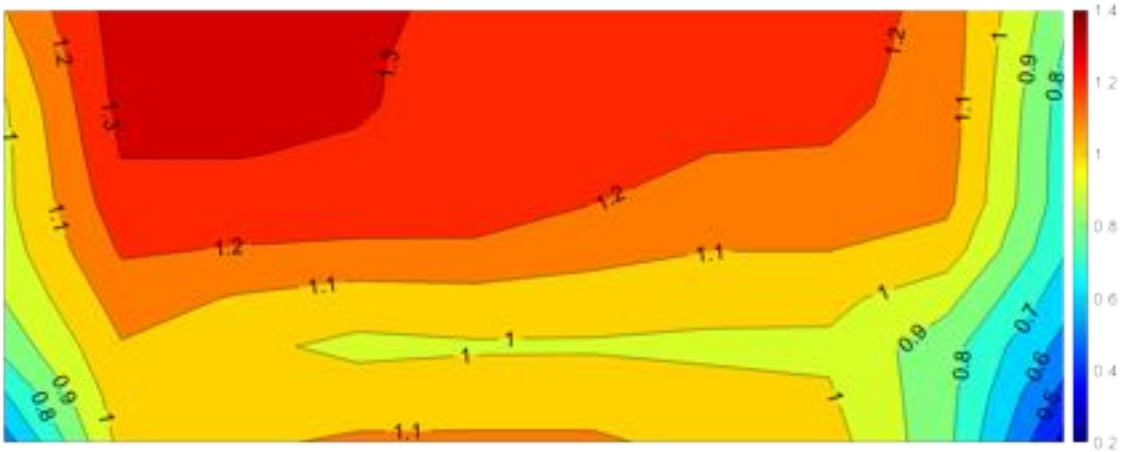

(c)

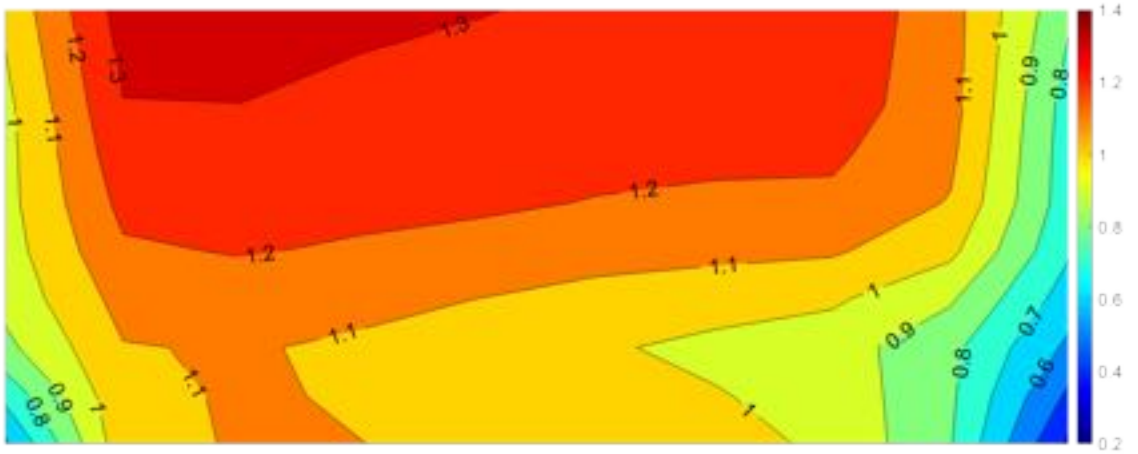

(d)

Fig.4. 6 (cont.): Peak max pressure coefficient contour plots for south wall of Model A at wind direction of 180º from (a) experimental model (b) ANN model (c) DT model (d) RF model

The mean pressure coefficient model using ANN was validated using the regression analysis between the measure and predicted mean pressure coefficient for Model A south soffit. The four untrained wind directions (i.e. 0˚,90˚,180˚ and 270˚) were used in validating the model (**Fig.4. 7**).The positive mean pressure coefficients in the plot are associated with 180˚ wind direction, and the negative mean pressure coefficients are associated with 0˚,90˚ and 270˚ wind directions. The R^2 factor between the measured and predicted values is 0.99,

which concludes a high accuracy in predicting the data. The developed ANN model was robust enough to predict the unseen data in the trained model. It is highly recommended to use ANN for predictions in structural wind engineering.

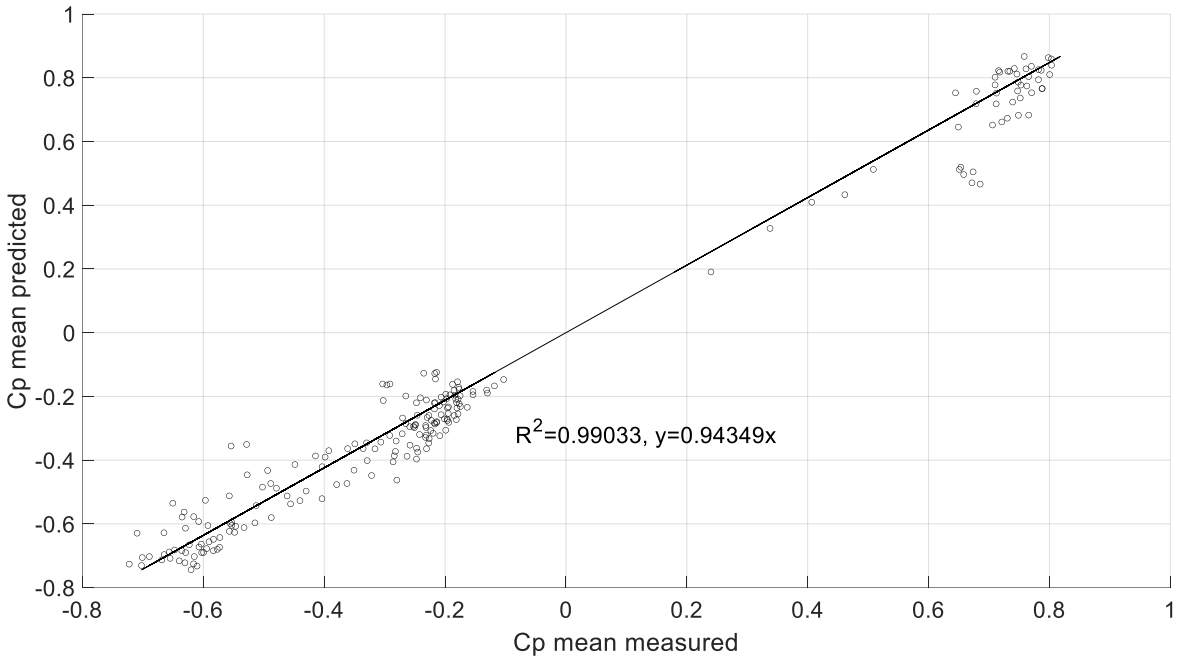

Fig.4. 7: Predicted and measured mean pressure coefficient for soffit of model C for tested wind directions using ANN model.

V. Summary and Conclusion

5.1. Summary

Large scale wind tunnel experiments were conducted at the Wall of Wind Experimental Facility at Florida International University for eight models of a two-story residential building with hip roof of two slopes (4:12 and 6:12) and different overhang widths (0.6 m, 1.2 m, and 1.8 m). Peak and mean local surface pressure coefficients were recorded for walls, soffits, and roofs with overhangs for all models that have been used in area-averaging analysis, regression, and correlation analyses. The regression analysis was considered to assess the correlation of soffit pressure coefficients to pressure coefficients of wall upper taps. The area-averaged analysis was used to develop a codification study that shall enhance the wind standards and code provision in terms of design guidelines for roof overhangs.

Area averaged pressure coefficients were measured for different combinations of taps and were compared to GC_p plots in ASCE 7-10, ASCE7-16 and ASCE 7-22. Area averaging and pressure coefficients for overhangs, and adjacent roof areas were compared to GC_p plots in the latest three versions of ASCE 7 for each specified zone. The Standards are less conservative regarding zone 2e/2 and zone 3 for most of the cases. In addition, an empirical model was developed to govern the relation between wall pressure coefficient and soffit pressure coefficient while considering overhang widths.

Machine learning techniques have been used in predicting the mean and peak pressure coefficients among the walls, soffits, and roof overhang. The ANN technique gave the highest performance in terms of predicting the pressure coefficients, and higher error

metrics accuracy compared to the other machine learning techniques such as decision trees and random forest.

5.2. Observations and Conclusions of Dissertation

Based on experimental testing results and discussion, the following observed/concluded remarks can be drawn:

- The 0.6 m inclined overhangs were found to have higher pressure coefficient at the edges compared to the 1.2 m and 1.8 m overhangs.
- Pressure taps at the soffit edge exposed to higher peak min Cp compared to the middle and inner taps.
- The width of the overhang did not seem to have a considerable effect on the absolute positive pressure correlation between walls and soffits.
- The width of the overhang has a recognized effect on the negative pressure correlation between walls and soffits.
- The 1.8 m soffit appeared to be less correlated at the edge with the wall upper taps compared to the 0.6 m and 1.2 m soffit.
- The correlation coefficients for wider soffits with the wall significantly decrease compared to narrower soffits when the walls and soffits are exposed to suctions.
- The soffit pressure coefficients shall be taken as the adjacent wall external pressure, as stated by ASCE 7-16/7-22 for positive pressure only, while this shall not be applicable for suction pressure.
- Roof with steeper slope (i.e., 26.6˚) experience lower suction along the roof surface compared to roofs with less steep slope (i.e. 18.4˚)

- GC_p plots in the latest three versions of ASCE 7 for hip roof of both angle ranges $7^o < \theta \leq 20^o$ and $20^\circ < \theta \leq 27^\circ$ might be less conservative compared to the experimental results regarding zone 2e/2 and zone 3.
- GC_p plots in the latest three versions of ASCE 7 for walls might be less conservative compared to the experimental results regarding zones 4 and 5.
- It is important to include a revised codification approach in the upcoming version of wind codes and standards considering all previous wind load studies on roof overhangs.
- Machine learning models were robust enough to be used in structural wind engineering to predict pressure coefficients on buildings surfaces.

5.3. Possible Design Recommendations and Code Changes

The findings from the peak pressure coefficients show that the 0.6 m overhang experienced higher suction coefficients at the edges compared to the 1.2 m and 1.8 m overhang. In addition, the findings show that the steeper the slope, the less suction experienced by the roof. Furthermore, the results confirmed that, for all models, soffit positive pressure coefficients may be taken as the adjacent wall external pressure, as stated by ASCE 7-16, but this is not valid for negative pressure coefficients. The width of the overhang did not seem to have a considerable effect on the positive pressure coefficient on walls and soffit, while it has a recognizable effect of negative pressure coefficients.

Accordingly, a codification study was proposed to account for the less conservative design guidelines in the previous versions of standards. The codification study was developed based on kernel fit distribution statistical approach which showed similar results

to the reduced factor approach of 0.8 by Davenport. Many recommendations have been given in terms of roof slope, zoning area, and net pressure coefficient (GC_p) plots with effective area for roof overhangs. In addition, an empirical model was developed that governs the relation between soffit pressure coefficient and wall pressure coefficient for both positive and negative pressure/suction.

Finally, it can be concluded that machine learning techniques is a powerful tool in predicting surface pressure that may save time and cost of wind tunnel testing.

VI. Future work and Recommendations

- The wind tunnel testing that were carried out at the WOW focused mainly on hip roofs with only two different roof slopes, and the findings have shown that some of the GC_p plots in the last three versions of the ASCE Wind Standard are less conservative compared to the experimental results. Therefore, more comprehensive large scale testing may be needed for different roof shapes with overhangs (i.e. gable roofs), and different roof angles ($27^\circ < \theta \leq 45^\circ$).
- Roof overhangs for irregular shape buildings may be studied under wind loads to expand the codification study for code enhancement.
- The large-scale testing of roof overhangs was conducted as aerodynamic testing under wind induced loads generated by the fans similar to the field wind profile in open terrain. Roof overhangs may be studied under downburst loads instead of the conducted aerodynamic testing under typical wind loads. It would be worthwhile generating testing phases for different roof slopes and overhangs width under downburst loads.
- Machine learning models can predict pressure coefficients on the surfaces of irregular shapes that have been tested before at the WOW. Since a huge number of datasets and buildings types have been tested experimentally, thus these datasets can be used for training a ML model to predict the surface pressure for irregular building shapes such as L shape or T shape.

References

Abbas, T., Kavrakov, I., Morgenthal, G., and Lahmer, T. (2020). "Prediction of aeroelastic response of bridge decks using artificial neural networks." *Computers and Structures*, Elsevier Ltd, 231, 106198.

Ahmad, S., and Kumar, K. (2002). "Effect of geometry on wind pressures on low-rise hip roof buildings." *Journal of Wind Engineering and Industrial Aerodynamics*.

Asghari Mooneghi, M., Irwin, P., and Gan Chowdhury, A. (2016). "Partial turbulence simulation method for predicting peak wind loads on small structures and building appurtenances." *Journal of Wind Engineering and Industrial Aerodynamics*, Elsevier, 157, 47–62.

Banks, D., Guha, T. K., and Fewless, Y. J. (2015). "A hybrid method of generating realistic full-scale time series of wind loads from large-scale wind tunnel studies: Application to solar arrays." *Proceedings of the 14th International Conference on Wind Engineering*, 21–26.

Bianchini, M., Frasconi, P., and Gori, M. (1995). "Learning without local minima in radial basis function networks." *IEEE transactions on neural networks*, IEEE, 6(3), 749–756.

Breiman, L. (1996). "Bagging predictors." *Machine learning*, Springer, 24(2), 123–140.

Breiman, L. (2001). "Random forests." *Machine learning*, Springer, 45(1), 5–32.

Broomhead, D. S., and Lowe, D. (1988). *Radial basis functions, multi-variable functional interpolation and adaptive networks*. Royal Signals and Radar Establishment Malvern (United Kingdom).

Browne, M. W. (2000). "Cross-validation methods." *Journal of mathematical psychology*, Elsevier, 44(1), 108–132.

Candelario, J. D., Stathopoulos, T., and Zisis, I. (2014). "Wind Loading on Attached Canopies: Codification Study." *Journal of Structural Engineering*, 140(5), 04014007.

Chen, B., Wu, T., Yang, Y., Yang, Q., Li, Q., and Kareem, A. (2016). "Wind effects on a cable-suspended roof: Full-scale measurements and wind tunnel based predictions." *Journal of Wind Engineering and Industrial Aerodynamics*, Elsevier, 155, 159–173.

Chen, F. B., Wang, X. L., Li, X., Shu, Z. R., and Zhou, K. (2021). "Prediction of wind pressures on tall buildings using wavelet neural network." *Journal of Building Engineering*, 46(November 2021), 103674.

Chen, T., and Guestrin, C. (2016). "Xgboost: A scalable tree boosting system." *Proceedings of the 22nd acm sigkdd international conference on knowledge discovery and data mining*, 785–794.

Chen, Y., Kopp, G. A., and Surry, D. (2003). “Prediction of pressure coefficients on roofs of low buildings using artificial neural networks.” *Journal of Wind Engineering and Industrial Aerodynamics*, 91(3), 423–441.

Cóstola, D., Blocken, B., and Hensen, J. L. M. (2009). “Overview of pressure coefficient data in building energy simulation and airflow network programs.” *Building and Environment*, Elsevier Ltd, 44(10), 2027–2036.

Davenport, A. G., Stathopoulos, T., and Surry, D. (1985). “Reliability of wind loading specifications for low buildings.” *Proceedings of the Fourth International Conference on Structural Safety and Reliability*.

Demuth, H., and Beale, M. (1998). “Neural Network Toolbox for Use with MATLAB, the Math Works Inc.” *Natick, MA*, 10–30.

Elith, J., Leathwick, J. R., and Hastie, T. (2008). “A working guide to boosted regression trees.” *Journal of animal ecology*, Wiley Online Library, 77(4), 802–813.

Friedman, J. H. (2001). “Greedy function approximation: a gradient boosting machine.” *Annals of statistics*, JSTOR, 1189–1232.

Fu, J. Y., Liang, S. G., and Li, Q. S. (2007). “Prediction of wind-induced pressures on a large gymnasium roof using artificial neural networks.” *Computers and Structures*, 85(3–4), 179–192.

Gan Chowdhury, A., Zisis, I., Irwin, P., Bitsuamlak, G., Pinelli, J.-P., Hajra, B., and Moravej, M. (2017). “Large-scale experimentation using the 12-fan wall of wind to assess and mitigate hurricane wind and rain impacts on buildings and infrastructure systems.” *Journal of Structural Engineering*, American Society of Civil Engineers, 143(7), 4017053.

Gu, S., Wang, J., Hu, G., Lin, P., Zhang, C., Tang, L., and Xu, F. (2021). “Prediction of wind-induced vibrations of twin circular cylinders based on machine learning.” *Ocean Engineering*, Elsevier Ltd, 239(January), 109868.

Guo, Y., Wu, C.-H., and Kopp, G. A. (2021). “A method to estimate peak pressures on low-rise building models based on quasi-steady theory and partial turbulence analysis.” *Journal of Wind Engineering and Industrial Aerodynamics*, Elsevier, 218, 104785.

Hagan, M. T., and Menhaj, M. B. (1994). “Training feedforward networks with the Marquardt algorithm.” *IEEE transactions on Neural Networks*, IEEE, 5(6), 989–993.

Hastie, T., Tibshirani, R., and Friedman, J. (2001). “The elements of statistical learning. Springer series in statistics.” :, Springer.

Hastie, T., Tibshirani, R., and Friedman, J. (2009). “Unsupervised learning.” *The elements of statistical learning*, Springer, 485–585.

Haykin, S. (2010a). “Neural networks: a comprehensive foundation. 1999.” *Mc Millan, New Jersey*, 1–24.

Haykin, S. (2010b). *Neural networks and learning machines, 3/E*. Pearson Education India.

Ho, T. C. (1992). "Variability of low building wind loads." Ph.D. Thesis, The University of Western Ontario, London, Ontario, Canada, 1992.

Hu, G., and Kwok, K. C. S. (2020). "Predicting wind pressures around circular cylinders using machine learning techniques." *Journal of Wind Engineering and Industrial Aerodynamics*, Elsevier Ltd, 198(November 2019), 104099.

Huang, P., Tao, L., Gu, M., and Quan, Y. (2018). "Experimental study of wind loads on gable roofs of low-rise buildings with overhangs." *Frontiers of Structural and Civil Engineering*, 12(3), 300–317.

John, A. D., Gairola, A., and Krishna, P. (2008). "Wind Loads on Overhangs in a Low Gable Building in Presence of Free Standing Wall." *Journal of Wind and Engineering*, 5(1), 39–46.

John, A. D., Singla, G., Shukla, S., and Dua, R. (2011). "Interference effect on wind loads on gable roof building." *Procedia Engineering*, Elsevier B.V., 14, 1776–1783.

Kang, M., and Jameson, N. J. (2018). "Machine Learning: Fundamentals." *Prognostics and Health Management of Electronics: Fundamentals, Machine Learning, and the Internet of Things*, Wiley Online Library, 85–109.

Loh, W. (2011). "Classification and regression trees." *Wiley interdisciplinary reviews: data mining and knowledge discovery*, Wiley Online Library, 1(1), 14–23.

Loh, W. (2014). "Fifty years of classification and regression trees." *International Statistical Review*, Wiley Online Library, 82(3), 329–348.

Majid, T. A., Zaini, S. S., Ismail, M. A., Deraman, N. C., and Poon, J. L. (2016). "Numerical investigation on the effect of overhang roof around rural house." *The 2016 World Congress on Advances in Civil, Environmental, and Materials Research (ACEM16)*.

Mallick, M., Mohanta, A., Kumar, A., and Charan Patra, K. (2020). "Prediction of Wind-Induced Mean Pressure Coefficients Using GMDH Neural Network." *Journal of Aerospace Engineering*, 33(1), 04019104.

Marquardt, D. W. (1963). "An algorithm for least-squares estimation of nonlinear parameters." *Journal of the society for Industrial and Applied Mathematics*, SIAM, 11(2), 431–441.

Mjolsness, E., and DeCoste, D. (2001). "Machine learning for science: State of the art and future prospects." *Science*, 293(5537), 2051–2055.

Mooneghi, M. A., Irwin, P., and Chowdhury, A. G. (2016). "Partial turbulence simulation method for predicting peak wind loads on small structures and building appurtenances." *Journal of Wind Engineering and Industrial Aerodynamics*, Elsevier, 157, 47–62.

Moravej, M. (2018). “Investigating scale effects on analytical methods of predicting peak wind loads on buildings.” Florida International University.

Moravej, M., Irwin, P., and Chowdhury, A. (2019). “A Simplified Approach for the Partial Turbulence Simulation Method of Predicting Peak Wind Loads.” *The 15th International Conference on Wind Engineering*, (September), 4–7.

Mostafa, K., Zisis, I., and Moustafa, M. A. (2022a). “Machine Learning Techniques in Structural Wind Engineering: A State-of-the-Art Review.” *Applied Sciences*, 12(10), 5232.

Mostafa, K., Zisis, I., and Stathopoulos, T. (2022b). “Large-Scale Wind Testing on Roof Overhangs for a Low-Rise Building.” *Journal of Structural Engineering*, 148(11), 1–21.

Murphy, K. P. (2012). *Machine learning: a probabilistic perspective*. MIT press.

Naeiji, A., Moravej, M., Matus, M., and Zisis, I. (2022). “Codification study of wind-induced loads on canopies attached to mid-rise buildings.” *Journal of Wind Engineering and Industrial Aerodynamics*, Elsevier Ltd, 227(June), 105050.

Nasrabadi, N. M. (2007). “Pattern Recognition and Machine Learning.” *Journal of Electronic Imaging*, 16(4).

Natekin, A., and Knoll, A. (2013). “Gradient boosting machines, a tutorial.” *Frontiers in neurorobotics*, Frontiers, 7, 21.

Nilsson, N. J. (2005). “INTRODUCTION TO MACHINE LEARNING AN EARLY DRAFT OF A PROPOSED TEXTBOOK Department of Computer Science.” *Machine Learning*, 56(2), 387–99.

Oh, B. K., Glisic, B., Kim, Y., and Park, H. S. (2019). “Convolutional neural network-based wind-induced response estimation model for tall buildings.” *Computer-Aided Civil and Infrastructure Engineering*, 34(10), 843–858.

Park, J., and Sandberg, I. W. (1991). “Universal approximation using radial-basis-function networks.” *Neural computation*, MIT Press, 3(2), 246–257.

Persson, C., Bacher, P., Shiga, T., and Madsen, H. (2017). “Multi-site solar power forecasting using gradient boosted regression trees.” *Solar Energy*, Elsevier, 150, 423–436.

Refaeilzadeh, P., Tang, L., and Liu, H. (2009). “Cross-validation.” *Encyclopedia of database systems*, Springer, 5, 532–538.

Reich, Y. (1997). “Machine learning techniques for civil engineering problems.” *Microcomputers in Civil Engineering*, 12(4), 295–310.

Reich, Y., and Barai, S. V. (1999). “Evaluating machine learning models for engineering problems.” *Artificial Intelligence in Engineering*, 13(3), 257–272.

Rumelhart, D. E., Hinton, G. E., and Williams, R. J. (1986). "Learning representations by back-propagating errors." *nature*, Nature Publishing Group, 323(6088), 533–536.

Saravanan, R., and Sujatha, P. (2018). "A state of art techniques on machine learning algorithms: a perspective of supervised learning approaches in data classification." *2018 Second International Conference on Intelligent Computing and Control Systems (ICICCS)*, IEEE, 945–949.

Shruti, K., Govindray, S. R., Rajasekharan, S. G., and Rao, P. N. (2021). "Artificial Neural Network-Based Prediction of Wind Pressure Coefficients on Buildings." *Journal of The Institution of Engineers (India): Series A*, Springer India, 102(2), 403–409.

Simiu, E., and Scanlan, R. H. (1996). "Wind effects on structures: fundamentals and applications to design." Wiley New York.

Stathopoulos, T. (2003). "Wind loads on low buildings: In the wake of Alan Davenport's contributions." *Journal of Wind Engineering and Industrial Aerodynamics*, 91(12–15), 1565–1585.

Stathopoulos, T., and Luchian, H. (1994). "Wind-induced forces on eaves of low buildings." *Journal of Wind Engineering and Industrial Aerodynamics*, 52(C), 249–261.

Taher, R. (2007). "Design of Low-Rise Buildings for Extreme Wind Events." *Journal of Architectural Engineering*, 13(1), 54–62.

Vickery, P. J. (2008). "Component and Cladding Wind Loads for Soffits." *Journal of Structural Engineering*, 134(5), 846–853.

Wang, X., Li, Q., and Li, J. (2020). "Field monitoring and wind tunnel study of wind effects on roof overhang of a low-rise building." *Structural Control and Health Monitoring*, 27(3), 1–25.

Waszczyszyn, Z., and Ziemiański, L. (2005). "Neural networks in the identification analysis of structural mechanics problems." *Parameter identification of materials and structures*, Springer, 265–340.

Weng, Y., and Paal, S. G. (2022). "Machine learning-based wind pressure prediction of low-rise non-isolated buildings." *Engineering Structures*, Elsevier Ltd, 258(March), 114148.

Wiik, T., and Hansen, E. W. M. (1997). "The assessment of wind loads on roof overhang of low-rise buildings." *Journal of Wind Engineering and Industrial Aerodynamics*, 67–68, 687–696.

Wu, T., and Kareem, A. (2011). "Modeling hysteretic nonlinear behavior of bridge aerodynamics via cellular automata nested neural network." *Journal of Wind Engineering and Industrial Aerodynamics*, Elsevier, 99(4), 378–388.

Zhang, Y., and Haghani, A. (2015). “A gradient boosting method to improve travel time prediction.” *Transportation Research Part C: Emerging Technologies*, Elsevier, 58, 308–324.

Zhou, Z.-H. (2012). “Ensemble Methods: Foundations and Algorithms.” Chapman and Hall/CRC.

Zisis, I., Raji, F., and Candelario, J. D. (2017). “Large-Scale Wind Tunnel Tests of Canopies Attached to Low-Rise Buildings.” *Journal of Architectural Engineering*, 23(1), 1–12.

Zisis, I., and Stathopoulos, T. (2010). “Wind-Induced Pressures on Patio Covers.” *Journal of Structural Engineering*, 136(9), 1172–1181.

VITA

KARIM ALY MOSTAFA

Born, Cairo, Egypt

2009-2014	B.S., Civil Engineering (Structural Engineering) Ain Shams University Cairo, Egypt
2014-2015	Teaching Assistant German University in Cairo Cairo, Egypt
2015	Teaching Assistant American University in Cairo Cairo, Egypt
2016-2018	M.S., Civil Engineering (Structural Engineering) University of Nevada, Reno Reno, Nevada, USA
2018-2019	Lecturer Assistant German University in Cairo Cairo, Egypt
2019-2022	Doctoral Candidate, Civil Engineering (Structural Engineering) Florida International University Miami, Florida, USA
2022	UGS Dissertation Year Fellow Florida International University Miami, Florida, USA

PUBLICATIONS AND PRESENTATIONS

Mostafa, Karim, Ioannis Zisis, Ted Stathopoulos, " Large-scale wind testing on roof overhangs for a low-rise building" ASCE Journal of Structural Engineering, Vol.84. issue 11 (2022): https://doi.org/10.1061/(ASCE)ST.1943-541X.0003477

Mostafa, K.; Zisis, I.; Moustafa, M.A. Machine Learning Techniques in Structural Wind Engineering: A State-of-the-Art Review. Appl. Sci. 2022, 12, 5232. https://doi.org/10.3390/app12105232.

Tolera, Ameyu B., Karim Mostafa, Arindam Gan Chowdhury, Ioannis Zisis, and Peter Irwin. "Study of wind loads on asphalt shingles using full-scale experimentation." Journal of Wind Engineering and Industrial Aerodynamics 225 (2022): 105005. https://doi.org/10.1016/j.jweia.2022.105005.

Mostafa, Karim, Ioannis Zisis, Ted Stathopoulos "Observations and Analysis of wind pressures on roof overhangs and underneath walls of a low-rise building." Proceedings of 6th Residential Buildings Design and Construction, virtual conference.

Mostafa, Karim, Ioannis Zisis, Ted Stathopoulos "Correlation of Wind-induced loads between roof overhangs and walls using large scale testing". 14th Americas conference on Wind Engineering, Texas Tech University, Lubbock, Texas , May 16th-19th (2022).

Mostafa, Karim, Ioannis Zisis, Ted Stathopoulos "Observations and analysis of wind pressures on roof overhangs and underneath walls of a low-rise building". 6th Residential Building Design & Construction Conference (virtual), Pennsylvania Housing Research Center, State College, Pennsylvania, May 11th-13th (2022).

Matus, Manuel, Karim Mostafa, Hrishikesh Dev Sarma, Brian Schwartz, Ioannis Zisis, "Design and development of a new Boundary Layer Wind Tunnel at Florida International University". 6th American Association for Wind Engineering workshop (virtual), Clemson University, Clemson, SC, May 12th-14th (2021).

Tolera, Ameyu B, Karim Mostafa, Arindam Gan Chowdhury, Ioannis Zisis, "Wind performance of Asphalt shingles using full-scale experimentation. 6th American Association for Wind Engineering workshop (virtual), Clemson University, Clemson, SC, May 12th-14th (2021).

Mostafa, Karim, Ioannis Zisis, Ted Stathopoulos, " Wind Loading on Roof Overhangs and Soffits: A codification Study". Engineering Structures (Submitted)

Mostafa, Karim, Ioannis Zisis, " Predicting wind-induced pressures on roof overhangs using artificial neural networks and ensemble methods". International Conference on Wind Engineering 16th , 2023 (Abstract Submitted)